Kinetic modeling of the heating processes in tokamak plasmas

NUGA Hideo

2011

Contents

Chapter 1

Introduction

1.1 Fusion energy

Huge increase in demand for energy available for human kind is expected in near future. Thus large-scale and sustainable energy generation satisfying environmental requirement has to be developed. Fusion energy is considered to be a future energy option, and will be able to play a significant role in providing a sustainable and secure solution for energy requirement.

1.1.1 Nuclear fusion reaction

Fusion energy is generated by some of nuclear fusion reactions. When two light nuclei approach sufficiently close to each other against electric repulsive force, they fuse and produce a new nucleus. The total mass of the new nucleus and by-products is slightly smaller than the total mass of the two fused nuclei. The mass deficit, Δm, between the two incident nuclei and the fusion product nucleus is converted into kinetic energy, E, according to the following equation;

$$E = \Delta m c^2$$

where c denotes the velocity of light.

Some fusion reaction candidates available for fusion power plants are listed below. (Branching ratios are correct for energies near the cross section peaks.) [1]

$$\mathrm{D + D} \rightarrow_{50\%} \mathrm{T(1.01MeV) + p(3.02MeV)} \tag{1.1}$$
$$\rightarrow_{50\%} \mathrm{He^3(0.82MeV) + n(2.45MeV)} \tag{1.2}$$
$$\mathrm{D + T} \rightarrow \mathrm{He^4(3.5MeV) + n(14.1MeV)} \tag{1.3}$$
$$\mathrm{D + He^3} \rightarrow \mathrm{He^4(3.6MeV) + p(14.7MeV)} \tag{1.4}$$
$$\mathrm{T + T} \rightarrow \mathrm{He^4 + 2n + 11.3MeV} \tag{1.5}$$
$$\mathrm{He^3 + T} \rightarrow_{51\%} \mathrm{He^4 + p + n + 12.1MeV} \tag{1.6}$$
$$\rightarrow_{43\%} \mathrm{He^4(4.8MeV) + D(9.5MeV)} \tag{1.7}$$
$$\rightarrow_{6\%} \mathrm{He^5(2.4MeV) + p(11.9MeV)} \tag{1.8}$$

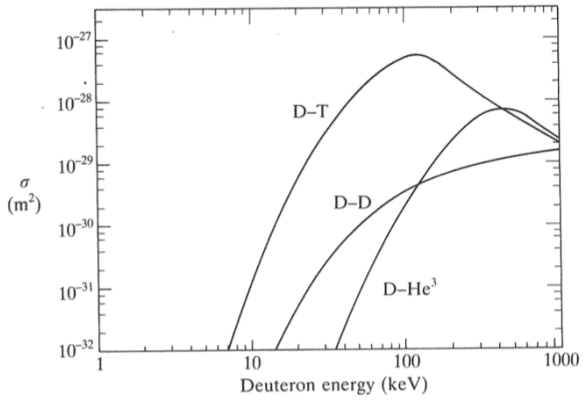

Figure 1.1: Fusion cross sections for some reactions as a function of the relative kinetic energy of the incident particles. [2]

1.1.2 Fusion cross section and reaction rate

The cross section of the reaction, σ, is a measure of the probability of the fusion reaction as a function of the relative velocity of the two reactant nuclei. Fig. 1.1 shows fusion cross section as a function of the relative kinetic energy of the incident particles. From the figure, it is seen that the maximums cross section occurs at around 100 keV in D-T reaction, and the energy which maximized the D-T reaction cross section is the lowest among the fusion reactions. Owing to this reason, the D-T reaction is preferred for fusion plant nearest future, and this reaction will be employed in the ITER (International Thermonuclear Experimental Reactor) project [3].

1.1.3 Plasma confinement scheme

When particles are accelerated enough to fuse each other, the particles are fully ionized. The fully ionized gas is called as plasma. Although plasma is rarely found on earth, it is estimated that more than 99% of the matter identified in universe exists as plasma.

In order to operate a fusion reactor, extremely high temperature (higher than 10keV) plasma must be confined in some space until fusion reaction occurs. Plasma density and confinement time depend on the plasma confinement scheme. There are two major types of plasma confinement schemes, one is inertial confinement, the other is magnetic confinement.

Inertial confinement

In the inertial confinement scheme, nuclear fusion reactions are initiated by heating and compressing a fuel pellet. In order to heat and compress a fuel pellet, high energy beam of laser , ($\sim 10^{15}$W), is applied as an energy driver. Typically in this scheme, the plasma density reaches extremely high, $\sim 10^{31\sim32}\mathrm{m}^{-3}$, while the required energy confinement time becomes very short, $\sim$ 10ns.

In 2010, there are some laser driven inertial confinement devices, such as 'NIF' in U.S., 'Gekko XII' in Japan, 'ISKRA' lasers in Russia and more.

Magnetic confinement

The magnetic confinement scheme is highly developed and is usually considered more promising for energy production. Since particles in plasma have electric charge, they are tied around a magnetic field line due to the Lorentz force. Typically in this scheme, the plasma density becomes $\sim 10^{20}\mathrm{m}^{-3}$, while the necessary energy confinement time becomes larger than 1s.

In 2010, there are many magnetic confinement devices. Magnetic confinement devices are classified by the magnetic configuration, such as tokamak, helical system, mirror, and so on. ITER is a tokamak type reactor which is under construction in France. In this paper, plasma confined in tokamak configuration is studied.

1.1.4 Merits of fusion energy

Resources

The resources necessary for fusion reactor was well studied in 1970s. It was found that the most of materials required for the D-T fusion reactor is sufficiently resourceful. Here, the some characteristic resources for steady state tokamak reactor (SSTR [4]) which is the typical design of D-T fusion plant are discussed.

- Deuterium (D_2) as fuels

A fusion plant which generate $\sim$ 3 GW thermal output and $\sim$ 1 GW electric output expends $\sim$ 200 g deuterium on a day. Since deuterium exists abundantly in seawater ($\sim$ 48 Tera tons), deuterium can be supplied inexhaustibly. Deuterium is produced by the Girdler sulfide process which is a kind of isotope exchange method, and this process can produce plentiful deuterium economically.

- Lithium (Li) as tritium source

Since tritium, a fuel of D-T reactor, is extremely rare naturally on the earth, it is necessary to produce tritium by neutron activation of lithium-6 in tritium breeding blankets.

$$\mathrm{Li}^6 + \mathrm{n} \rightarrow \mathrm{He}^4(2.05\mathrm{MeV}) + \mathrm{T}(2.75\mathrm{MeV})$$

Although lithium is widely distributed on Earth, it does not naturally occur in elemental form due to its high reactivity. Lithium resources are estimated as 19 million tons in continental brine and 11 million tons in mineral. Moreover 230 billion tons lithium is contained in seawater. Lithium occurrences content of seawater exist at a relatively constant concentration, on the other hand, lithium reserves of brine and mineral are distributed unevenly. Presently resources in brine and mineral are mainly mined in a commercial reason.

Approximate 2000 fusion reactors are needed when assuming that the electrical power consumption of present all of the world (~ 19 PWh in 2006) is supplied in the 1 GW class fusion reactor. If a D-T fusion reactor is running for 30 years, about 300 tons lithium will be consumed for blankets and Lithium consumption per a year becomes about 10 tons. Thus 2000 fusion reactors consume lithium 20 kilo tons in a year.

From the lithium reserves and the expectation of lithium consumption, lithium can be extracted around 1000 years. Furthermore, if the economic efficiency of lithium extraction from seawater increases, lithium can be supplied inexhaustibly.

- Beryllium (Be) for neutron multiplication

In order to increase tritium breeding ratio, neutron multiplier composed of Be are used in the blanket.

$$Be^9 + n \rightarrow 2n + 2He^4$$

The resources of beryllium are estimated approximately 740 kilo tons all of the world [5].

It is estimated that a SSTR consume ~ 110 tons beryllium, thus ~ 220 kilo tons beryllium is needed for 2000 SSTRs which supply electrical power consumed in present all of the world. Furthermore, since 1 ton of beryllium will be consumed through the nuclear reaction by a SSTR per a year, 2000 SSTRs will consume 2000 tons of beryllium per a year. From these estimation, it seems that beryllium will be short in a few hundred years. However, there is a possibility that resources of beryllium increase. Since the present demand of beryllium is low, resource explanation is done insufficiently [6, 7]. In addition, beryllium which is a material of neutron breeder can be substituted by lead. Moreover, Li/V blanket which uses liquid lithium as coolant and breeder does not require neutron breeder [8]. In these reasons, beryllium resources will make no trouble for fusion reactor.

- Vanadium (V) for blanket material

Vanadium holds great promise for structural material of liquid metal blanket. This type of blanket has a feature that beryllium as neutron breeder materials is not required. The resources of vanadium are estimated approximately 27 million tons all of the world.

It is estimated that 600 tons of vanadium will be required for structural material of a SSTR, and 300 tons of vanadium will be changed every three years. Therefore it seems that resources of vanadium will be short in approximate 200 years. However, since very plentiful vanadium (~ 2.7 billion tons) is contained in seawater, if the economic efficiency of vanadium extraction from seawater increases, vanadium can be supplied inexhaustibly.

- Niobium (Nb) for superconducting material

Since niobium is a kind of rare metal and used for superconducting coil, the resources of niobium are also important. The resources of niobium are estimated approximately 4.2 million tons.

It is estimated that approximate 400 kilo tons of niobium will be required for superconducting material of 2000 SSTRs. Assuming the lifetime of SSTR is 40 years, niobium is able to be supplied for approximate 400 years. If superconducting materials are 90% recycled, the resources of niobium make no problems for a few thousand years.

- note

SSTR is designed in the early 1990s. In present (2000s), some tokamak reactors which are more economical and more efficiency are designed [9, 10]. Therefore it seems that resources of constructing materials will be consumed less than that of estimated above.

Safety

Since fusion plasma emits a strong flux of neutron radiation during the operation of fusion reactor, it is expected that some radiation will leak from plants even though plants are shielded. The expected amount of radiation at site boundary during ITER operation is an amount equivalent to one tenth of natural radiation (1 mS) or less.

Moreover, since nuclear reactions in fusion plants make no nuclear waste, fusion plants make no high-level radioactive waste unlike fission plants. Therefore it only has to consider the neutron induced activation material as radioactive waste. The radiological toxic hazard potential[1] of fusion plants is much lower than the nuclear fission plants, furthermore low activation material makes the risk lower.

Environmental

Since nuclear reactions make no CO_2, nuclear plants can generate electric power without CO_2 emissions. Therefore CO_2 is emitted at only the stages of construction and dismantlement of fusion plants.

Fig. 1.2 shows the comparison of the amount of CO_2 emissions among verious kind of electrical power plants [13]. From this figure, it is found that the amount of CO_2 emissions from fusion plant is estimated smaller than that of most of other plants

1.2 Tokamak

Tokamak is a kind of axisymmetric magnetic configuration, in which the plasma current itself gives rise to the poloidal field essential to the equilibrium of toroidal plasmas. The tokamak type device is composed of toroidal field coils, poloidal field coils, ohmic heating coil, and vacuum vessel mainly.

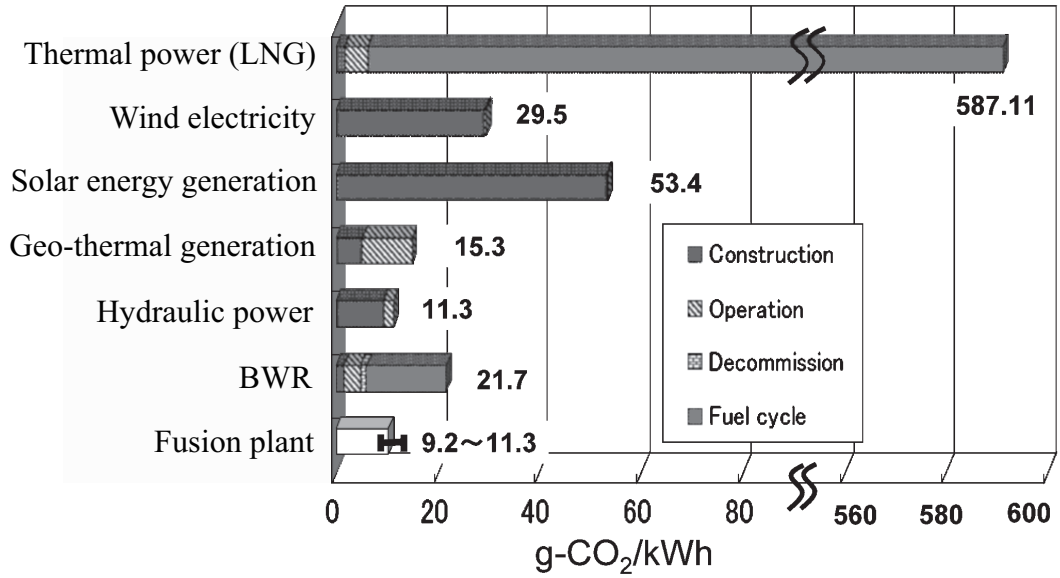

Figure 1.2: Comparison of CO_2 emissions from fusion reactor and other electric generation systems. These values except fusion are quoted from [11, 12].

1.2.1 Magnetic configuration

The conceptual diagram of tokamak is shown in Fig. 1.3. The tokamak plasma is described in toroidal coordinate system (r, θ, ϕ), where r, θ, and ϕ denote minor radius, poloidal angle, and toroidal angle. Since the tokamak plasma is not cylinder but torus, the strength of the toroidal magnetic field is inversely proportional to the major radius from the torus axis and encircles the torus axis. Charged particles drift due to the inhomogeneity and curvature of the toroidal magnetic field. The direction of the magnetic drift due to gradient and curvature of B_t is the opposite direction for electrons and ions. Therefore these drifts generates the vertical electric field due to the charge separation as shown in Fig. 1.4. And then, both electrons and ions drift towards the outer region of the confined plasma due to the $\boldsymbol{E} \times \boldsymbol{B}$ drift. In this way, plasma can not be confined in a simple torus. In order to overcome this problem, the poloidal magnetic field is introduced.

The poloidal magnetic field prevents the separation of the charged particle to occur. It makes magnetic field line curved around magnetic axis, and a magnetic field line becomes a spiral and a magnetic surface is created as shown in Fig. 1.5. Since charged particles can move freely along magnetic field lines, spiral magnetic field lines enable the charge separation to be short-circuited. The poloidal magnetic field is generated by toroidal plasma current I_P.

Since plasma particles gyrate around magnetic field line, a guiding center of plasma particle also gyrates around magnetic axis like a magnetic field line. Accordingly, the

[1]Radiological Toxic Hazard Potential: The influence of exposure when radionuclide is taken into human body is shown in this value.

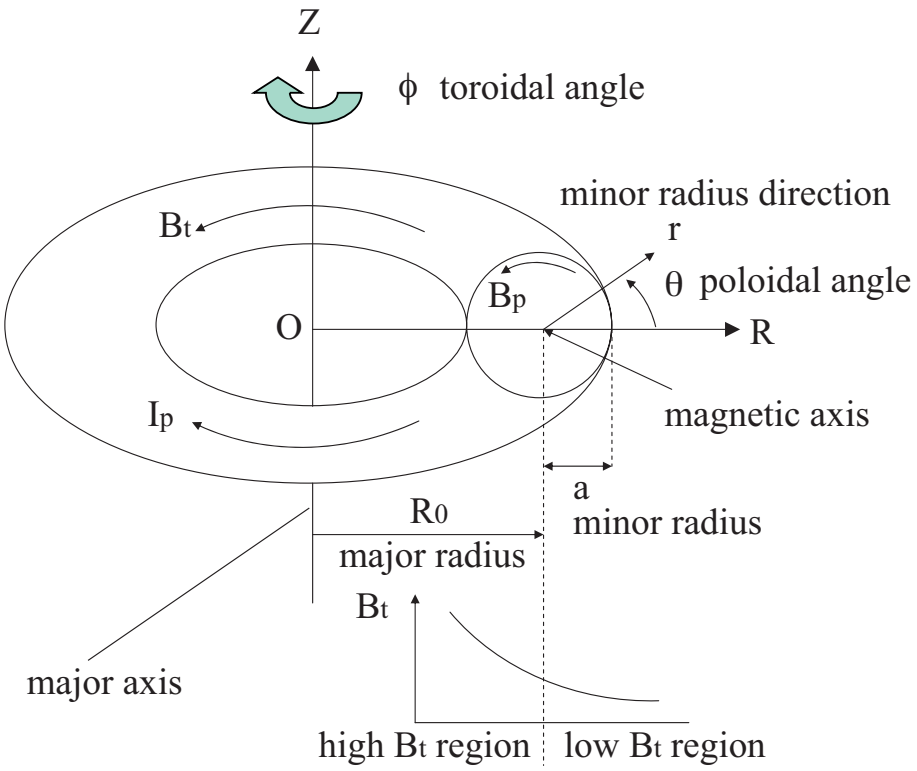

Figure 1.3: The conceptual diagram of tokamak configuration. The toroidal magnetic field B_t is generated by toroidal field coils, while the poloidal magnetic field B_p is generated by the plasma current I_p and the poloidal field coils.

orbit of plasma particles makes a closed circle on poloidal cross section.

1.2.2 Trapped particle

Since toroidal magnetic field is inversely proportional to major radius, the guiding center rotating around the magnetic axis feels stronger magnetic field when it moves to high B_t region from low B_t region. This inhomogeneity of the toroidal magnetic field classifies the guiding center motion of particles into two types, one is passing particle another is trapped particle.

If $v_{\|0}$ (velocity component parallel to the magnetic field at the minimum magnetic field point) is much smaller than $v_{\perp 0}$ (velocity component perpendicular to the magnetic field at the minimum magnetic field point) and satisfies the condition;

$$\frac{v_{\perp 0}}{v_{\|0}} > \sqrt{\frac{1-\epsilon}{2\epsilon}}$$

the particle is trapped in the region of weak magnetic field due to the mirror effect as is shown in Fig. 1.6 (where $\epsilon = r/R_0$). This kind of particles are called trapped particles. Meanwhile, circulating particles without trapped are called passing particles.

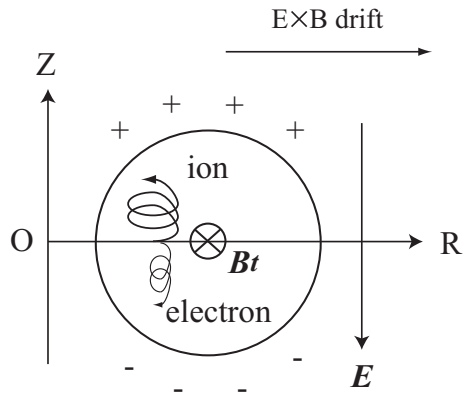

Figure 1.4: Outward drift of plasma particle

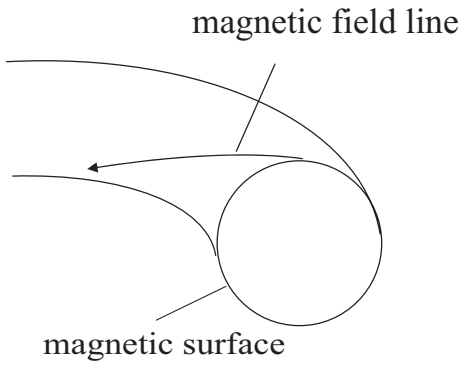

Figure 1.5: Magnetic field line and magnetic surface

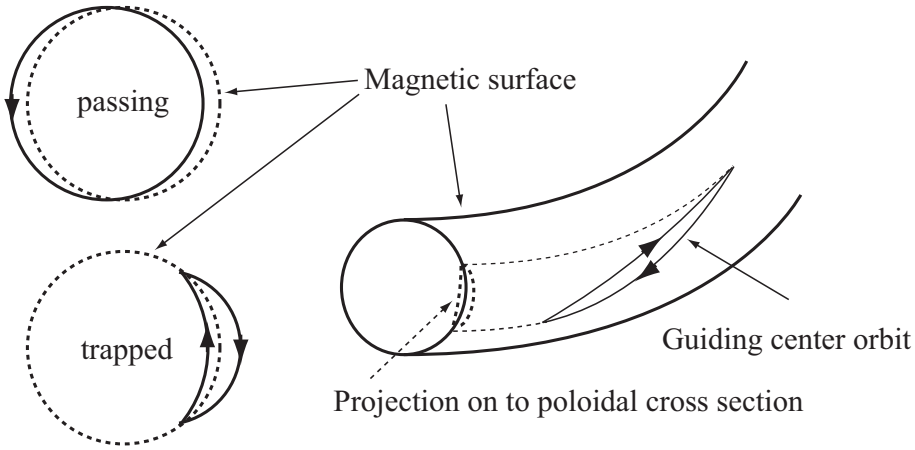

Figure 1.6: Guiding center orbits of passing and trapped particle.

The trapped particle has several features which passing particle does not have. Because of these features, it is necessary to consider physical mechanism separately.

1.3 Plasma heating in tokamak plasmas

In a fusion plasma, the energy losses are balanced by the plasma heating from the slowing down of α particles resulting from the fusion reaction. The fusion reaction rate, however, is a strong function of temperature and is negligible at low temperatures. Thus to reach the temperature required for reaction, it is necessary to provide some kind of heating. There are several methods proposed for this requirement.

	EC	IC	LH	NBI
Frequency (Energy)	170 GHz	40 ~ 60MHz	5GHz	1MeV
Injection power	20MW	20MW	0	33MW
Unit power	1MW	2.5MW	1MW	16.5MW D^0
Upgrade option	+20MW	+20MW	+20 ~ 40MW	17MW

Table 1.1: Installation plan of ITER heating and current drive systems. [14, 15]

1.3.1 Ohmic heating

One of the conventional methods is ohmic heating caused by the joule heating of toroidal current. At low temperatures, ohmic heating is quite powerful and, in large tokamaks, easily produces temperatures of a few keV. However, as the temperature increases, the collision frequency and the resistivity fall. Consequently, at the temperatures required for reactor operations, the power of ohmic heating is strongly reduced.

In addition, since the toroidal current necessary for ohmic heating is driven by an inductive electric field generated by the primary coil as is shown in Fig. 1.7, it is impossible to drive toroidal current in steady state. As a consequence, additional heating is required.

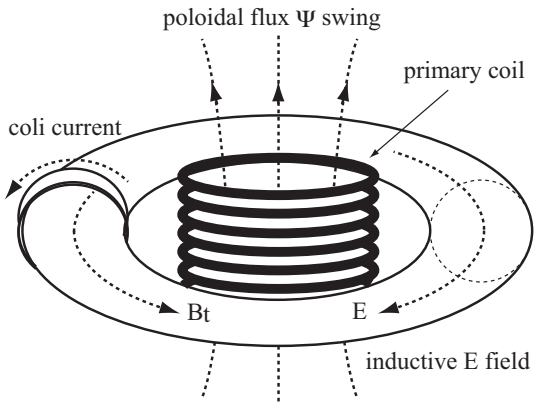

Figure 1.7: The conceptual diagram of primary coil and toroidal inductive current.

1.3.2 Wave heating

One of the main method which are envisaged for heating to ignition temperatures is resonant absorption of electromagnetic waves. When an electromagnetic wave propagates through a plasma, the electric field of the wave accelerates a group of charged particles which then heat the plasma through collisions. Wave heating has been used to heat magnetically confined plasmas since the early days of fusion research. Three schemes have emerged as the most successful, namely, ion cyclotron (IC), lower hybrid (LH), and electron cyclotron (EC) heating (H) and current drive (CD). Each method has been tested at the Mega Watt level in major tokamak devices.

In ITER, tens of MW wave heating is planned as is shown in Table 1.1. EC wave are used for plasma ramp up, plasma heating, current drive for sustaining operation, and suppression of neoclassical tearing mode (NTM). Especially, EC waves which is able to drive local plasma current is essential for stabilization of NTM. In ITER, a coupled transport and MHD simulation has shown that 20MW EC wave power is required for NTM suppression. Since IC wave has a good track record of some dozens of MW ion heating in several experimental devices, such as JT-60, JET, and LHD, IC heating and

current drive device will be equipped as highly-dependable heating source and core plasma current drive. Moreover, ICH is expected as the method of fusion reaction control, because ICRF can heat ions selectively.

1.3.3 Neutral Beam Injection

Another promising method for plasma heating to reactor operation is the neutral beam injection (NBI). The beams used for injection heating have to be composed of neutral particles because ions can not penetrate across the tokamak magnetic field. Heating with neutral beams is a slightly complicated process. Ions must be produced first and accelerated to a required energy. They are then neutralized by charge exchange in a gas target, and the unwanted residual ions are removed. Once the neutral beam particles entering the plasma become ionized, the resulting fast ions are slowed down by Coulomb collisions. Through the slowing down process, the kinetic energy is transferred to the particles in the plasma, causing heating of both electrons and ions. At high injection velocity, the electron heating is initially dominant. Then, as the beam ions slow down, the heating is transferred to the ions.

It is clearly desirable that as much of deposition as possible should take place in the central region of plasma. This means avoiding both too strong absorption, which leads to heating of the plasma edge, and too weak absorption which allows transmission of the beam through the plasma to produce heating and particle sputtering at opposite material surfaces. The deposition of beam particles depend on the energy of beam particles and the plasma density. In the high density ($\sim 10^{20}$ m^{-3}) plasma, since tens of keV neutral beam is not able to penetrate plasma core, high energy neutral beam ($\sim$ 1MeV) is required. Because of this requirement, high energy negative-ion based neutral beam injection systems (N-NBI) have been developed [16]. In ITER, tens of MW N-NBI is planned as is shown in Table 1.1.

1.3.4 α particle heating

Different from the previous heating schemes, α particle heating is a internal heating without external heating devices. The D-T thermonuclear power consists of two parts. Four fifth of the reaction energy is carried by neutrons and one fifth is carried by α particles.

$$D^+ + T^+ \rightarrow He^{2+}(3.5\text{MeV}) + n(14.1\text{MeV})$$

The neutrons leave the plasma without interaction with plasma but the α particles, being charged, are confined by the magnetic field. The α particles then transfer their 3.5MeV energy to the plasma through collisions.

As a D-T plasma is heated to thermonuclear conditions, the α particle heating provides an increasing fraction of total heating. When adequate confinement conditions are provided, a point is reached where the plasma temperature can be maintained against the energy losses solely by α particle heating. In this case, the applied heating can be removed and the plasma temperature is sustained by internal heating. By analogy with the burning fossil fuels, this event is called ignition.

1.4 Kinetic analysis

Kinetic theory describes the behaviour of plasmas in terms of the particle motions. Because of the large number of particles involved, this description has to be statistical. In practice, this is carried out using the distribution function, $f(\boldsymbol{r}, \boldsymbol{v}, t)$ which measures the probability density for a single particle in six dimensional phase space, ($\boldsymbol{r}$,$\boldsymbol{v}$). The behaviour of the distribution function is described by the kinetic equation.

For many purposes, it is adequate to describe the plasma in terms of fluid variables such as the particle density $n(\boldsymbol{r}, t)$, fluid velocity $\boldsymbol{u}(\boldsymbol{r}, t)$, and pressure $p(\boldsymbol{r}, t)$ which are functions of only four variables. In fact, a lot of conventional transport codes apply fluid description instead of kinetic description because it is easy to calculate fluid model due to less variables. Although conventional transport simulation which use diffusive fluid transport equation describes only fast particle in the momentum distribution function, there are some vagueness of classification between fast particles and bulk particles. Thus kinetic transport simulation is required because there are a lot of kinetic effects which can not be described by fluid models in fusion plasmas. One of the effects is the effect of plasma heating. Plasma heatings, such as ohmic, RF, NBI, and α particles, deform the velocity distribution function of plasma from Maxwellian to non-Maxwellian. Ohmic heating accelerates the plasma particles parallel to the magnetic field line, while IC and EC waves mostly accelerate perpendicular to the magnetic field line. NBI is a particle source with strong anisotropy, and α particle heating is a non-thermal particle source. In this reason, kinetic description is required for accurate analysis of plasma heating in tokamaks.

1.4.1 Fokker-Planck equation

In the absence of collisions, the velocity distribution function obeys the following equation under the electromagnetic field.

$$\frac{\partial f}{\partial t} + \boldsymbol{v} \cdot \frac{\partial f}{\partial \boldsymbol{r}} + \frac{e}{m}(\boldsymbol{E} + \boldsymbol{v} \times \boldsymbol{B}) \cdot \frac{\partial f}{\partial \boldsymbol{v}} = 0 \tag{1.9}$$

This equation is called Vlasov equation. The inclusion of collisions requires the additional collision term, $(\partial f/\partial t)_c$ to the RHS of eq. (1.9). Vlasov equation including a collision term derived on the basis of multiple small angle collisions is the Boltzmann equation.

$$\frac{\partial f}{\partial t} + \boldsymbol{v} \cdot \frac{\partial f}{\partial \boldsymbol{r}} + \frac{e}{m}(\boldsymbol{E} + \boldsymbol{v} \times \boldsymbol{B}) \cdot \frac{\partial f}{\partial \boldsymbol{v}} = \left(\frac{\partial f}{\partial t}\right)_c \tag{1.10}$$

Many plasma phenomena involve processes which are slow compared to the cyclotron frequency and which vary slowly in space compared to the Larmor radius of the individual particles, such as transport. To study such phenomena simpler kinetic equations which average over the fast Larmor motion have been derived. The advantage of such kinetic equations lies in the reduced dimensionality of the phase space. The Fokker-Planck equation has the six independent variables $(\boldsymbol{r}, \boldsymbol{v})$, and the gyro-averaging reduces them to five, $(\boldsymbol{r}, v_{\parallel}, v_{\perp})$, where $v_{\parallel}$ is the velocity parallel to the magnetic field

line, and $v_\perp$ is the velocity perpendicular to the magnetic field line. The gyro-averaged velocity distribution function is described as

$$\bar{f} = \frac{1}{2\pi} \int f \, d\phi. \tag{1.11}$$

The equation which the gyro-averaged velocity distribution function obeys is called drift kinetic equation. In our study, we refer to "gyro averaged distribution function" and "drift kinetic equation" just as "distribution function" and "kinetic equation" for simplicity.

1.4.2 Previous work

One of the earliest kinetic evaluations of ICRF heating was done by Stix [17] using Fokker-Planck theory. Several authors [18, 19, 20] applied Stix's approach to reactor studies and wrote Fokker-Planck codes. Some of them had three dimensions (time, parallel and perpendicular velocity). These approaches, however, assumed uniform magnetic field, so spatial distribution and wave propagation are neglected. The assumption of homogeneous magnetic field is assured in the study of RF heating and current drive in tokamaks if the RF waves interact only with passing particles. This is often not proper in cyclotron heating case because cyclotron resonances develop distribution function of heated species to perpendicular direction and it will cause heated particle to be trapped. In this reason, a number of bounce-averaged Fokker-Planck codes have been written [21, 22, 23, 24, 25]. Some of them consists of a 2D in momentum space, multi-species, relativistic, bounce-averaged Fokker-Planck equation solver running on a radial array of non-circular flux surface [26].

1.4.3 Our kinetic analysis

Our Fokker-Planck code TASK/FP [22] is one of them. TASK/FP has advanced features as follow. Firstly, it includes non-linear collision term to the second order Legendre harmonics in order to conserve total density, momentum and energy through collision. Secondly, it calculates velocity distribution function of each species simultaneously. Thus, velocity distribution function of background particles are non-Maxwellian. Thirdly, it is able to couple with full wave analysis code TASK/WM [27] in order to evaluate ICRF wave-particle interaction. Fourthly, fusion reaction rate is calculated without the assumption of Maxwellian background.

1.5 The contents of this thesis

The objective of this thesis is to develop a drift kinetic transport code and to study the time evolution of the plasma including the deformation of velocity distribution function in plasma heating. And the aim of this study is to contribute to the international

collaboration for the development of ITER integrated modeling codes and the domestic collaboration for the code development intended for computer simulations in the Broader Approach activities.

Chapter 2 introduces the integrated code TASK which describes the time evolution of toroidal plasmas. Since various phenomena with broad range of time and spatial scales occurs, it is impossible to describe whole phenomena in a single simulation code. Therefore integrated code TASK implements several components which describe various phenomena separately. The drift kinetic transport component TASK/FP is also included in TASK.

In Chapter 3, a detailed description of kinetic transport code TASK/FP is given: basic equation, implemented models, and numerical scheme. And then, verification of the code is given in Chapter 4.

Chapter 5 and 6 show simulation results with ITER like plasma parameters by using TASK/FP. In Chapter 5, the simulation of the case without radial transport is shown. And then the simulation of the case with radial transport is presented in Chapter 6.

Finally, the thesis is summarized and future perspective of this study is presented in chapter 7.

Chapter 2

Integrated code TASK

In order to develop reliable and efficient schemes to control burning plasma, numerical simulations which predict the behavior of burning plasma in tokamaks are needed. However, the phenomena related in burning plasma have various temporal (a few hundred GHz~ a few thousand sec) and spatial (a few μm ~ a few ten m) scales and the simulations have to describe whole plasma and whole discharge as are shown in Fig. 2.1 and 2.2. In this reason, a single simulation code never covers all the phenomena essential for reactor operation. Therefore simulation of burning plasmas requires integrated modeling of various physics phenomena with wide-ranging spatial and time scales.

Because of this requirement, our integrated modeling code TASK (Transport Analyzing System for Tokamak) has been developed since 1992. The features of the code are listed below.

1. TASK is an integrated code which have a modular structure.
2. It include various heating and current drive schemes.
3. It has high portability and most of library routines are included.
4. Parallel processing using MPI library is enabled.
5. Open Source: `http://bpsi.nucleng.kyoto-u.ac.jp/task/`
6. Expansion for 3D helical system has been developed.

At present, the TASK code is composed of several components which are listed in Fig. 2.3. Each component exchanges initial data and calculated results and use them for its calculation. For example, the Fokker-Planck component TASK/FP calculates time evolution of the momentum distribution function using the magnetic configuration calculated by the equilibrium component TASK/EQ and the wave electric field calculated by the full wave analysis component TASK/WM. When TASK/WM calculates the wave electric field, it calls the wave dispersion component TASK/DP in order to calculate the dielectric tensor. The wave dispersion calculation the requires magnetic configuration (TASK/EQ), the density and temperature profiles (TASK/TR). It also can include the effect of relativistic non-Maxwellian distribution function which is calculated by TASK/FP.

The rest of this chapter introduces briefly several components of TASK. Detailed explanation of the Fokker-Planck component TASK/FP will be given in Chapter 3.

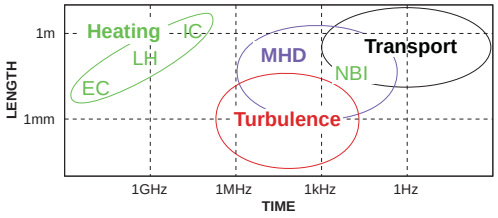

Figure 2.1: The range of time and spatial scales of the phenomena in fusion plasmas.

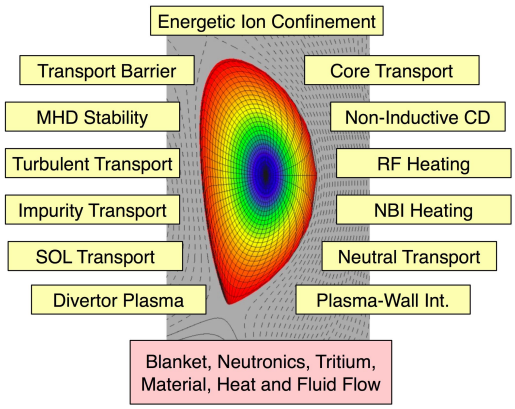

Figure 2.2: Simulation of burning plasma covering whole plasma is required.

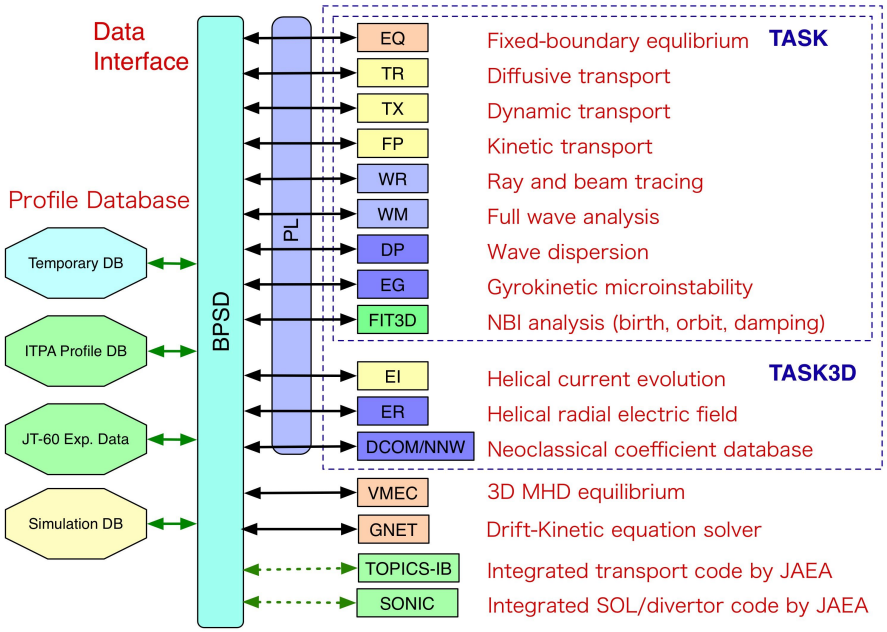

Figure 2.3: The structure of integrated code TASK.

2.1 Equillibrium components

The MHD equilibrium of an axisymmetric plasma is governed by Grad-Shafranov equation. TASK has two equilibrium components, TASK/EQ and TASK/EQU. TASK/EQ solves Grad-Shafranov equation with a fixed plasma boundary condition for given plasma pressure and safety factor profiles. Using the solution of Grad-Shafranov equation or reading the equilibrium data from a file, TASK/EQ calculates the magnetic flux coordinates and metric data. The other component TASK/EQU solves Grad-Shafranov equation with a free boundary condition for given separatrix points by iteration starting from initial poloidal coil currents. In this study, TASK/EQ is used.

Equilibrium component TASK/EQ calculates the poloidal magnetic flux $\psi(R, Z)$ which satisfies Grad-Shafranoc equation.

$$R\frac{\partial}{\partial R}\frac{1}{R}\frac{\partial \psi}{\partial R} + \frac{\partial^2 \psi}{\partial Z^2} = \mu_0 R^2 \frac{dp(\psi)}{d\psi} - F(\psi)\frac{dF(\psi)}{d\psi} \tag{2.1}$$

where, $P(\psi)$, $F(\psi)$, R, and Z denote the pressure profile, the poloidal current density profile, the vertical position, and the major radius, respectively. The poloidal magnetic flux determines the shape of the cross section of the plasma.

2.2 Wave analysis components

There are various kinds of electromagnetic fields in tokamak plasma, excited internally or externally, with a wide range of frequency, growth rate and wave number. In order to describe the excitation, propagation, and absorption of the fields several modeling schemes have been used in toroidal plasma as shown in Table. 2.1.

The full wave analysis component, TASK/WM [27, 28], analyzes the wave propagation by solving a boundary value problem of Maxwell's equations.

$$\nabla \times \nabla \times \boldsymbol{E}(\boldsymbol{r}) = \frac{\omega^2}{c^2} \overleftrightarrow{\epsilon}(\boldsymbol{r}) \cdot \boldsymbol{E}(\boldsymbol{r}) + i\omega\mu_0 \boldsymbol{j}_{ext}(\boldsymbol{r}), \tag{2.2}$$

where $\tilde{\boldsymbol{j}}_{ext}(\boldsymbol{r}, t) = \boldsymbol{j}_{ext}(\boldsymbol{r}) \exp(-i\omega t)$ and $\tilde{\boldsymbol{E}}(\boldsymbol{r}, t) = \boldsymbol{E}(\boldsymbol{r}) \exp(-i\omega t)$ denote the external antenna current density and the wave electric field with a wave angular frequency ω and

Scheme	Temporal dependence	Spatial dependence	TASK
Wave optics	Initial value problem	FEM/FDM	-
	Boundary value problem	Fourier analysis	-
		Fourier & FEM/FDM	WM
		FEM/FDM	WF
Geometrical optics	Initial value problem	Ray tracing	WR
		Beam tracing	WR

Table 2.1: Type of wave modeling

$\overleftrightarrow{\epsilon}(\boldsymbol{r})$ is the dielectric tensor which is calculated by the wave dispersion component TASK/DP. It uses the Fourier expansion in the poloidal and toroidal directions and the finite element method (FEM) in the radial direction. The TASK/WM has been used in the analysis of wave heating and current drive in the ion cyclotron range of frequency [29]. Since the wave frequency can be complex in TASK/WM, it is applicable to the eigen mode analysis by maximizing the volume integral of the square of the wave amplitude for given excitation proportional to the electron density. It also has been applied to the analysis of Alfvén eigen mode. Another full wave component TASK/WF using three dimensional FEM is under development for the analysis of the waves with shorter wave length.

The ray tracing component, TASK/WR, solves the ray equation in the Hamiltonian form to calculate the ray position and the wave number from the dispersion relation which corresponds to the Hamiltonian. It also uses the dielectric tensor component, TASK/DP, to calculate the dispersion relation. The TASK/WR is applicable to beam tracing in which the radius of the wave beam and the curvature radii of the equi-phase wave surface are also calculated. The TASK/WR has been applied to the electron cyclotron heating and current drive as well as the lower-hybrid current drive.

The wave dispersion component TASK/DP calculates the dielectric tensor $\overleftrightarrow{\epsilon}(\omega, \boldsymbol{k}; \boldsymbol{r})$. Various models of dielectric tensor are available in the code. For example, resistive MHD, collisional multi-fluid, uniform kinetic, and drift kinetic models are implemented. For the kinetic models, not only the Maxwellian distribution function but also any form of equilibrium momentum distribution function, such as the output calculated by the Fokker-Planck component TASK/FP can be used through numerical integration. In this thesis, kinetic model is employed.

2.3 Transport components

Transport components usually describe the time evolution of the plasma in the transport time scale. Table 2.2 shows various levels of transport modeling. The most accurate models are full kinetic and gyro kinetic which is usually used in the analysis of the turbulence. However these models requires very large amount of computational resources.

On the other hand, conventional transport modeling (TASK/TR) is easy to calculate the time evolution of the plasma. It solves the diffusive transport equation accompanied with the flux gradient relation. Since the flux gradient relation is derived from the stationary solution of the equation of motion, quick change of the transport may not be described self-consistently.

The dynamic transport modeling (TASK/TX [30]) solves the flux-surface-averaged multi-fluid equations coupled with Maxwell's equation. Since the equations of motion and Poisson's equation are solved simultaneously, the plasma rotation and the radial electric field are self-consistently calculated without the assumption of quasi-neutrality.

In order to analyze the heating and current drive which usually produce energetic particles and modify the velocity distribution function, the kinetic transport modeling (TASK/FP) has been developed. It solves the bounce averaged Fokker-Planck equation for the momentum distribution function including radial transport and will be described

Model	Equation	Variables	TASK
Fluid model	Diffusive transport equation	$n(\rho,t)$, $v_\phi(\rho,t)$, $T(\rho,t)$	TR
	Dynamic transport equation	$n(\rho,t)$, $\boldsymbol{u}(\rho,t)$, $T(\rho,t)$	TX
Kinetic model	Bounce averaged drift kinetic equation	$f(p,\theta,\rho,t)$	FP
	Axisymmetric gyrokinetic equation	$f(p,\theta,\rho,\chi,t)$	-
	Gyro kinetic equation	$f(p,\theta,\rho,\chi,\zeta,t)$	-
	Full kinetic equation	$f(p,\theta,\phi,\rho,\xi,\zeta,t)$	-

Table 2.2: Type of transport modeling.

in the next chapter.

Chapter 3

Fokker-Planck component TASK/FP

In this chapter, we concentrate on the Fokker-Planck component TASK/FP [29, 31]. In order to include the relativistic effects, TASK/FP treats the *momentum* distribution functions. So, here, f denotes the momentum distribution function not the velocity distribution function.

3.1 Preliminaries

3.1.1 Coordinate systems

In TASK/FP, the assumptions of azimuthal symmetry in momentum space and toroidal symmetry in real space are applied. In the poloidal direction, we average over the bounce and circulating motion of the particles on a magnetic surface. Therefore variables of the momentum distribution function $f(\boldsymbol{p}, \boldsymbol{r}, t)$ are reduced to $f(p_\parallel, p_\perp, \rho, t)$, where $p_\parallel$, $p_\perp$, and ρ denote the momentum parallel or perpendicular to magnetic field at the poloidal position where the strength of the magnetic field is minimum on the magnetic surface, and the normalized minor radius of the magnetic surface. $p_\parallel$ and $p_\perp$ satisfy the following relations,

$$p^2 = p_\parallel^2 + p_\perp^2, \tag{3.1}$$

$$\cos\theta = p_\parallel / p, \tag{3.2}$$

where p is the total momentum and θ denotes the pitch angle. Using these relations, TASK/FP can be expressed in the spherical coordinate system, (p, θ), in the momentum space. In this coordinate system, a divergence of the flux,$\nabla_{p,\rho} \cdot \boldsymbol{S}$, is written in the following expressions,

$$\frac{\partial f}{\partial t} = -\nabla_{p,\rho} \cdot \boldsymbol{S} = -\frac{1}{p^2}\frac{\partial}{\partial p} p^2 S_p - \frac{1}{p \sin\theta}\frac{\partial}{\partial \theta}\sin\theta S_\theta - \frac{1}{\rho}\frac{\partial}{\partial \rho}\rho S_\rho, \tag{3.3}$$

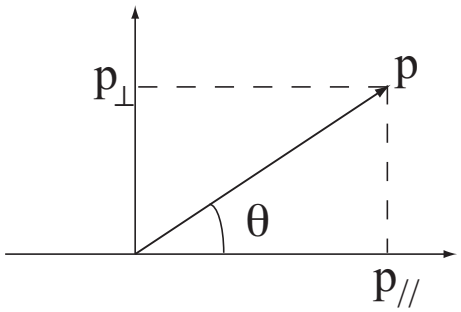

Figure 3.1: The spherical coordinate systems for momentum variables.

where,

$$S_p = -D_{pp}\frac{\partial f}{\partial p} - D_{p\theta}\frac{1}{p}\frac{\partial f}{\partial \theta} + F_p f \tag{3.4}$$

$$S_\theta = -D_{\theta p}\frac{\partial f}{\partial p} - D_{\theta\theta}\frac{1}{p}\frac{\partial f}{\partial \theta} + F_\theta f \tag{3.5}$$

$$S_\rho = -D_\rho\frac{\partial f}{\partial \rho} + F_\rho f. \tag{3.6}$$

It should be noted that the collisional, quasi-linear, and dc electric field fluxes do not contribute to the radial transport, namely $\nabla_\rho \cdot \boldsymbol{S}_{\mathrm{c,ql,dc}} = 0$, in the present analysis. This assumption neglects the finite particle orbit width effect.

In this coordinate system, integration over the momentum becomes

$$\int d\boldsymbol{p} = \int 2\pi p^2 \sin\theta \, dp \, d\theta. \tag{3.7}$$

3.1.2 Fokker-Planck equation

As shown in sec. 1.4.1, Boltzmann eqnation is expressed as

$$\frac{\partial f}{\partial t} + \boldsymbol{v}\cdot\frac{\partial f}{\partial \boldsymbol{r}} + \frac{e}{m}(\boldsymbol{E} + \boldsymbol{v}\times\boldsymbol{B})\cdot\frac{\partial f}{\partial \boldsymbol{v}} = \left(\frac{\partial f}{\partial t}\right)_c.$$

Because collisions in a plasma are primary due to small angle scattering, the collision term, RHS of eq. (1.10), can be expressed as Fokker-Planck type operator, the divergence of a flux;

$$\left(\frac{\partial f}{\partial t}\right)_c = -\nabla_{p,\rho}\cdot\boldsymbol{S}_c^{a/b}, \tag{3.8}$$

where the superscript a/b means that species a collides with species b and the derivative operator means $\nabla_{p,\rho} = \nabla_p + \nabla_\rho$. After averaging over the cyclotron motion in order to derive the drift kinetic equation, averaging over the wave frequency to derive the

quasi-linear operator and averaging over the bounce motion, Boltzmann equation can be written as a Fokker-Planck equation:

$$\frac{\partial f}{\partial t} = -\nabla_{p,\rho} \cdot \boldsymbol{S} + H, \tag{3.9}$$

where

$$\boldsymbol{S} = \boldsymbol{S}_c + \boldsymbol{S}_{\mathrm{ql}} + \boldsymbol{S}_{\mathrm{dc}} + \boldsymbol{S}_{\mathrm{r}} \tag{3.10}$$

denote the collisional, quasi-linear, dc electric field fluxes, and radial diffusion, respectively and H indicates the source term. Generally, the fluxes are composed of two terms, a diffusion term and a friction term,

$$\boldsymbol{S}_s = -\overleftrightarrow{\boldsymbol{D}}_s \cdot \nabla f_s + \boldsymbol{F} f_s, \tag{3.11}$$

subscript "s" indicates the partcile species s.

3.1.3 Relativistic momentum distribution function

In fusion plasmas, the velocity of heated particles becomes very fast. Thus the relativistic effects of fast particles, especially electrons, are important.

The relativistic momentum distribution function satisfies

$$\int f_s(\boldsymbol{p}, \rho) d\boldsymbol{p} = n_s(\rho), \tag{3.12}$$

where $n_s(\rho)$ denotes the density on the normalized minor radius ρ. In particular, the relativistic Maxwellian distribution function has the form [32];

$$f_{s,m}(p, \rho) = \frac{n_s(\rho)}{4\pi m_s^3 c^3 \Theta_s K_2(\Theta_s^{-1})} \exp\left(-\frac{\gamma_s}{\Theta_s}\right), \tag{3.13}$$

where subscript "m" denotes "Maxwell", and $\Theta_s = T_s(\rho)/m_s c^2$, K_n is n-th order modified Bessel function of the second kind, $\gamma_s = \sqrt{1 + p^2/m^2c^2}$, and $T_s(\rho)$ are temperature at ρ.

The plasma averaged kinetic energy density is defined by

$$E_s \equiv \int m_s c^2 (\gamma_s - 1) f_{s,m}(p, \rho)\, d\boldsymbol{p} \tag{3.14}$$

and the relation between E_s and T_s is given by [33]

$$E_s = mc^2 \left(3\Theta_s + \frac{K_1(\Theta_s^{-1})}{K_2(\Theta^{-1})}\right) n_s(\rho). \tag{3.15}$$

In the non-relativistic limit, the averaged kinetic energy density of the plasma E_s is defined by;

$$E_s \equiv \int \frac{p_s^2}{2m_s} f_{s,m}(p, \rho)\, d\boldsymbol{p} \tag{3.16}$$

and the relation between E_s and T_s becomes $E_s = 3n_sT_s/2$.

We define the temperature T_s in the relativistic case as the solution of the relation eq. (3.15). Since this equation can not be solved analytically, because the equation is non-linear with respect to T_s, eq. (3.15) is solved numerically and the temperature T_s in the relativistic case is obtained.

3.1.4 Normalization factors

In TASK/FP, most of variables are normalized because the scale of variables have different order of magnitude for each species. The thermal velocity and momentum, which are the chief normalized factors, are defined as

$$v_{ts0} = \sqrt{\frac{T_{s0}}{m_s}} \tag{3.17}$$

$$p_{ts0} = \sqrt{m_s T_{s0}}, \tag{3.18}$$

where T_{s0} denotes the temperature on the magnetic axis $\rho = 0$ for species s. Using these parameters, the velocity and momentum are normalized as

$$\bar{p}_s \equiv \frac{p_s}{p_{ts0}} \tag{3.19}$$

$$\bar{v}_s \equiv \frac{v_s}{v_{ts0}}. \tag{3.20}$$

Then, the relation between the velocity and the momentum is described as

$$m_s v_s = \frac{p_s}{\gamma_s}, \tag{3.21}$$

where

$$\gamma_s = \left(1 + \frac{p_s^2}{m_s^2 c^2}\right)^{1/2} = \left(1 + \frac{p_{ts0}^2 \bar{p}_s^2}{m_s^2 c^2}\right)^{1/2} = \left(1 + \bar{p}_s{}^2 \Theta_{s0}\right)^{1/2} \tag{3.22}$$

$$\Theta_{s0} = \frac{p_{ts0}^2}{m_s^2 c^2} = \frac{T_{s0}}{m_s c^2}, \tag{3.23}$$

where γ_s is a relativistic factor and $\gamma_s = 1$ in the non-relativistic limit.

Similarly, the momentum distribution function f, the diffusion coefficient $\overleftrightarrow{\boldsymbol{D}}$, and the friction coefficient $\boldsymbol{F}$ are also normalized;

$$\hat{f}(\bar{p}) \equiv p_{t0}^3 f(p) \tag{3.24}$$

$$\hat{\overleftrightarrow{\boldsymbol{D}}} \equiv \frac{\overleftrightarrow{\boldsymbol{D}}}{p_{t0}^2} \tag{3.25}$$

$$\hat{\boldsymbol{F}} \equiv \frac{\boldsymbol{F}}{p_{t0}}. \tag{3.26}$$

3.2 DC electric field term

First, we consider the effect of DC electric field parallel to the magnetic field. Since DC electric field acceleration term is non-diffusive, $\overleftrightarrow{\boldsymbol{D}}_{\rm dc} = \overleftrightarrow{\boldsymbol{0}}$. The friction term is expressed as

$$\boldsymbol{F}_{\rm dc} = \frac{q_s \boldsymbol{E}}{m_s}. \tag{3.27}$$

Thus (p, θ) elements of $\boldsymbol{F}_{\rm dc}$ are

$$F_{{\rm dc},p} = \frac{q_s}{m_s} E_\parallel \cos\theta \tag{3.28}$$

$$F_{{\rm dc},\theta} = \frac{q_s}{m_s} E_\parallel \sin\theta. \tag{3.29}$$

3.3 Coulomb collision term without relativistic effect

The collisional flux is given by the Landau collision integral [34]

$$\boldsymbol{S}^{a/b} = \frac{q_a^2 q_b^2}{8\pi\epsilon_0^2 m_a} \ln\Lambda^{a/b} \int \overleftrightarrow{\boldsymbol{U}}(\boldsymbol{u}) \cdot \left(\frac{f_a(\boldsymbol{v})}{m_b} \frac{\partial f_b(\boldsymbol{v}')}{\partial \boldsymbol{v}'} - \frac{f_b(\boldsymbol{v}')}{m_a} \frac{\partial f_a(\boldsymbol{v})}{\partial \boldsymbol{v}} \right) d^3\boldsymbol{v}' \tag{3.30}$$

where $\boldsymbol{u}$ is the relative velocity $\boldsymbol{u} = \boldsymbol{v} - \boldsymbol{v}'$,

$$\overleftrightarrow{\boldsymbol{U}}(\boldsymbol{u}) = \frac{u^2 \overleftrightarrow{\boldsymbol{I}} - \boldsymbol{u}\boldsymbol{u}}{u^3}, \tag{3.31}$$

and $\ln\Lambda^{a/b} = \ln(2\lambda_D/b_0)$ is the Coulomb logarithm and λ_D and b_0 denote Debye length and impact parameter for 90 degrees scatter. Eq. (3.30) can be rewritten in terms of Rosenbluth potentials [35, 36]:

$$\boldsymbol{S}_c^{a/b} = -\overleftrightarrow{\boldsymbol{D}}_c \nabla f_a(\boldsymbol{v}) + \boldsymbol{F}_c^{a/b} f_a(\boldsymbol{v}) \tag{3.32}$$

$$\overleftrightarrow{\boldsymbol{D}}_c^{a/b} = -\frac{4\pi\Gamma^{a/b}}{n_{b0}} \nabla\nabla\psi_b(\boldsymbol{v}) \tag{3.33}$$

$$\boldsymbol{F}_c^{a/b} = -\frac{4\pi\Gamma^{a/b}}{n_{b0}} \frac{m_a}{m_b} \nabla\phi_b(\boldsymbol{v}), \tag{3.34}$$

where

$$\Gamma^{a/b} = \frac{n_{b0} q_a^2 q_b^2 \ln\Lambda^{a/b}}{4\pi\epsilon_0^2 m_a^2}. \tag{3.35}$$

The functions $\phi_b(\boldsymbol{v})$ and $\psi_b(\boldsymbol{v})$ are called Rosenbluth potentials and defined by:

$$\phi_b(\boldsymbol{v}) = -\frac{1}{4\pi} \int \frac{f_b(\boldsymbol{v}')}{|\boldsymbol{v} - \boldsymbol{v}'|} d^3\boldsymbol{v}' \tag{3.36}$$

$$\psi_b(\boldsymbol{v}) = -\frac{1}{8\pi} \int |\boldsymbol{v} - \boldsymbol{v}'| f_b(\boldsymbol{v}') d^3\boldsymbol{v}'. \tag{3.37}$$

$\nabla\nabla\psi(\boldsymbol{v})$ and $\nabla\phi(\boldsymbol{v})$ are decomposed into the (v, θ) components

$$(\nabla\nabla\psi)_{vv} = \frac{\partial^2\psi}{\partial v^2} \tag{3.38}$$

$$(\nabla\nabla\psi)_{v\theta} = (\nabla\nabla\psi)_{\theta v} = \frac{1}{v}\frac{\partial^2\psi}{\partial v\partial\theta} - \frac{1}{v^2}\frac{\partial\psi}{\partial\theta} \tag{3.39}$$

$$(\nabla\nabla\psi)_{\theta\theta} = \frac{1}{v}\frac{\partial\psi}{\partial v} + \frac{1}{v^2}\frac{\partial^2\psi}{\partial\theta^2} \tag{3.40}$$

$$(\nabla\phi)_v = \frac{\partial\phi}{\partial v} \tag{3.41}$$

$$(\nabla\phi)_\theta = \frac{1}{v}\frac{\partial\phi}{\partial\theta}. \tag{3.42}$$

3.3.1 Linear collision model

If the background momentum distribution function is Maxwellian, the diffusion and friction coefficients are calculated analytically to obtain [37],

$$\hat{D}_{cpp} = \frac{\hat{\Gamma}^{a/b}v_{ta0}}{2\sqrt{2}v_{tb0}}\left(\frac{\mathrm{erf}(u)}{u^3} - \frac{\mathrm{erf}'(u)}{u^2}\right) \tag{3.43}$$

$$\hat{D}_{c\theta\theta} = \frac{\hat{\Gamma}^{a/b}v_{ta0}}{4\sqrt{2}v_{tb0}}\left(\frac{2\mathrm{erf}(u)}{u} - \frac{\mathrm{erf}}{u^3} + \frac{\mathrm{erf}'(u)}{u^2}\right) \tag{3.44}$$

$$\hat{F}_{cp} = -\hat{\Gamma}^{a/b}\frac{v_{ta0}^2}{2v_{tb0}^2}\frac{m_a}{m_b}\left(\frac{\mathrm{erf}(u)}{u^2} - \frac{\mathrm{erf}'(u)}{u}\right), \tag{3.45}$$

where

$$\hat{\Gamma}^{a/b} = \frac{n_{b0}q_a^2q_b^2\ln\lambda^{a/b}m_a}{4\pi\epsilon_0^2m_a^2p_{ta0}^3} = \Gamma^{a/b}\frac{m_a}{p_{ta0}^3}, \tag{3.46}$$

$u = v_a/\sqrt{2}v_{tb0}$, and the error function $\mathrm{erf}(u)$ and its derivative $\mathrm{erf}'(u)$ are defined by

$$\mathrm{erf}(u) = \frac{2}{\sqrt{\pi}}\int_0^u \exp(-x^2)dx \tag{3.47}$$

$$\mathrm{erf}'(u) = \frac{2}{\sqrt{\pi}}\exp(-u^2). \tag{3.48}$$

In the limit of $u \to 0$, eq. (3.43)~(3.45) are simplified as

$$\hat{D}_{cpp} \to \hat{\Gamma}^{a/b}\frac{2v_{ta0}}{3\sqrt{2\pi}v_{tb0}} \tag{3.49}$$

$$\hat{D}_{c\theta\theta} \to \hat{\Gamma}^{a/b}\frac{2v_{ta0}}{3\sqrt{2\pi}v_{tb0}} \tag{3.50}$$

$$\hat{F}_{cp} \to 0. \tag{3.51}$$

where the relation [1]

$$\lim_{u\to 0}\left(\mathrm{erf}(u) - u\,\mathrm{erf}'(u)\right) = \frac{4}{3\sqrt{\pi}}u^3 \tag{3.53}$$

is used.

3.3.2 Legendre expansion

In the linear collision model, the momentum distribution function in the integrand of Rosenbluth potentials, eq. (3.36) and (3.37), is assumed to be Maxwellian and the integration is carried out analytically. In the case of non-Maxwellian distribution function, however, it is required to calculate the integration numeically, and it costs a lot of computational resources.

In order to reduce the required computational resources, it is sometimes useful to decompose the momentum distribution function and potentials into the Legendre harmonics, $P_l(\cos\theta)$. The momentum distribution function $f(p,\theta)$ and Rosenbluth potentials $\phi_b(\boldsymbol{v})$ and $\psi_b(\boldsymbol{v})$ are expressed in terms of the Legendre expansion [35]:

$$f(p,\theta) = \sum_{l=0}^{\infty} f^{(l)}(p)P_l(\cos\theta) \tag{3.54}$$

$$\phi_b(v,\theta) = \sum_{l=0}^{\infty} \phi^{(l)}(v)P_l(\cos\theta) \tag{3.55}$$

$$\psi_b(v,\theta) = \sum_{l=0}^{\infty} \psi^{(l)}(v)P_l(\cos\theta) \tag{3.56}$$

where

$$f^{(l)}(p) = \frac{2l+1}{2}\int_0^{\pi} f(p,\theta)P_l(\cos\theta)\sin\theta d\theta \tag{3.57}$$

$$\phi_b^{(l)}(v) = -\frac{1}{2l+1}\left[v^{-l-1}N_l(v) + v^l M_l(v)\right] \tag{3.58}$$

$$\psi_b^{(l)}(v) = \frac{1}{2(4l^2-1)}\left[v^{-l+1}N_l(v) + v^l M_l^+(v) - \frac{l-1/2}{l+3/2}\left\{v^{-l-1}N_l^+(v) + v^{l+2}M_l(v)\right\}\right]. \tag{3.59}$$

[1] Taylor expansion of the error function $\mathrm{erf}(u)$ is

$$\mathrm{erf}(u) = \frac{2}{\sqrt{\pi}}\left(u - \frac{u^3}{3} + \frac{u^5}{10} - \cdots\right). \tag{3.52}$$

The four functionals of $\phi_b^{(l)}(v)$ and $\psi_b^{(l)}(v)$ are defined as:

$$M_l(v) \equiv \int_v^\infty v'^{1-l} f_b^{(l)}(v') dv' \tag{3.60}$$

$$N_l(v) \equiv \int_0^v v'^{2+l} f_b^{(l)}(v') dv' \tag{3.61}$$

$$M_l^+(v) \equiv \int_v^\infty v'^{3-l} f_b^{(l)}(v') dv' \tag{3.62}$$

$$N_l^+(v) \equiv \int_0^v v'^{4+l} f_b^{(l)}(v') dv' \tag{3.63}$$

For simplicity, the valiable of radial position ρ is omitted.

Usually, we choose the value of the upper limit in the sum in eq. (3.56) $l_{\max} = 2$. Since the number of numerical grid of the valiable θ is the order of 100, Legendre expansion enable us to compute the collision term with less resources.

3.3.3 Normalized potentials

The functionals, eq. (3.60)~(3.63), can be written as a function of momentum;

$$M_l(p) = \int_{\frac{m_b}{m_a}p}^\infty v'^{-1-l} p'^2 f_b^{(l)}(p') dp' \tag{3.64}$$

$$N_l(p) = \int_0^{\frac{m_b}{m_a}p} v_b'^l p'^2 f_b^{(l)}(p') dp' \tag{3.65}$$

$$M_l^+(p) = \int_{\frac{m_b}{m_a}p}^\infty v'^{1-l} p'^2 f_b^{(l)}(p') dp' \tag{3.66}$$

$$N_l^+(p) = \int_0^{\frac{m_b}{m_a}p} v'^{l+2} p'^2 f_b^{(l)}(p') dp'. \tag{3.67}$$

By the use of $\hat{f}$, $\bar{p}$, and $v_a = p_{ta0}\bar{p}/m_a\gamma_a$, normalized functionals, $\hat{M}_l$, $\hat{N}_l$, $\hat{M}_l^+$, and $\hat{N}_l^+$, are defined as;

$$M_l(\bar{p}) = \left(\frac{p_{tb0}}{m_b}\right)^{-l-1} \int_{p_c}^\infty \left(\frac{1}{\gamma_b}\right)^{-l-1} \bar{p}'^{(1-l)} \hat{f}_b^{(l)}(\bar{p}') d\bar{p}' = \left(\frac{p_{tb0}}{m_b}\right)^{-l-1} \hat{M}_l(\bar{p}) \tag{3.68}$$

$$N_l(\bar{p}) = \left(\frac{p_{tb0}}{m_b}\right)^{l} \int_0^{p_c} \left(\frac{1}{\gamma_b}\right)^{l} \bar{p}'^{(2+l)} \hat{f}_b^{(l)}(\bar{p}') d\bar{p}' = \left(\frac{p_{tb0}}{m_b}\right)^{l} \hat{N}_l(\bar{p}) \tag{3.69}$$

$$M_l^+(\bar{p}) = \left(\frac{p_{tb0}}{m_b}\right)^{-l+1} \int_{p_c}^\infty \left(\frac{1}{\gamma_b}\right)^{-l+1} \bar{p}'^{(3-l)} \hat{f}_b^{(l)}(\bar{p}') d\bar{p}' = \left(\frac{p_{tb0}}{m_b}\right)^{-l+1} \hat{M}_l^+(\bar{p}) \tag{3.70}$$

$$N_l^+(\bar{p}) = \left(\frac{p_{tb0}}{m_b}\right)^{l+2} \int_0^{p_c} \left(\frac{1}{\gamma_b}\right)^{l+2} \bar{p}'^{(4+l)} \hat{f}_b^{(l)}(\bar{p}') d\bar{p}' = \left(\frac{p_{tb0}}{m_b}\right)^{l+2} \hat{N}_l^+(\bar{p}), \tag{3.71}$$

where

$$p_c^2 = \frac{v_t^2}{1 - \Theta_{b0} v_t^2 (\bar{p}/\gamma_a)^2} \left(\frac{\bar{p}}{\gamma_a}\right)^2 \tag{3.72}$$
$$v_t \equiv \frac{m_b p_{ta0}}{m_a p_{tb0}}.$$

Similarly, eq. (3.58) and (3.59) can be rewritten in term of normalized quantities;

$$\phi_b^{(l)}(\bar{p}) = -\frac{1}{2l+1}\left[\left(\frac{p_{ta0}\bar{p}}{m_a\gamma_a}\right)^{-l-1}\left(\frac{p_{tb0}}{m_b}\right)^l \hat{N}_l(\bar{p}) + \left(\frac{p_{ta0}\bar{p}}{m_a\gamma_a}\right)^{l}\left(\frac{p_{tb0}}{m_b}\right)^{-l-1}\hat{M}_l(\bar{p})\right] \tag{3.73}$$

$$\psi_b^{(l)}(\bar{p}) = \frac{1}{2(4l^2-1)}\left[\left(\frac{p_{ta0}\bar{p}}{m_a\gamma_a}\right)^{-l+1}\left(\frac{p_{tb0}}{m_b}\right)^l \hat{N}_l(\bar{p}) + \left(\frac{p_{ta0}\bar{p}}{m_a\gamma_a}\right)^{l}\left(\frac{p_{tb0}}{m_b}\right)^{-l+1}\hat{M}_l^+(\bar{p}) \right.$$
$$\left. -\frac{l-1/2}{l+3/2}\left\{\left(\frac{p_{ta0}\bar{p}}{m_a\gamma_a}\right)^{-l-1}\left(\frac{p_{tb0}}{m_b}\right)^{l+2}\hat{N}_l^+(\bar{p}) + \left(\frac{p_{ta0}\bar{p}}{m_a\gamma_a}\right)^{l+2}\left(\frac{p_{tb0}}{m_b}\right)^{-l-1}\hat{M}_l(\bar{p})\right\}\right]. \tag{3.74}$$

Here, the normalized Rosenbluth potentials, $\hat{\phi}_b \equiv \frac{p_{tb0}}{m_b}\phi_b$ and $\hat{\psi}_b \equiv \frac{m_b}{p_{tb0}}\psi_b$ are introduced and then their Legendre expansion, $\hat{\phi}_b^{(l)}$ and $\hat{\psi}_b^{(l)}$ are expressed as;

$$\hat{\phi}_b^{(l)}(\bar{p}) = -\frac{1}{2l+1}\left(\frac{m_b p_{ta0}}{m_a p_{tb0}}\right)\left[p_d^{-l-1}\hat{N}_l + p_d^l \hat{M}_l\right] \tag{3.75}$$

$$\hat{\psi}_b^{(l)}(\bar{p}) = \frac{1}{2(4l^2-1)}\left(\frac{m_a p_{tb0}}{m_b p_{ta0}}\right)\left[p_d^{-l+1}\hat{N}_l + p_d^l\hat{M}_l^+ - \frac{l-1/2}{l+3/2}\left\{p_d^{-l-1}\hat{N}_l^+ + p_d^{l+2}\hat{M}_l\right\}\right]. \tag{3.76}$$

where $p_d \equiv \frac{m_b p_{ta0}\bar{p}}{m_a p_{tb0}\gamma_a}$.

3.3.4 Non-linear collision coefficients

Using eq. (3.25), (3.26), (3.33), (3.34), and (3.38)~(3.42), the normalized diffusion and friction coefficients can be written in terms of normalized Rosenbluth potentials for each components;

$$\hat{D}_{cpp} = -\frac{4\pi\hat{\Gamma}}{n_{b0}}\gamma_a^6\frac{\partial^2\hat{\psi}}{\partial\bar{p}^2} \tag{3.77}$$

$$\hat{D}_{cp\theta} = -\frac{4\pi\hat{\Gamma}}{n_{b0}}\left(\gamma_a^4\frac{1}{\bar{p}}\frac{\partial^2\hat{\psi}}{\partial\bar{p}\partial\theta} - \gamma_a^2\frac{1}{\bar{p}^2}\frac{\partial\hat{\psi}}{\partial\theta}\right) \tag{3.78}$$

$$\hat{D}_{c\theta\theta} = -\frac{4\pi\hat{\Gamma}}{n_{b0}}\left(\gamma_a^4\frac{1}{\bar{p}}\frac{\partial\hat{\psi}}{\partial\bar{p}} + \gamma_a^2\frac{1}{\bar{p}^2}\frac{\partial^2\hat{\psi}}{\partial\theta^2}\right) \tag{3.79}$$

$$\hat{F}_{cp} = -\frac{4\pi\hat{\Gamma}}{n_{b0}}\left(\frac{m_a}{m_b}\right)\gamma_a^3\frac{\partial\hat{\phi}}{\partial\bar{p}} \tag{3.80}$$

$$\hat{F}_{c\theta} = -\frac{4\pi\hat{\Gamma}}{n_{b0}}\left(\frac{m_a}{m_b}\right)\gamma_a\frac{1}{\bar{p}}\frac{\partial\hat{\phi}}{\partial\theta} \tag{3.81}$$

Since the normalized Rosenbluth potentials are also expanded in terms of the Legendre polimoninals, the derivatives of the potentials in eq. (3.77)~(3.81) are expressed as

$$\frac{\partial^2\hat{\psi}}{\partial\bar{p}^2} = \sum_l \frac{\partial^2\hat{\psi}^{(l)}(\bar{p})}{\partial\bar{p}^2}P_l \tag{3.82}$$

$$\frac{\partial^2\hat{\psi}}{\partial\bar{p}\partial\theta} = \sum_l \frac{\partial\hat{\psi}^{(l)}}{\partial\bar{p}}\frac{\partial P_l}{\partial\theta} \tag{3.83}$$

$$\frac{\partial^2\hat{\psi}}{\partial\theta^2} = \sum_l \hat{\psi}^{(l)}\frac{\partial^2 P_l}{\partial\theta^2} \tag{3.84}$$

$$\frac{\partial\hat{\psi}}{\partial\bar{p}} = \sum_l \frac{\partial\hat{\psi}^{(l)}}{\partial\bar{p}}P_l \tag{3.85}$$

$$\frac{\partial\hat{\psi}}{\partial\theta} = \sum_l \hat{\psi}^{(l)}\frac{\partial P_l}{\partial\theta} \tag{3.86}$$

$$\frac{\partial\hat{\phi}}{\partial\bar{p}} = \sum_l \frac{\partial\hat{\phi}^{(l)}}{\partial\bar{p}}P_l \tag{3.87}$$

$$\frac{\partial\hat{\phi}}{\partial\theta} = \sum_l \hat{\phi}^{(l)}\frac{\partial P_l}{\partial\theta}. \tag{3.88}$$

where the argument of $P_l(\cos\theta)$ is omitted for simplicity. These derivatives are calculated by the relation ;

$$\frac{\partial\hat{\phi}^{(l)}}{\partial\bar{p}} = -\frac{1}{2l+1}\left(\frac{m_b p_{ta0}}{m_a p_{tb0}}\right)^2 \gamma_a^{-3}\left[-(l+1)p_d^{-(l+2)}\hat{N}_l + l p_d^{l-1}\hat{M}_l\right] \tag{3.89}$$

$$\begin{aligned}\frac{\partial\hat{\psi}^{(l)}}{\partial\bar{p}} = \frac{\gamma_a^{-3}}{2(4l^2-1)}\Big[&-(l-1)p_d^{-l}\hat{N}_l + l p_d^{l-1}\hat{M}_l^+ \\ &-\frac{l-1/2}{l+3/2}\left\{-(l+1)p_d^{-l-2}\hat{N}_l^+ + (l+2)p_d^{l+1}\hat{M}_l\right\}\Big]\end{aligned} \tag{3.90}$$

$$\begin{aligned}\frac{\partial^2\hat{\psi}^{(l)}}{\partial\bar{p}^2} = \left(\frac{m_b p_{ta0}}{m_a p_{tb0}}\right)\frac{\gamma_a^{-6}}{2(4l^2-1)}\Big[&l(l-1)\left\{p_d^{-l-1}\hat{N}_l + p_d^{l-2}\hat{M}_l^+\right\} \\ &-\frac{l-1/2}{l+3/2}\left\{(l+1)(l+2)\left(p_d^{-l-3}\hat{N}_l^+ + p_d^l\hat{M}_l\right)\right\}\Big]\end{aligned} \tag{3.91}$$

$$\frac{\partial P_l(\mu)}{\partial\theta} = \frac{l}{\sin\theta}\left\{\mu P_l(\mu) - P_{l-1}(\mu)\right\} \tag{3.92}$$

$$\frac{\partial^2 P_l}{\partial\theta^2} = -\left(\frac{l}{\sin^2\theta} + l^2\right)P_l + \frac{l\cos\theta}{\sin^2\theta}P_{l-1}, \tag{3.93}$$

where $\mu = \cos\theta$. The derivation of these relations are given in Appendix A.1.

3.4 Coulomb collision term with relativistic effect

The relativistic collision operator is given by Beliaev and Budker [38]. The collision term for a plasma of species a colliding of species b may be written in Fokker-Planck form as:

$$-\nabla \cdot \boldsymbol{S}_c^{a/b} = \frac{\partial}{\partial \boldsymbol{u}} \cdot \left(\overleftrightarrow{\boldsymbol{D}}^{a/b} \cdot \frac{\partial f_a}{\partial \boldsymbol{u}} - \boldsymbol{F}^{a/b} f_a \right) \tag{3.94}$$

where the diffusion and friction coefficients are given by

$$\overleftrightarrow{\boldsymbol{D}}^{a/b}(\boldsymbol{u}) = \frac{\Gamma^{a/b}}{2n_b} \int \overleftrightarrow{\boldsymbol{U}}(\boldsymbol{u}, \boldsymbol{u}') f_a(\boldsymbol{u}') d^3\boldsymbol{u}' \tag{3.95}$$

$$\boldsymbol{F}^{a/b}(\boldsymbol{u}) = -\frac{\Gamma^{a/b}}{2n_a} \frac{m_a}{m_b} \int \left(\frac{\partial}{\partial \boldsymbol{u}'} \cdot \overleftrightarrow{\boldsymbol{U}}(\boldsymbol{u}, \boldsymbol{u}') \right) f_b(\boldsymbol{u}') d^3\boldsymbol{u}', \tag{3.96}$$

where $\boldsymbol{u}$ is the momentum per unit rest mass. In the relativistic case, the kernel $\overleftrightarrow{\boldsymbol{U}}$ is given by [38]

$$\overleftrightarrow{\boldsymbol{U}}(\boldsymbol{u}, \boldsymbol{u}') = \frac{r^2}{\gamma\gamma'\omega} \left(\omega^2 \overleftrightarrow{\boldsymbol{I}} - \boldsymbol{u}\boldsymbol{u} - \boldsymbol{u}'\boldsymbol{u}' + r(\boldsymbol{u}\boldsymbol{u}' + \boldsymbol{u}'\boldsymbol{u}) \right), \tag{3.97}$$

where

$$r = \gamma\gamma' - \boldsymbol{u} \cdot \boldsymbol{u}'/c^2 \tag{3.98}$$

$$\omega = c\sqrt{r^2 - 1}. \tag{3.99}$$

3.4.1 Potentials for relativistic collision operator

Braams and Karney [39, 40] formulated the relativistic collision operator in terms of five scalar potentials:

$$\begin{aligned}
\Psi_{s'[1]0}(\boldsymbol{u}) &= -\frac{1}{4\pi} \int \omega^{-1} f_{s'}(\boldsymbol{u}') \frac{d^3\boldsymbol{u}'}{\gamma'} \\
\Psi_{s'[2]02}(\boldsymbol{u}) &= -\frac{1}{8\pi} \int \omega f_{s'}(\boldsymbol{u}') \frac{d^3\boldsymbol{u}}{\gamma'} \\
\Psi_{s'[3]022}(\boldsymbol{u}) &= -\frac{1}{32\pi} \int c^3 \left(r \sinh^{-1}(\omega/c) - \omega/c \right) f_{s'}(\boldsymbol{u}') \frac{d^3\boldsymbol{u}'}{\gamma'} \\
\Psi_{s'[1]1}(\boldsymbol{u}) &= -\frac{1}{4\pi} r\omega^{-1} f_{s'}(\boldsymbol{u}') \frac{d^3\boldsymbol{u}'}{\gamma'} \\
\Psi_{s'[2]11}(\boldsymbol{u}) &= -\frac{1}{8\pi} \int c \sinh^{-1}(\omega/c) f_{s'}(\boldsymbol{u}') \frac{d^3\boldsymbol{u}'}{\gamma'}.
\end{aligned} \tag{3.100}$$

These potentials satisfy the following equations

$$\begin{aligned} L_0\Psi_{s'[1]0} &= f_{s'} \\ L_2\Psi_{s'[2]02} &= \Psi_{s'[1]0} \\ L_2\Psi_{s'[3]022} &= \Psi_{s'[2]02} \\ L_1\Psi_{s'[1]1} &= f_{s'} \\ L_1\Psi_{s'[2]11} &= \Psi_{s'[1]1} \end{aligned} \tag{3.101}$$

where

$$L_a\Psi = \left(\overleftrightarrow{\boldsymbol{I}} + \frac{\boldsymbol{uu}}{c^2}\right) : \frac{\partial^2\Psi}{\partial\boldsymbol{u}\partial\boldsymbol{u}} + \frac{3\boldsymbol{u}}{c^2}\cdot\frac{\partial\Psi}{\partial\boldsymbol{u}} + \frac{1-a^2}{c^2}\Psi \tag{3.102}$$

and "a" is a positive integer. Eqs. (3.101) can be expressed in the concise form

$$L_a\Psi_{s'[k+1]*a} = \Psi_{s'[k]*}. \tag{3.103}$$

The notations of the potentials used in ref. [40] are employed in the following.

In terms of these potentials, the diffusion and friction coefficients are expressed in the following form [40]:

$$\overleftrightarrow{\boldsymbol{D}}^{s/s'}(\boldsymbol{u}) = -\frac{4\pi\gamma^{s/s'}}{n'_s}\left[\frac{1}{\gamma}\left(\overleftrightarrow{\boldsymbol{L}} + \frac{\overleftrightarrow{\boldsymbol{I}}}{c^2} + \frac{\boldsymbol{uu}}{c^4}\right)\Psi_{s'[2]02} - \frac{4}{\gamma c^2}\left(\overleftrightarrow{\boldsymbol{L}} - \frac{\overleftrightarrow{\boldsymbol{I}}}{c^2} - \frac{\boldsymbol{uu}}{c^4}\right)\Psi_{s'[3]022}\right] \tag{3.104}$$

$$\boldsymbol{F}^{s/s'}(\boldsymbol{u}) = -\frac{4\pi\gamma^{s/s'}}{n'_s}\frac{m_s}{m_{s'}}\frac{1}{\gamma}\left[\boldsymbol{K}\Psi_{s'[1]1} - \frac{2}{c^2}\boldsymbol{K}\Psi_{s'[2]11}\right], \tag{3.105}$$

where

$$\overleftrightarrow{\boldsymbol{L}}\Psi(\boldsymbol{u}) = \left(\overleftrightarrow{\boldsymbol{I}} + \frac{\boldsymbol{uu}}{c^2}\right)\cdot\frac{\partial^2\Psi}{\partial\boldsymbol{u}\partial\boldsymbol{u}}\cdot\left(\overleftrightarrow{\boldsymbol{I}} + \frac{\boldsymbol{uu}}{c^2}\right) + \left(\overleftrightarrow{\boldsymbol{I}} + \frac{\boldsymbol{uu}}{c^2}\right)\left(\boldsymbol{u}\cdot\frac{\partial\Psi}{\partial\boldsymbol{u}}\right) \tag{3.106}$$

$$\boldsymbol{K}\Psi(\boldsymbol{u}) = \left(\overleftrightarrow{\boldsymbol{I}} + \frac{\boldsymbol{uu}}{c^2}\right)\cdot\frac{\partial\Psi}{\partial\boldsymbol{u}}. \tag{3.107}$$

In the spherical coordinate system, now we assume azimuthal symmetry, that is, $\partial/\partial\phi = 0$. The components of the operators $\overleftrightarrow{\boldsymbol{L}}$ and $\boldsymbol{K}$ become [40]:

$$\begin{aligned} L_{uu}\Psi &= \gamma^4\frac{\partial^2\Psi}{\partial u^2} + \frac{\gamma^2 u}{c^2}\frac{\partial\Psi}{\partial u} \\ L_{\theta\theta}\Psi &= \frac{1}{u^2}\frac{\partial^2\Psi}{\partial\theta^2} + \frac{\gamma^2}{u}\frac{\Psi}{u} \\ L_{u\theta}\Psi &= L_{\theta u}\Psi = \frac{\gamma^2}{u}\left(\frac{\partial^2\Psi}{\partial u\partial\theta} - \frac{1}{u}\frac{\partial\Psi}{\partial\theta}\right) \\ K_u\Psi &= \gamma^2\frac{\partial\Psi}{\partial u} \\ K_\theta\Psi &= \frac{1}{u}\frac{\partial\Psi}{\partial\theta}. \end{aligned} \tag{3.108}$$

Similarly, the operator L_a (eq. (3.102)) becomes

$$L_a\Psi = \gamma^2\frac{\partial^2\Psi}{\partial u^2} + \left(\frac{2}{u} + \frac{3u}{c^2}\right)\frac{\partial\Psi}{\partial u} + \frac{1}{u^2}\left(\frac{\partial^2\Psi}{\partial\theta^2} + \cot\theta\frac{\partial\Psi}{\partial\theta}\right) + \frac{1-a^2}{c^2}\Psi. \tag{3.109}$$

3.4.2 Legendre expansion

Similarly to the case of non-relativistic collision term, the momentum distribution function, the potentials, and the operators are expanded in terms of Legendre harmonics. The potentials are expanded as:

$$\Psi_{[k]*}(\boldsymbol{u}) = \sum_{l=0}^{\infty} \psi_{l[k]*}(u) P_l(\cos\theta). \tag{3.110}$$

Eq. (3.101) becomes

$$L_{l,a}\psi_{l[k+1]*a} = \psi_{l[k]*}, \tag{3.111}$$

where eq. (3.109) is rewritten as

$$L_{l,a}\psi(u) = \left(1 + \frac{u^2}{c^2}\right)\frac{d^2\psi}{du^2} + \left(\frac{2}{u} + \frac{3u}{c^2}\right)\frac{d\psi}{du} - \left(\frac{l(l+1)}{u^2} + \frac{a^2-1}{c^2}\right)\psi. \tag{3.112}$$

The coefficient $\psi_{l[k]*}$ of the Legendre expansion of the potential is expressed as:

$$\psi_{l[k]*}(u) = \int_0^u N_{l[k]*}(u,u')\frac{u'^2}{\gamma'} f^{(l)}(u')du' + \int_u^\infty N_{l[k]*}(u',u)\frac{u'^2}{\gamma'} f^{(l)}(u')du'. \tag{3.113}$$

The kernel function $N_{l[n]*}(u,u')$ is defined by

$$\begin{aligned}
N_{l[0]}(u,u') &= 0 \\
N_{l[1]a}(u,u') &= c^{-1} y_{l[1]a}(u/c) j_{l[1]a}(u'/c) \\
N_{l[2]aa'}(u,u') &= c\left[y_{l[1]a}(u/c) j_{l[2]aa'}(u'/c) + y_{l[2]aa'}(u/c) j_{l[1]a'}(u'/c)\right] \\
N_{l[3]aa'a''}(u,u') &= c^3\left[y_{l[1]a}(u/c) j_{l[3]aa'a''}(u'/c) + y_{l[2]aa'}(u/c) j_{l[2]a'a''}(u'/c)\right. \\
&\quad \left. + y_{l[3]aa'a''}(u/c) j_{l[1]a''}(u'/c)\right],
\end{aligned} \tag{3.114}$$

and

$$\begin{aligned}
j_{l[1]a}(u/c) &= \sqrt{\pi c/2u} P^{-l-1/2}_{a-1/2}(\gamma) \\
y_{l[1]a}(u/c) &= (-1)^{-l-1}\sqrt{\pi c/2u} P^{l+1/2}_{a-1/2}(\gamma).
\end{aligned} \tag{3.115}$$

where P^μ_ν is the associated Legendre function of the first kind. The functions, $j_{l[k]*}$ and $y_{l[k]*}$, satisfy the relations $j_{l[k]*}(-z) = (-1)^l j_{l[k]*}(z)$ and $y_{l[k]*}(-z) = (-1)^l y_{l[k]*}(z)$, and they are related with each other:

$$y_{l[k]*} = (-1)^{l+1} j_{-l-1[k]*}. \tag{3.116}$$

The derivative of these functions are

$$\begin{aligned}
\frac{d}{du} j_{l[k]*} &= \frac{1}{c\gamma} j_{l-1[k]*} - \frac{l+1}{u} j_{l[k]*} \\
\frac{d}{du} y_{l[k]*} &= -\frac{1}{c\gamma} y_{l+1[k]*} + \frac{l}{u} y_{l[k]*}.
\end{aligned} \tag{3.117}$$

The argument of these functions, $z = u/c$, is omitted for simplicity. The functions, $j_{l[k]*}$ and $y_{l[k]*}$, for $k = 2,\ 3$ are expressed in terms of $j_{l[1]*}$ and $y_{l[1]*}$:

$$
\begin{aligned}
j_{l[2]02} &= \frac{u}{2c} j_{l+1[1]1} \\
y_{l[2]02} &= -\frac{u}{2c} y_{l-1[1]1} \\
j_{l[2]11} &= \frac{u}{2c} j_{l+1[1]0} \\
y_{l[2]11} &= -\frac{u}{2c} y_{l-1[1]0} \\
j_{l[2]22} &= \frac{u}{2c}\left(j_{l+1[1]1} + \frac{u}{c} j_{l+2[1]0}\right) \\
y_{l[2]22} &= -\frac{u}{2c}\left(y_{l-1[1]1} - \frac{u}{2c} y_{l-2[1]0}\right) \\
j_{l[3]022} &= \frac{u^2}{8c^2} j_{l+2[1]0} \\
y_{l[3]022} &= -\frac{u^2}{8c^2} y_{l-2[1]0}.
\end{aligned}
\tag{3.118}
$$

The detailed derivation of the functions $j_{l[k]*}$ and $y_{l[k]*}$ are expressed in the Appendix A.2.

3.4.3 Non-linear coollision coefficients

Using eqs. (3.104), (3.105), (3.108), (3.110), (3.111), and (3.112), the coefficients of the Legendre expansion of the diffusion and friction coefficients in momentum spherical coordinate with azimuthal symmetry are given by

$$
\begin{aligned}
D^{s/s'}_{luu} &= \frac{4\pi\Gamma^{s/s'}}{n_{s'}}\frac{\gamma}{u}\left[2\gamma^2\frac{\partial\psi_{s'l[2]02}}{\partial u} - \frac{8\gamma^2}{c^2}\frac{\partial\psi_{s'l[3]022}}{\partial u} - u\psi_{s'l[1]0}\right. \\
&\quad \left. -\frac{l(l+1)}{u}\psi_{s'l[2]02} + \left(\frac{8u}{c^4} + \frac{4l(l+1)}{uc^2}\right)\psi_{s'l[3]022}\right] P_l(\mu) \\
D^{s/s'}_{l\theta\theta} &= \frac{4\pi\Gamma^{s/s'}}{n_{s'}}\frac{1}{\gamma u}\left[-\gamma^2\frac{\partial\psi_{s'l[2]02}}{\partial u}P_l(\mu) - \left(\frac{u}{c^2}P_l(\mu) + \frac{1}{u}\frac{\partial^2 P_l(\mu)}{\partial\theta^2}\right)\psi_{s'l[2]02}\right. \\
&\quad \left. +\frac{4\gamma^2}{c^2}\frac{\partial\psi_{s'l[3]022}}{\partial u} - \left(\frac{4u}{c^4}P_l(\mu) - \frac{4}{uc^2}\frac{\partial^2 P_l(\mu)}{\partial\theta^2}\right)\psi_{s'l[3]022}\right] \\
D^{s/s'}_{lu\theta} &= \frac{4\pi\Gamma^{s/s'}}{n_{s'}}\frac{\gamma}{u}\left[\frac{4}{c^2}\frac{\partial\psi_{l[3]022}}{\partial u} - \frac{\partial\psi_{l[2]02}}{\partial u} - \frac{4}{uc^2}\psi_{l[3]022} + \frac{1}{u}\psi_{s'[2]02}\right]\frac{\partial P_l(\mu)}{\partial\theta} \\
F^{s/s'}_{lu} &= -\frac{\partial\psi_{l[2]02}}{\partial u}\frac{m_s}{m_{s'}}\gamma\left(-\frac{\partial\psi_{l[1]1}}{\partial u} + \frac{2}{c^2}\frac{\partial\psi_{l[2]11}}{\partial u}\right)P_l(\mu) \\
F^{s/s'}_{l\theta} &= -\frac{\partial\psi_{l[2]02}}{\partial u}\frac{m_s}{m_{s'}}\frac{1}{\gamma u}\left(-\psi_{l[1]1} + \frac{2}{c^2}\psi_{l[2]11}\right)\frac{\partial P_l(\mu)}{\partial\theta}.
\end{aligned}
\tag{3.119}
$$

The expression for , $l \leq 1$, is given in Ref. [40]. In order to satisfy the energy conservation, we formulate up tp $l = 2$.

Now we consider to express the potentials, $\psi_{l[k]*}$, and its derivatives in Eqs. (3.119) in terms of $j_{l[1]*}$, and $y_{l[1]*}$. We define the abbreviations of the integrals as follow:

$$
\begin{aligned}
J_a^{+i} &\equiv \int_0^u \frac{u'^{2+i}}{\gamma'} j'_{l+i[1]a} f^{(l)}(u') du' \\
Y_a^{-i} &\equiv \int_u^\infty \frac{u'^{2+i}}{\gamma'} y'_{l-i[1]a} f^{(l)}(u') du',
\end{aligned}
\tag{3.120}
$$

where $j'_{l[k]*} = j_{l[k]*}(u'/c)$ and $y'_{l[k]*} = y_{l[k]*}(u'/c)$.

Using these notations, potentials, $\psi_{l[k]*}$, and their derivatives are expressed as follow:

$$
\begin{aligned}
\psi_{l[1]0} &= \frac{1}{c}[y_{l[1]0} J_0^{+0} + j_{l[1]0} Y_0^{-0}] \\
\psi_{l[1]1} &= \frac{1}{c}[y_{l[1]1} J_1^{+0} + j_{l[1]1} Y_1^{-0}] \\
\psi_{l[2]02} &= \frac{1}{2}[y_{l[1]0} J_1^{+1} - u y_{l-1[1]1} J_2^{+0} + u j_{l+1[1]1} Y_0^{-0} - j_{l[1]2} Y_1^{-1}] \\
\psi_{l[2]11} &= \frac{1}{2}[y_{l[1]1} J_0^{+1} - u y_{l-1[1]0} J_1^{+0} + u j_{l+1[1]0} Y_1^{-0} - j_{l[1]1} Y_0^{-1}] \\
\psi_{l[3]022} &= \frac{c}{8}\left[y_{l[1]0} J_0^{+2} - 2u y_{l-1[1]1} \left(J_1^{+1} + \frac{1}{c} J_0^{+2} \right) + u^2 y_{l-2[1]0} J_2^{+0} + u^2 j_{l+2[1]0} Y_0^{-0} \right. \\
&\quad \left. -2u \left(j_{l+1[1]1} + \frac{u}{c} j_{l+2[1]0} \right) Y_1^{-1} + j_{l[1]2} Y_0^{-2} \right]
\end{aligned}
$$

$$
\begin{aligned}
\frac{\partial \psi_{l[1]1}}{\partial u} &= \frac{1}{c}\left[\frac{\partial y_{l[1]1}}{\partial u} J_1^{+0} + \frac{\partial j_{l[1]1}}{Y}{}_1^{-0} \right] \\
\frac{\partial \psi_{l[2]02}}{\partial u} &= \frac{1}{2}\left[\frac{\partial y_{l[1]0}}{\partial u} J_1^{+1} - \left(y_{l-1[1]1} + u \frac{\partial y_{l-1[1]1}}{\partial u} \right) J_2^{+0} \right. \\
&\quad \left. + \left(j_{l+1[1]1} + u \frac{\partial j_{l+1[1]1}}{\partial u} \right) Y_0^{-0} - \frac{\partial j_{l[1]2}}{\partial u} Y_1^{-1} \right] \\
\frac{\partial \psi_{l[2]11}}{\partial u} &= \frac{1}{2}\left[\frac{\partial y_{l[1]1}}{\partial u} J_0^{+1} - \left(y_{l-1[1]0} + u \frac{\partial y_{l-1[1]0}}{\partial u} \right) J_1^{+0} \right. \\
&\quad \left. + \left(j_{l+1[1]0} + u \frac{\partial j_{l+1[1]0}}{\partial u} \right) Y_1^{-0} - \frac{\partial j_{l[1]1}}{\partial u} Y_0^{-1} \right] \\
\frac{\partial \psi_{l[3]022}}{\partial u} &= \frac{c}{8}\left[\frac{\partial y_{l[1]0}}{\partial u} J_0^{+2} - 2\left(y_{l-1[1]1} + u \frac{\partial y_{l-1[1]1}}{\partial u} \right)\left(J_1^1 + \frac{1}{c} J_0^2 \right) \right. \\
&\quad + u\left(2 y_{l-2[1]0} + u \frac{\partial y_{l-2[1]0}}{\partial u} \right) J_2^0 + u\left(2 j_{l+2[1]0} + u \frac{\partial j_{l+2[1]0}}{\partial u} \right) Y_0^0 \\
&\quad \left. -2\left\{ \left(j_{l+1[1]1} + \frac{2u}{c} j_{l+2[1]0} \right) + u\left(\frac{\partial j_{l+1[1]1}}{\partial u} + \frac{u}{c} \frac{\partial j_{l+2[1]0}}{\partial u} \right) \right\} Y_1^{-1} + \frac{\partial j_{l[1]2}}{\partial u} Y_0^{-2} \right].
\end{aligned}
\tag{3.121}
$$

3.4.4 Linear collision coefficients with weak relativistic approximation

In the relativistic case, due to the relativistiv form of Maxwellian, the integration including Maxwellian can not be solved analytically. Therefore, there is no counter-part to the Eqs. (3.43)~(3.45) in the relativistic case.

In TASK/FP, the relativistic linear collision coefficients are obtained by numerical integration with a weak relativistic approximation. If either the incident or background species is weakly relativistic ($p_a \ll m_a c$, or $p_b \ll m_b c$), the kernel $\overleftrightarrow{\boldsymbol{U}}$, eq. (3.97), may be approximated by its non-relativistic form, eq. (3.31). With this approximation, the linear diffusion and friction coefficients are given with isotropic background [41]. By the use of our normalization, the coefficients are expressed as

$$\begin{aligned}
\hat{D}_{cpp} &= \frac{4\pi}{3n_b}\hat{\Gamma}\left(\frac{m_a^2 p_{tb0}^2 \gamma_a^3}{m_b^2 p_{ta0}^2 \overline{p}^3}\int_0^{p_c} \hat{f}_b \frac{\overline{p'}^4}{\gamma_b^2} d\overline{p'} + \frac{m_b p_{ta0}}{m_a p_{tb0}}\int_{p_c}^{\infty} \hat{f}_b \gamma_b \overline{p'} d\overline{p'}\right) \\
\hat{D}_{c\theta\theta} &= \frac{4\pi\hat{\Gamma}}{3n_b}\left(\frac{3\gamma_a}{2\bar{p}}\int_0^{p_c} \bar{p}'^2 \hat{f}_b d\bar{p}' - \frac{1}{2}\frac{m_a^2 p_{tb0}^2 \gamma_a^3}{m_b^2 p_{ta0}^2 \bar{p}^3}\int_0^{p_c} \bar{p}'^4 \frac{1}{\gamma_b^2}\hat{f}_b d\bar{p}' + \frac{m_b p_{ta0}}{m_a p_{tb0}}\int_{p_c}^{\infty} \bar{p}' \gamma_b \hat{f}_b d\bar{p}'\right) \\
\hat{F}_{cp} &= -\frac{4\pi}{3n_b}\hat{\Gamma}\left[3\frac{m_a}{m_b}\frac{\gamma_a^2}{\bar{p}^2}\int_0^{p_c} \bar{p}'^2 \hat{f}_b \gamma_b^{-1} d\bar{p}' - \frac{m_a}{m_b}\Theta_{b0}\frac{\gamma_a^2}{\bar{p}^2}\int_0^{p_c} \bar{p}'^4 \hat{f}_b \gamma_b^{-3} d\bar{p}'\right. \\
&\qquad \left. + 2\frac{p_{ta0}}{p_{tb0}}\frac{\bar{p}}{\gamma_a}\Theta_{a0}\int_{p_c}^{\infty} \bar{p}' \hat{f}_b d\bar{p}'\right], \qquad (3.122)
\end{aligned}$$

where p_c is given by eq. (3.72).

3.5 Quasi-linear diffusion term

The wave-particle interaction is conveniently described in terms of the quasi-linear theory [42, 43]. The quasi-linear theory assumes the amplitudes of the various modes are still small enough that the structure, frequency, and instantaneous growth rates of the modes are all adequately described by the linear approximation. Thus, even in the small amplitude limit, the quasi-linear theory allows us to understand and quantify how waves and particles exchange energy. The essence of the theory is to suppose that the 0th order distribution function f_0 does not only describe some initial state, but also describes a slowly evolving background distribution that is changing due to the effects of the unstaqble waves themselves. Moreover the assumption that f_0 is averaged spatially over many wave length is adopted. It is also assumed a continuous spectrum of waves with different k value is excited. Since the wave spectrum is sufficiently dense, coherence between modes is destroyed by phase mixing.

In this theory, the flux of plasma particles in momentum space is given by:

$$\boldsymbol{S}_{\rm ql} = -\overleftrightarrow{\boldsymbol{D}}_{\rm ql} \cdot \nabla f \qquad (3.123)$$

where $\overleftrightarrow{\boldsymbol{D}}_{\rm ql}$ is the quasi-linear diffusion tensor. Although the quasi-linear theory is not strictly applicable to a single wave, the case of sigle wave is adopted because it is the

simplest. The quasi-linear diffusion coefficient for single wave is given by [44]

$$\overleftrightarrow{\boldsymbol{D}}_{\mathrm{ql}} = \sum_n \frac{\pi}{2}\frac{q_s^2}{m_s^2}\delta(\omega - k_\parallel v_\parallel - n\Omega_s/\gamma_s)\boldsymbol{a}_n^*\boldsymbol{a}_n \tag{3.124}$$

and

$$\boldsymbol{a}_n = \Theta_n \frac{k_\parallel}{\omega}\left[\left(\frac{\omega}{k_\parallel} - v_\parallel\right)\hat{\boldsymbol{v}_\perp} + v_\perp\hat{\boldsymbol{v}_\parallel}\right] \tag{3.125}$$

$$\Theta_n = \frac{E_{w+}J_{n-1} + E_{w-}J_{n+1}}{\sqrt{2}} + \frac{v_\parallel}{v_\perp}J_n E_{w\parallel} \tag{3.126}$$

where $\Omega_s = q_s B/m_s$ is the cyclotron frequency for species s, B is the magnetic field, superscript $*$ indicates complex conjugation, J_n is the nth order Bessel function, and the argument of the Bessel functions is $k_\perp v_\perp/\Omega_s$. E_{w+} and E_{w-} are the left- and right-handed components of the wave electric field $\boldsymbol{E}_w$, that is,

$$E_{w+} = \frac{E_{wr} + iE_{w\perp}}{\sqrt{2}} \tag{3.127}$$

$$E_{w-} = \frac{E_{wr} - iE_{w\perp}}{\sqrt{2}}, \tag{3.128}$$

where E_{wr} and $E_{w\perp}$ denote the radial electric field of waves and the wave electric field perpendicular to the magnetic field.

Since the perpendicular velocity in the second term of RHS of Eq. (3.126) has a possibility to be zero, using the reccurence formula of the Bessel function

$$J_{n+1}(x) = \frac{2n}{x}J_n(x) - J_{n-1}(x), \tag{3.129}$$

we can rewrite Eq. (3.126) as

$$\Theta_n = \frac{E_{w+}J_{n-1} + E_{w-}J_{n+1}}{\sqrt{2}} + \frac{v_\parallel E_{w\parallel}k_\perp}{2n\Omega}(J_{n+1} + J_{n-1}) \tag{3.130}$$

for $n \neq 0$.

The vector $\boldsymbol{a}_n$ in Eq. (3.125) should be expressed in $(p_\parallel,\ p_\perp)$ coordinate. Sicne our coordinate system is $(p,\ \theta)$, variable transformation is required. Using the relations $\boldsymbol{v}_\parallel = \hat{\boldsymbol{p}}\cos\theta - \hat{\boldsymbol{\theta}}\sin\theta$ and $\boldsymbol{v}_\perp = \hat{\boldsymbol{p}}\sin\theta + \hat{\boldsymbol{\theta}}\cos\theta$, $\boldsymbol{a}_n$ is expressed in $(p,\ \theta)$ system:

$$\boldsymbol{a}_n = \Theta_n\left[\left\{\left(1 - \frac{k_\parallel}{\omega}v_\parallel\right)\sin\theta + \frac{k_\parallel}{\omega}v_\perp\cos\theta\right\}\hat{\boldsymbol{p}} + \left\{\left(1 - \frac{k_\parallel}{\omega}v_\parallel\right)\cos\theta - \frac{k_\parallel}{\omega}v_\perp\sin\theta\right\}\hat{\boldsymbol{\theta}}\right] \tag{3.131}$$

The delta function in Eq. (3.124) is put into Gaussian distribution for small σ

$$\delta(x) \to \frac{1}{\sqrt{2\pi}\sigma}\exp\left(-\frac{x^2}{2\sigma^2}\right) \tag{3.132}$$

in order to surpress numerical divergence due to the discretization. Using the substitution, normalized quasi-linear diffusion coefficient $\hat{\overleftrightarrow{\boldsymbol{D}}}_{ql}$ becomes

$$\hat{\overleftrightarrow{\boldsymbol{D}}}_{ql} = \frac{q_a^2}{p_{ta0}^2} \frac{\sqrt{\pi}}{2\sqrt{2}|\omega|\sigma} \exp\left(-\frac{(\omega - k_\parallel v_\parallel - n\Omega_a/\gamma_a)^2}{2\sigma^2\omega^2}\right) \boldsymbol{a}_n^* \boldsymbol{a}_n. \tag{3.133}$$

The delta function in Eq. (3.124) specifies the resonance condition. Only particles for which the Doppler-Shifted wave frequency $\omega - k_\parallel v_\parallel$ is zero ($n = 0$: the Landau damping) or a multiple of cyclotron frequency ($n \neq 0$: a cyclotron harmonic resonance) interact with the wave.

3.6 Radial transport term

TASK/FP implements the radial diffusion corresponding to the turbulence transport.

3.6.1 Pinch effect

The radial transport term contains the radial diffusion coefficient $\overleftrightarrow{\boldsymbol{D}}_\rho$ and the pinch coefficient $\boldsymbol{F}_\rho$. These coefficients should be calculated from turbulent transport models, though there exists no reliable theory based model. In the present analysis, we introduce simple models with fixed radial profiles. The pinch coefficient is chosen to sustain the initial density profile. The time evolution of momentum distribution function due to radial flux is given by [45]

$$\left(\frac{\partial f}{\partial t}\right)_\rho = -\frac{1}{\rho}\frac{\partial}{\partial \rho}\rho S_\rho \tag{3.134}$$

$$S_\rho = -D_\rho \frac{\partial f}{\partial \rho} + F_\rho f. \tag{3.135}$$

In order to keep the density defined by $n(\rho) = \int d\boldsymbol{p}\ f$, the pinch coefficient has to satisfy

$$-\int \frac{1}{\rho}\frac{\partial}{\partial \rho}\rho S_\rho d\boldsymbol{p} = 0, \tag{3.136}$$

in other words,

$$\int S_\rho d\boldsymbol{p} = 0. \tag{3.137}$$

In this case, though density is not transported, energy is able to transport, because

$$\int (\gamma - 1) S_\rho\ d\boldsymbol{p} \neq 0. \tag{3.138}$$

If F_ρ has a p dependence as same as D_ρ, F_ρ can be calculated numerically.

3.6.2 Radial dependence

We employ a simple model of radial diffusion coefficient $D_\rho(\rho)$ model. The radial profile of radial diffusion coefficient is assumed to be parabolic and stationary, namely,

$$D_\rho(\rho) = D_\rho(0) + (D_\rho(1) - D_\rho(0))\rho^2. \tag{3.139}$$

Since the radial transport in outer region is stronger than that of inner region, $D_\rho(0) < D_\rho(1)$ is usually satisfied.

3.6.3 Momentum dependence

TASK/FP implements three simple momentum dependence models. The first model has no momentum dependence. The second model is roughly proportional to the inverse of the momentum as

$$D_r \propto \frac{1}{\sqrt{1 + p^2/p_{th}^2(\rho)}} \tag{3.140}$$

where $p_{th}(\rho)$ denotes the thermal momentum at the normalized minor radius ρ (different from p_{ta0}). This model simulates the finite gyroradius effect due to turbulence with $k_\perp \rho_{th} \sim 1$, where $k_\perp$ is typical perpendicular wave number and ρ_{th} is the thermal gyroradius.

The spatial diffusion across a magnetic field can be expressed as [46]:

$$D_\perp \propto \sum_{\boldsymbol{k}} \sum_n \int_{-\infty}^{\infty} d\omega \left[|E^2(\boldsymbol{k}, \omega)| \frac{k_\perp^2}{k^2} J_n^2(\zeta_1) \delta(n\Omega + k_\parallel v_\parallel - \omega) \right] \tag{3.141}$$

where $|E^2(\boldsymbol{k}, \omega)|$ denotes the fluctuation spectrum and $J_n(\zeta)$ is the Bessel function of the nth order with the argument $\zeta = k_\perp v_\perp / \Omega = k_\perp r_g$. $\boldsymbol{k}$ and ω are the wave vector and the frequency of the fluctuation. The quasi-linear theory has shown that the radial diffusion coefficient in a magnetized plasma is proportional to $J_n^2(\zeta)$ or similar terms. Since the gyro radius r_g of energetic ion is much larger than $r_{\mathrm{g,th}}$ and $k_\perp$ spectrum of the turbulence is usually broad, $J_n^2(\zeta)$ dependence may be approximated by $1/\zeta$ by the use of the asymptotic form, $J_n(\zeta) \propto 1/\sqrt{\zeta}$. Therefore, from Eq. (3.141), we conclude that the radial diffusion scales as $1/\sqrt{p_\perp^2}$. For simplicity, $p_\perp$ in the dependence is replaced by p in our calculations.

The third model is roughly proportional to the inverse of the kinetic energy, namely square of the momentum,

$$D_r \propto \frac{1}{1 + p^2/p_{th}^2(\rho)}. \tag{3.142}$$

3.7 Source term

TASK/FP implements two kind of particle sources, neutral beam and the particles generated by fusion reaction. The Fokker-Planck equation with source term, H, is given

by:

$$\frac{\partial f}{\partial t} = -\frac{1}{p^2}\frac{\partial}{\partial p}p^2 S_p - \frac{1}{p\sin\theta}\frac{\partial}{\partial \theta}\sin\theta S_\theta - \frac{1}{\rho}\frac{\partial}{\partial \rho}\rho S_\rho + H(p,\theta,\rho). \tag{3.143}$$

3.7.1 Neutral beam injection

The nuetral beam is a source of accelerated ions and electrons which have same velocity for simplicity. In TASK/FP, the beam deposition profile is a very simple model. It is assumed to be the Gaussian distribution, namely:

$$I(\rho) \propto \frac{n_{NB}}{\sqrt{2\pi}\sigma_{NB}} \exp\left(\frac{(\rho-\rho_{NB0})^2}{2\sigma_{NB}^2}\right), \tag{3.144}$$

where n_{NB}, ρ_{NB0} and σ_{NB} denote the amount of source density $[1/\mathrm{m}^3]$, center radius of the beam deposition and the width of deposition profile. The deposition profile of neutral beam is assumed to be constant in time and the pitch angle of the beam is constant in radial direction. In momentum space, the beam source is a delta function which is non-zero at only $\bar{p} = \sqrt{2m_a E_{NB}}/p_{ta0}$ and $\theta = \theta_{NB}$, where E_{NB} and θ_{NB} denote the beam energy and the pitch angle of the beam.

3.7.2 Fusion reaction

In fusion plasma, several kinds of fusion reaction may occur, such as D-D, D-T, and T-T. These reactions have different reaction rates and temperature dependence. TASK/FP calculates the reaction rate for four kind of reaction. Since the fusion reaction rate depends on the momentum distribution functions of ions, the rate of energetic ions generation also depend on them. Under the plasma heating, therefore, the reaction rate is calculated by the numerical integration of the momentum distribution functions. The fusion reaction rate is expressed by [2, 1]:

$$\mathcal{R} = n_a n_b \langle \sigma v \rangle = \iint \sigma_T(E) v' f_a(\boldsymbol{v}_a) f(\boldsymbol{v}_b)\, d\boldsymbol{v}_a d\boldsymbol{v}_b \tag{3.145}$$

where v', E, and σ_T are relative velocity $v' = |\boldsymbol{v}_a - \boldsymbol{v}_b|$, kinetic energy of incident particle in keV, and reaction cross section in barns (1 barns $=10^{-24}\mathrm{cm}^{-2}$), respectively. The fusion cross section $\sigma_T(E)$ is approximated by fitting formula [47, 48]:

$$\sigma_T(E) = \frac{A_5 + [(A_4 - A_3 E)^2 + 1]^{-1} A_2}{E[\exp(A_1 E^{-1/2}) - 1]}. \tag{3.146}$$

The coefficients A_i are Duane coefficients given in Table 3.1

Relative velocity

In TASK/FP, the velocity and the moemntum are described in (p, θ) coordinate system. However, in order to obtain the relative velocity $v' = |\boldsymbol{v}_a - \boldsymbol{v}_b|$, the gyro phase ϕ_a and ϕ_b

	D-D	D-D	D-T	D-He^3	T-T	T-He^3
Eq.	1.1	1.2	1.3	1.4	1.5	1.6~ 1.8
A_1	46.097	47.88	45.95	89.27	38.39	123.1
A_2	372	482	50200	25900	448	11250
A_3	4.36×10^{-4}	3.08×10^{-4}	1.368×10^{-2}	3.98×10^{-3}	1.02×10^{-3}	0
A_4	1.220	1.177	1.076	1.297	2.09	0
A_5	0	0	409	647	0	0

Table 3.1: The Duane coefficients for the principle fusion reaction [1]

are required. Therefore the relative velocity between $\boldsymbol{v}_a$ and $\boldsymbol{v}_b$ have to be averaged in gyro phase. In Cartesian system, the velocity $\boldsymbol{v}_a$ and $\boldsymbol{v}_b$ can be expressed as

$$\boldsymbol{v}_a = (v_{\perp a}\cos\phi_a, v_{\perp a}\sin\phi_a, v_{\parallel a}) \tag{3.147}$$
$$\boldsymbol{v}_b = (v_{\perp b}\cos\phi_b, v_{\perp b}\sin\phi_b, v_{\parallel b}). \tag{3.148}$$

Thus the square of the relative velocity v'^2 becomes

$$\begin{aligned} v'^2 &= |\boldsymbol{v}_a - \boldsymbol{v}_b|^2 \\ &= v_{\perp a}^2 + v_{\perp b}^2 + (v_{\parallel a} - v_{\parallel b})^2 - 2v_{\perp a}v_{\perp b}\cos(\phi_a - \phi_b) \\ &= \frac{2}{\mu}E \\ &= \frac{2}{\mu}(E_0 + E_1\cos(\phi_a - \phi_b)), \end{aligned} \tag{3.149}$$

where $\mu = m_a m_b/(m_a + m_b)$ is a reduced mass, E_0 and E_1 are coefficients of the kinetic energy of relative motion, and

$$\frac{2}{\mu}E_0 = v_{\perp a}^2 + v_{\perp b}^2 + (v_{\parallel a} - v_{\parallel b})^2 \tag{3.150}$$
$$\frac{2}{\mu}E_1 = -2v_{\perp a}v_{\perp b}. \tag{3.151}$$

In Eq. (3.145), since $f_a(\boldsymbol{v}_a)$, $f_b(\boldsymbol{v}_b)$, $d\boldsymbol{v}_a$, and $d\boldsymbol{v}_b$ are independent of the gyro phase, ϕ_a and ϕ_b, $\sigma_T(E)v'$ can be averaged over the gyro phase to obtain.

$$\begin{aligned} \langle\sigma_T(E)v'\rangle_{\phi_a\phi_b} &= \left(\frac{1}{2\pi}\right)^2 \int_0^{2\pi}\int_0^{2\pi} \sigma_T(E_0 + E_1\cos(\phi_a - \phi_b)) \\ &\qquad \sqrt{\frac{2}{\mu}(E_0 + E_1\cos(\phi_a - \phi_b))}\, d\phi_a\, d\phi_b \\ &= \frac{1}{2\pi}\int_0^{2\pi} \sigma_T(E_0 + E_1\cos\psi_b)\sqrt{\frac{2}{\mu}(E_0 + E_1\cos\psi_b)}\, d\psi_b, \end{aligned} \tag{3.152}$$

where variables ϕ_a and ϕ_b are transformed into $\psi_a = \psi_a + \phi_b$ and $\psi_b = \phi_a - \phi_b$. The integration is calculated numerically.

Using Eq. (3.152), Eq. (3.145) is rewritten as

$$\mathcal{R} = \iint \langle \sigma_T(E) v' \rangle_{\phi_a \phi_b} \, f_a(\boldsymbol{v}_a) f(\boldsymbol{v}_b) \, d\boldsymbol{v}_a d\boldsymbol{v}_b. \tag{3.153}$$

3.8 Bounce averaging

In general, the magnetic field is non-uniform in magnetic confinement devices. Therefore it is necessary to include the effect of the non-uniform magnetic field into the analysis. The formulations of Fokker-Planck equation including the non-uniform magnetic field effect is given by Killeen *et al.*[49]. In this method, the gyro averaged distribution function and the Fokker-Planck equation are averaged along a poloidal circulation of guiding center. Since the poloidal circulating motion becomes bounce motion for a trapped particle, this method is called bounce averaging. According to this method, Fokker-Planck equation and its coefficients are bounce averaged in TASK/FP. The scheme of bounce averaging used in TASK/FP is explained in this section.

3.8.1 Bounce averaged Fokker-Planck equation

Now we assume that the typical time scale is longer than the bounce peroid $\tau_B = 2\pi/\omega_B$. The gyro averaged distribution function f is expanded in inverse powers of the large bounce frequency:

$$f = \mathcal{F} + \mathcal{F}_1 + \mathcal{F}_2 + \cdots \tag{3.154}$$

where $\mathcal{F}$ is bounce phase independent. Fokker-Planck equation averaged over bounce period is expressed in term of $\mathcal{F}$ as follow[49]:

$$\frac{\partial \mathcal{F}}{\partial t} = \left\langle \nabla \cdot \boldsymbol{S}_{\mathrm{c,ql}} \right\rangle_{\phi_B} + \langle \nabla \cdot \boldsymbol{S}_{\mathrm{dc}} \rangle_{\phi_B} + \left\langle \nabla_\rho \cdot \boldsymbol{S}_\rho \right\rangle_{\phi_B}. \tag{3.155}$$

where bracket, $\langle Q \rangle_{\phi_B}$, denotes the average over the bounce motion for physical quantity Q.

The bounce average is defined as:

$$\langle Q \rangle_{\phi_B} = \frac{1}{\tau_B} \int_0^{s_B} \frac{Q}{v_\parallel} ds \tag{3.156}$$

where ds is the element of the arclength along the magnetic field line associated with the guiding center motion and s_B is the arclength of guiding center orbit from minimum magnetic field point to bounce point. Here, zero banana width approximation, $\Delta_B = 0$, is applied.

Similarly, the bounce period is defined as follow:

$$\tau_B = \int_0^{s_B} \frac{ds}{|v_\parallel|}. \tag{3.157}$$

The arclength of guiding center orbit from minimum magnetic field point to maximum magnetic field point is $s_{\mathrm{mx}} = \pi q(\rho) R_0$, where $q(\rho)$ is the safty factor and R_0 is the major

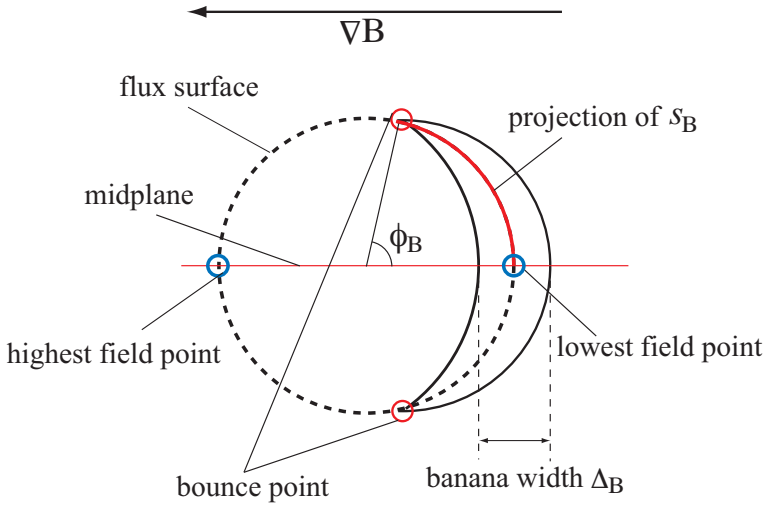

Figure 3.2: The projection of bounce motion on poloidal cross section.

radius at the magnetic axis. Because of non-uniformity of magnetic field, $v_\parallel$ depend on poloidal phase angle. Therefore it is required to express $v_\parallel$ as a function of the arclength s. Now, we define a function $\psi(s)$ as for a plasma with a circular cross section:

$$\begin{aligned}\psi(s) \equiv \frac{B(s)}{B_{\min}} &= \frac{R+r}{R+r\cos(\pi s/s_{\mathrm{mx}})} \\ &= \frac{1+\epsilon}{1+\epsilon\cos\left(\pi\frac{s}{s_{\mathrm{mx}}}\right)},\end{aligned} \tag{3.158}$$

where $\epsilon = r/R$ is the inverse aspect ratio. Since the magnetic moment $\mu = mv_\perp^2/2B(s)$ is constant, $\psi(s)$ satisfies $\sin^2\theta = \psi\sin^2\theta_0$. The pitch angle variables θ and θ_0 denote the pitch angle at s and the minimum magnetic field point, $s = 0$. Using $\psi(s)$, the definition of τ_B is rewritten as:

$$\tau_B = \int_0^{s_B} \frac{ds}{v_0\sqrt{1-\psi(s)(1-\cos^2\theta_0)}} \tag{3.159}$$

Next, the expression of the bounce averaged divergence of the flux, $\langle\nabla\cdot\boldsymbol{S}\rangle_{\phi_B}$, is considerd. Using $\psi(s)$, the derivatives in (p, θ, ρ) system are transformed into those of (p_0, θ_0, ρ_0) systems.

$$\frac{\partial}{\partial p} = \frac{\partial}{\partial p_0} \tag{3.160}$$

$$\frac{\partial}{\partial\theta} = \frac{\sin\theta\cos\theta}{\psi\sin\theta_0\cos\theta_0}\frac{\partial}{\partial\theta_0} \tag{3.161}$$

$$\frac{\partial}{\partial\rho} = \frac{\partial}{\partial\rho_0} \tag{3.162}$$

Therefore $\langle \nabla \cdot \boldsymbol{S} \rangle_{\phi_B}$ is expressed as

$$\begin{aligned}\langle \nabla \cdot \boldsymbol{S} \rangle_{\phi_B} &\equiv \frac{1}{\tau_B} \int_0^{s_B} \frac{ds}{|v_\parallel|} \left[-\frac{1}{p^2} \frac{\partial}{\partial p} p^2 S_p - \frac{1}{p \sin\theta} \frac{\partial}{\partial \theta} \sin\theta S_\theta - \frac{1}{\rho} \frac{\partial}{\partial \rho} \rho S_\rho \right] \\ &= \frac{1}{\tau_B} \int_0^{s_B} \frac{ds}{v_0 |\cos\theta|} \left[-\frac{1}{p_0^2} \frac{\partial}{\partial p_0} p_0^2 S_p - \frac{1}{p_0} \frac{\cos\theta}{\psi \sin\theta_0 \cos\theta_0} \frac{\partial}{\partial \theta_0} \sin\theta S_\theta - \frac{1}{\rho_0} \frac{\partial}{\partial \rho_0} \rho_0 S_\rho \right]\end{aligned} \tag{3.163}$$

Now we introduce $\lambda = v_0 |\cos\theta_0| \tau_B$ and rewrite Eq. (3.163) as

$$\begin{aligned}\langle \nabla \cdot \boldsymbol{S} \rangle = \frac{1}{\lambda} \Bigg[&\frac{1}{p_0^2} \frac{\partial}{\partial p_0} p_0^2 \lambda \left\langle S_p \right\rangle_{\phi_B} \\ &+ \frac{1}{p_0 \sin\theta_0} \frac{\partial}{\partial \theta_0} \sin\theta_0 \lambda \left\langle \frac{\cos\theta \sin\theta}{\psi \cos\theta_0 \sin\theta_0} S_\theta \right\rangle_{\phi_B} + \frac{q(\rho) R_0}{\rho_0} \frac{\partial}{\partial \rho_0} \rho_0 \frac{\lambda}{q(\rho_0) R_0} \left\langle S_\rho \right\rangle_{\phi_B} \Bigg].\end{aligned} \tag{3.164}$$

The detailed derivation of this equation is introduced in Appendix C. Since the bounce average parameter λ has a dimension of the length, we normalize the bounce average parameter by $q(\rho_0)R_0$ as $\lambda = v_0 |\cos\theta_0| \tau_B / (q(\rho_0) R_0)$. Because of the independence of the normalized factor from the variables p_0 and θ_0, by using this normalization, Eq. (3.164) can be rewritten as:

$$\begin{aligned}\lambda \langle \nabla \cdot \boldsymbol{S} \rangle = &\frac{1}{p_0^2} \frac{\partial}{\partial p_0} p_0^2 \lambda \left\langle S_p \right\rangle_{\phi_B} \\ &+ \frac{1}{p_0 \sin\theta_0} \frac{\partial}{\partial \theta_0} \sin\theta_0 \lambda \left\langle \frac{\cos\theta \sin\theta}{\psi \cos\theta_0 \sin\theta_0} S_\theta \right\rangle_{\phi_B} + \frac{1}{\rho_0} \frac{\partial}{\partial \rho_0} \rho_0 \lambda \left\langle S_\rho \right\rangle_{\phi_B}\end{aligned} \tag{3.165}$$

Then the bounce averaged Fokker-Planck equation is given by:

$$\begin{aligned}\frac{\partial \lambda \mathcal{F}}{\partial t} = &-\frac{1}{p_0^2} \frac{\partial}{\partial p_0} p_0^2 \lambda \left\langle S_p \right\rangle_{\phi_B} \\ &- \frac{1}{p_0 \sin\theta_0} \frac{\partial}{\partial \theta_0} \sin\theta_0 \lambda \left\langle \frac{\cos\theta \sin\theta}{\psi \cos\theta_0 \sin\theta_0} S_\theta \right\rangle_{\phi_B} - \frac{1}{\rho_0} \frac{\partial}{\partial \rho_0} \rho_0 \lambda \left\langle S_\rho \right\rangle_{\phi_B}.\end{aligned} \tag{3.166}$$

where each components of the bounce averaged flux $\lambda \langle \boldsymbol{S} \rangle_{\phi_B}$ are expressed as

$$\lambda \left\langle S_p \right\rangle_{\phi_B} = -D_{pp0} \frac{\partial \mathcal{F}}{\partial p_0} - D_{p\theta 0} \frac{1}{p_0} \frac{\partial \mathcal{F}}{\partial \theta_0} + F_{p0} \mathcal{F} = S_{p0} \tag{3.167}$$

$$\lambda \left\langle \frac{\cos\theta \sin\theta}{\psi \cos\theta_0 \sin\theta_0} S_\theta \right\rangle_{\phi_B} = -D_{\theta p 0} \frac{\partial \mathcal{F}}{\partial p_0} - D_{\theta\theta 0} \frac{1}{p_0} \frac{\partial \mathcal{F}}{\partial \theta_0} + F_{\theta 0} \mathcal{F} = S_{\theta 0} \tag{3.168}$$

$$\lambda \left\langle S_\rho \right\rangle_{\phi_B} = -D_{\rho 0} \frac{\partial \mathcal{F}}{\partial \rho} + F_{\rho 0} \mathcal{F} = S_{\rho 0}. \tag{3.169}$$

The new coefficients $\overleftrightarrow{\boldsymbol{D}}_0$ and $\boldsymbol{F}_0$ are composed of the following coefficients.

$$
\begin{aligned}
D_{pp0} &= \lambda \left\langle D_{pp} \right\rangle_{\phi_B} \\
D_{p\theta 0} &= \lambda \left\langle \frac{\cos\theta}{\sqrt{\psi}\cos\theta_0} D_{p\theta} \right\rangle_{\phi_B} \\
D_{\theta p 0} &= \lambda \left\langle \frac{\cos\theta \sin\theta}{\psi \cos\theta_0 \sin\theta_0} D_{\theta p} \right\rangle_{\phi_B} \\
D_{\theta\theta 0} &= \lambda \left\langle \frac{\cos^2\theta}{\psi^{3/2}\cos^2\theta_0} \frac{\sin\theta}{\sin\theta_0} D_{\theta\theta} \right\rangle_{\phi_B} \\
F_{p0} &= \lambda \left\langle F_p \right\rangle_{\phi_B} \\
F_{\theta 0} &= \lambda \left\langle \frac{\cos\theta}{\psi\cos\theta_0} \frac{\sin\theta}{\sin\theta_0} F_\theta \right\rangle_{\phi_B} \\
D_{\rho 0} &= \lambda \left\langle D_\rho \right\rangle_{\phi_B} \\
F_{\rho 0} &= \lambda \left\langle F_\rho \right\rangle_{\phi_B}
\end{aligned}
\tag{3.170}
$$

Similarly, the boucen averaged Fokker-Planck equation with source term is given by:

$$
\begin{aligned}
\frac{\partial \lambda \mathcal{F}}{\partial t} = &-\frac{1}{p_0^2}\frac{\partial}{\partial p_0} p_0^2 \lambda \left\langle S_p \right\rangle_{\phi_B} \\
&-\frac{1}{p_0 \sin\theta_0}\frac{\partial}{\partial\theta_0}\sin\theta_0 \lambda \left\langle \frac{\cos\theta\sin\theta}{\psi\cos\theta_0\sin\theta_0} S_\theta \right\rangle_{\phi_B} - \frac{1}{\rho_0}\frac{\partial}{\partial\rho_0}\rho_0 \lambda \left\langle S_\rho \right\rangle_{\phi_B} + \lambda \langle H \rangle .
\end{aligned}
\tag{3.171}
$$

In the following, the distribution function with 0-th order of bounce phase $\mathcal{F}$ is represented by merely f for simplicity

3.8.2 Bounce averaging parameters

Now we examine the boundary condition $\theta_0 = \theta_B$ which divides the momentum space into trapped and passing regions. From the conservation of magnetic moment, the poloidal angle of bounce point ϕ_B is obtained as

$$
\cos\phi_B = 1 - \frac{1+\epsilon}{\epsilon}\cos^2\theta_0. \tag{3.172}
$$

When $\theta_0 = \theta_B$, the particle bounce at the highest magnetic field point, $\phi_B = \pi$. Thus the boundary pitch angle θ_B is given by

$$
\cos\theta_B = \sqrt{\frac{2\epsilon}{1+\epsilon}}. \tag{3.173}
$$

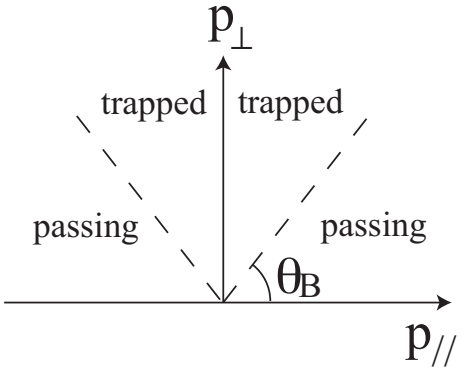

Figure 3.3: Trapped and passing regions at minimum magnetic field point.

The bounce period τ_B is given by Eq. (3.159). The integrating variable transformation, $ds = s_{\rm mx} d\phi/\pi$, makes Eq. (3.159)

$$\tau_B = \frac{s_{\rm mx}}{v_0 \pi} \int_0^{\phi_B} d\phi \sqrt{\frac{1+\epsilon\cos\phi}{1+\epsilon\cos\phi-(1+\epsilon)\sin^2\theta_0}}. \tag{3.174}$$

Similarly, the bounce averaging parameter λ is given by

$$\lambda = \frac{|\cos\theta_0|}{\pi} \int_0^{\phi_B} d\phi \sqrt{\frac{1+\epsilon\cos\phi}{1+\epsilon\cos\phi-(1+\epsilon)\sin^2\theta_0}}. \tag{3.175}$$

3.8.3 Bounce averaged dc electric field term

The bounce averaging of the dc electric field term requires the following steps. The parallel electric field $E_{\|0}$ at minimum magnetic field point and $E_\|$ at any arclength s satisfy the following relation

$$2\pi(R+r)E_{\|0} = 2\pi(R+r\cos\phi)E_\|$$

namely,

$$E_\| = \psi(s) E_{\|0}. \tag{3.176}$$

The p and θ components of Eqs. (3.29) are bounce averaged as

$$\begin{aligned}\lambda\left\langle \hat{F}_p \right\rangle &= \frac{\lambda}{\tau_B}\int_0^{s_B} \frac{ds}{v_0|\cos\theta|}\hat{F}_p \\ &= \frac{1}{\pi}\frac{q_a}{p_{ta0}} E_{\|0}|\cos\theta_0| \int_0^{\phi_B} d\phi\, \psi(s)\frac{\cos\theta}{|\cos\theta|},\end{aligned} \tag{3.177}$$

$$\begin{aligned}\lambda\left\langle \frac{\cos\theta}{\psi\cos\theta_0}\frac{\sin\theta}{\sin\theta_0}F_{e\theta}\right\rangle &= \frac{\lambda}{\tau_B}\int_0^{s_B}\frac{ds}{v_0|\cos\theta|}\frac{\cos\theta}{\psi\cos\theta_0}\frac{\sin\theta}{\sin\theta_0}F_{e\theta} \\ &= -\frac{1}{\pi}\frac{q_e}{p_{ta0}}E_{\|0}\sin\theta_0\int_0^{\phi_B}\psi(s)d\phi.\end{aligned} \tag{3.178}$$

for passing particles. On the other hand, DC term for trapped particles becomes zero. Since trapped particles have back-and-forth motion along the magnetic field line, the average for trapped particles becomes zero.

3.9 Evaluations of physical quantities

3.9.1 Variation of kinetic energy

In this section, the variation of the kinetic energy due to each term is considerd. In the non-relativistic limit, the total kinetic energy for species "a", W_a, is given by

$$\begin{aligned} W_a &= \int \frac{1}{2} m_a v^2 f_a \, d^3\boldsymbol{v} \\ &= \frac{p_{ta0}^2}{2m_a} \int \bar{p^2} \hat{f}_a \bar{p}^2 \sin\theta \, d\bar{p} \, d\theta. \end{aligned} \tag{3.179}$$

Thus the variation of the kinetic energy becomes

$$\frac{\partial W_a}{\partial t} = \frac{p_{ta0}^2}{2m_a} \int \bar{p^2} \frac{\partial \hat{f}_a}{\partial t} \bar{p}^2 \sin\theta \, d\bar{p} \, d\theta. \tag{3.180}$$

At first, the variation without radial diffusion is discussed. In this case, the variation of the momentum distributio function is

$$\frac{\partial \hat{f}_a}{\partial t} = -\frac{1}{\bar{p}^2} \frac{\partial}{\partial \bar{p}} \bar{p}^2 \hat{S}_p - \frac{1}{\bar{p} \sin\theta} \frac{\partial}{\partial \theta} \sin\theta \hat{S}_\theta. \tag{3.181}$$

Substituting Eq. (3.181) into Eq. (3.180),

$$\frac{\partial W_a}{\partial t} = -\frac{p_{ta0}^2}{2m_a} \int \left(\frac{\partial}{\partial \bar{p}} \bar{p}^2 \hat{S}_p + \frac{\bar{p}}{\sin\theta} \frac{\partial}{\partial \theta} \sin\theta \hat{S}_\theta \right) \bar{p}^2 \sin\theta \;\; d\bar{p} \, d\theta \tag{3.182}$$

is given. Using integration by parts for $d\bar{p}$, Eq. (3.182) becomes

$$\frac{\partial W_a}{\partial t} = \frac{p_{ta0}^2}{m_a} \int \bar{p}^3 \hat{S}_p \sin\theta \, d\bar{p} \, d\theta. \tag{3.183}$$

In the relativistic case, since the total kinetic energy is given by:

$$W_a = mc^2 \int (\gamma_a - 1) \hat{f}_a \, \bar{p}^2 \sin\theta \, d\bar{p} \, d\theta, \tag{3.184}$$

the expression of the variation of the kinetic energy is expressed as

$$\frac{\partial W_a}{\partial t} = \frac{p_{ta0}^2}{m_a} \int \frac{\bar{p}^3}{\gamma} \hat{S}_p \sin\theta \, d\bar{p} \, d\theta. \tag{3.185}$$

Using these expressions, the kinetic energy variation can be evaluated.

Next, the energy variation due to radial diffusion is discussed. The variation of the stored energy in the region $r_1 < \rho < r_2$ is given by

$$\Delta E = 4\pi^2 R \int_{r_1}^{r_2} \rho \, d\rho \left[mc^2 \int (\gamma - 1) \frac{\partial \hat{f}_a}{\partial t} \bar{p}^2 \sin\theta \, d\bar{p} d\theta \right] \tag{3.186}$$

Since the variation of the momentum distribution function due to radial transport is

$$\frac{\partial \hat{f}_a}{\partial t} = -\frac{1}{\rho} \frac{\partial}{\partial \rho} \rho \hat{S}_\rho, \tag{3.187}$$

the amount of energy transported radially is

$$\Delta E = -4\pi^2 R mc^2 \int (\gamma - 1) \bar{p}^2 \sin\theta \left[\rho \hat{S}_\rho \right]_{r_1}^{r_2} \, d\bar{p} d\theta \tag{3.188}$$

3.9.2 Temperatures

The definition of temperature was discussed in Sec. 3.1.3. However, the relation between kinetic energy density and temperature is valid only for Maxwellian distribution function. Since heated plasma has non-Maxwellian distribution function, in general temperature like parameter should be introduced.

The most simple one is the temperature which is adopted the relation between kinetic energy density and temperature of Maxwellian distribution function, namely:

$$W_a = mc^2 \left(4\Theta_a + \frac{K_1(\Theta_a^{-1})}{K_2(\Theta_a^{-1})} - 1 \right) n_a(\rho). \tag{3.15}$$

Eq. (3.15) is the relation between relativistic kinetic energy and temperature. Form now on, we call this *averaged energy temperature*. Since the averaged energy temperature is strongly affected by fewer fast ion tail, it tends to be overestimated.

The other temperature like parameter evaluates temperature averaged over the particles thermal momentum. By considering around thermal momentum, the effect of less fast ions is supressed; so we call this parameter as *bulk temperature*. For Maxwellian distribution function, temperature satisfies the following relation in whole momentum space:

$$T_s = -\frac{p_s f_s}{\gamma_s} \left(\frac{\partial f_s}{\partial p} \right)^{-1} \tag{3.189}$$

If the number of fast ions is small, most of ions with the order of thermal momentum (bulk ion) still satisfy Eq. (3.189). Therefore, we evaluate the bulk temperature T_{bulk} as the average of Eq. (3.189) around the normalized thermal momentum ($0 < \bar{p} <\sim 4$).

3.10 Numeical schemes

3.10.1 Boundary condition

In TASK/FP, the computational domain for the Fokker-Planck equation is taken as:

$$\begin{aligned} 0 < p < p_{\max} \\ 0 < \theta < \pi \\ 0 < \rho < 1. \end{aligned}$$

Therefore, the boundary of computational domain exists at $p = 0$, $p = p_{\max}$, $\theta = 0$, $\theta = \pi$, $\rho = 0$, and $\rho = 1$. The boundaries at $p = 0$, $\theta = 0$, and $\theta = \pi$ are treated with the boundary conditions:

$$\begin{aligned} f_s(-p, \theta) &= f_s(p, \pi - \theta) \\ f_s(p, -\theta) &= f_s(p, \theta) \\ f_s(p, \pi + \theta) &= f_s(p, \pi - \theta). \end{aligned}$$

Now the normal vector $\hat{\boldsymbol{n}}$ perpendicular to the $p = p_{\max}$ boundary is introduced. The boundary condition at $p = p_{\max}$ is described as:

$$\boldsymbol{S} \cdot \hat{\boldsymbol{n}} = 0 \qquad \text{at} \quad p = p_{\max}, \tag{3.190}$$

namely:

$$D_{pp} = D_{p\theta} = F_p = 0 \qquad \text{at} \quad p = p_{\max}. \tag{3.191}$$

This means that the plasma can not enter or leave the integration domain. Thus the number of plasma particles is conserved with this boundary condition.

If an electric field is present, then in the real problem some electrons will run away. Now I wish to impose boundary conditions which allow this to happen. The p component of the dc acceleration term is $F_p \propto (q_s E/m_s)\cos\theta$. Since run away will occur in the case of $F_p > 0$, the boundary condition on $p = p_{\max}$, Eq. (3.191), can be rewritten as:

$$\begin{aligned} D_{pp} = D_{p\theta} = F_p = 0 \qquad &\text{for} \quad F_p < 0 \\ D_{pp} = D_{p\theta} = 0 \qquad &\text{for} \quad F_p > 0. \end{aligned} \tag{3.192}$$

3.10.2 Spatial differencing

In order to solve the Fokker-Planck equation, the differential equation should be converted to algebraic equation by using the finite difference method. In this method, f is represented by its values on a finite set of points and differentials are represented by the differences between neighboring values.

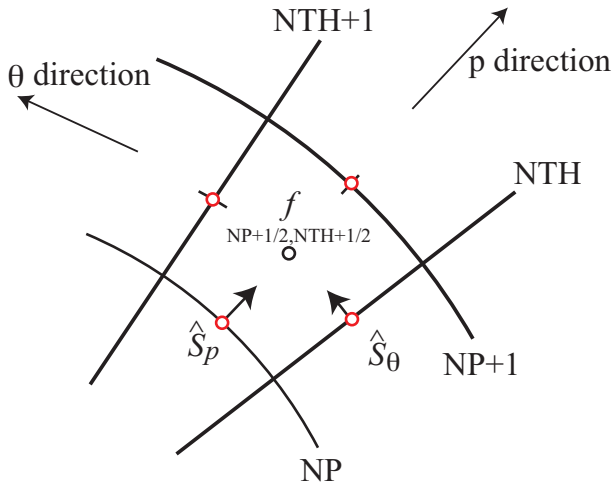

Figure 3.4: The numerical grid showing where the momentum distribution function and the fluxes are defined in momentum space.

First, the numerical grid points for momentum space are discussed. A set of numerical grid points is established by dividing $\bar{p}$ and θ into NPMAX and NTHMAX equal pieces. That is:

$$\Delta\bar{p} = \bar{p}_{\max}/\text{NPMAX}$$
$$\Delta\theta = \pi/\text{NTHMAX}.$$

Each grid point is represented by two variables

$$\bar{p}_{\text{NP}} = \text{NP} \times \Delta\bar{p}$$
$$\theta_{\text{NTH}} = \text{NTH} \times \Delta\theta$$

These grid points make cells. The momentum distribution function is represented by its value at the center of each cell as is shown in Fig. 3.4.

$$\hat{f}_{\text{NP+1/2,NTH+1/2}} = f(\bar{p}_{\text{NP+1/2}}, \theta_{\text{NTH+1/2}})$$
$$\text{for} \quad 0 \le \text{NP} < \text{NPMAX}, \quad \text{and} \quad 0 \le \text{NTH} < \text{NTHMAX} \tag{3.193}$$

On the other hands, the fluxes are represented by the value at the points on the cell boundary. The flux $\hat{S}_p$ is defined by the value at the middle of θ grid point on a $\bar{p}$ grid line. And the flux $\hat{S}_\theta$ is defined by the value at the middle of $\bar{p}$ grid point on a θ grid line.

Similarly, numerical grid points for radial direction is also established by dividing ρ into NRMAX equal pieces,

$$\Delta\rho = \rho_{\max}/\text{NRMAX}.$$

And then, each grid point is

$$\rho_{\text{NR}} = \text{NR} \times \Delta\rho$$

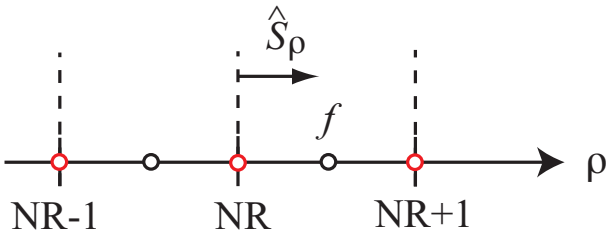

Figure 3.5: The numerical grid showing where the momentum distribution function and the fluxes are defined in radial direction.

Similar to the momentum space, the momentum distribution function is represented by its value at the center of each radial grid points as is shown in Fig. 3.5. The flux of radial transport is calculated on the radial grid point.

The evaluation of $\hat{f}$ on grid lines, such as red circles in Fig. 3.4 and 3.5, uses a method proposed by Chang and Cooper [50] extended to two dimension by Karney [20]. It is found that the simple average of two points

$$\hat{f}_{\mathrm{NP,NTH+1/2}} = \frac{1}{2}\left(\hat{f}_{\mathrm{NP-1/2,NTH+1/2}} + \hat{f}_{\mathrm{NP+1/2,NTH+1/2}}\right)$$
$$\hat{f}_{\mathrm{NP+1/2,NTH}} = \frac{1}{2}\left(\hat{f}_{\mathrm{NP+1/2,NTH-1/2}} + \hat{f}_{\mathrm{NP+1/2,NTH+1/2}}\right)$$

gives poor result due to the flow in momentum space. Chang and Cooper replace these with

$$\begin{aligned}\hat{f}_{\mathrm{NP,NTH+1/2}} &= (1-\delta_{\mathrm{NP,NTH+1/2}})\hat{f}_{\mathrm{NP+1/2,NTH+1/2}} + \delta_{\mathrm{NP,NTH+1/2}}\hat{f}_{\mathrm{NP-1/2,NTH+1/2}} \\ \hat{f}_{\mathrm{NP+1/2,NTH}} &= (1-\delta_{\mathrm{NP+1/2,NTH}})\hat{f}_{\mathrm{NP+1/2,NTH+1/2}} + \delta_{\mathrm{NP+1/2,NTH}}\hat{f}_{\mathrm{NP+1/2,NTH-1/2}},\end{aligned} \tag{3.194}$$

where the coefficients $\delta_{i,j}$ are given by:

$$\delta_{\mathrm{NP,NTH+1/2}} = g\left(-\Delta\theta\frac{\hat{F}_{\theta:\mathrm{NP,NTH+1/2}}}{\hat{D}_{\theta\theta:\mathrm{NP,NTH+1/2}}}\right) \tag{3.195}$$

$$\delta_{\mathrm{NP+1/2,NTH}} = g\left(-\Delta\bar{p}\frac{\hat{F}_{p:\mathrm{NP+1/2,NTH}}}{\hat{D}_{pp:\mathrm{NP+1/2,NTH}}}\right), \tag{3.196}$$

and

$$g(w) = \frac{1}{w} - \frac{1}{\exp(w)-1}. \tag{3.197}$$

The function $g(w)$ has the properties

$$\begin{aligned} &g(w) = 1 - g(-w) \\ &g(w) = \frac{1}{2} - \frac{w}{12} + \frac{w^3}{120} \quad \text{for } w \ll 1 \\ &g(-\infty) = 1 \\ &g(0) = 1/2 \\ &g(\infty) = 1. \end{aligned}$$

The role of $\delta_{i,j}$ is to weight the averaging. This weighting is necessary because $\hat{f}$ is a strongly varying function of $\bar{p}$. For example, non-relativistic Maxwellian varies with $\exp(-\bar{p}^2)$.

Similarly, the momentum distribution function on a radial grid point is estimated as

$$\hat{f}_{\mathrm{NR}} = (1 - \delta_{\mathrm{NR}})\hat{f}_{\mathrm{NR}+1/2} + \delta_{\mathrm{NR}}\hat{f}_{\mathrm{NR}-1/2}, \tag{3.198}$$

where the δ_{NR} is given by:

$$\delta_{\mathrm{NR}} = g\left(-\Delta\rho\frac{\hat{F}_{\rho:\mathrm{NR}}}{\hat{D}_{\rho:\mathrm{NR}}}\right). \tag{3.199}$$

The dependence of momentum distribution function on ρ is not so strong as $\bar{p}$ dependence.

3.10.3 Time advancing

In this section, the method for time advancing is discussed. The simplest way of time advancing is the explicit scheme:

$$\frac{\boldsymbol{f}_s^{t+1} - \boldsymbol{f}_s^t}{\Delta t} = \overset{\leftrightarrow}{\boldsymbol{A}}_s^t \cdot \boldsymbol{f}_s^t + \boldsymbol{H}_s, \tag{3.200}$$

where subscript t, tensor $\overset{\leftrightarrow}{\boldsymbol{A}}$, an vector $\boldsymbol{H}$ denote the step number, the coefficient matrix, and source term vector, respectively. In this scheme, Δt must be chosen to be very small for numerical stability. Too small time step is not applicable for transport code.

TASK/FP adopts a full implicit method for time advancing in stead of the explicit method. The discretized equation to be solved is

$$\frac{\boldsymbol{f}_s^{t+1} - \boldsymbol{f}_s^t}{\Delta t} = \overset{\leftrightarrow}{\boldsymbol{A}}_s^{t+1} \cdot \boldsymbol{f}_s^{t+1} + \boldsymbol{H}_s. \tag{3.201}$$

Eq. (3.201) can be solved for $\boldsymbol{f}_s^{t+1}$:

$$\boldsymbol{f}_s^{t+1} = \left(\overset{\leftrightarrow}{\boldsymbol{I}} - \overset{\leftrightarrow}{\boldsymbol{A}}_s^{t+1}\Delta t\right)^{-1} \cdot \left(\boldsymbol{f}_s^t + \boldsymbol{H}_s\Delta t\right). \tag{3.202}$$

Since $\overset{\leftrightarrow}{\boldsymbol{A}}_s^{t+1}$ in RHS of Eq. (3.202) depends on $\boldsymbol{f}_s^{t+1}$, it is necessary to use $\overset{\leftrightarrow}{\boldsymbol{A}}_s^t$ instead of $\overset{\leftrightarrow}{\boldsymbol{A}}_s^{t+1}$ at the first step. Then using obtained temporal $\boldsymbol{f}_s^{t+1}$, tensor $\overset{\leftrightarrow}{\boldsymbol{A}}_s^{t+1}$ is calculated. Iterating the sequence until the calculation converges, we obtain the solution $\boldsymbol{f}_s^{t+1}$. The convergence criterion is expressed as:

$$\frac{\left|f_s^{t,n+1} - f_s^{t,n}\right|}{f_s^t} \leq \varepsilon, \tag{3.203}$$

where superscript n denotes the iteration number.

The formulation of the matrix $\overset{\leftrightarrow}{\boldsymbol{A}}$ is shown in Appendix B.

3.10.4 Parallel computing

The size of the momentum distribution function vector in Eq. (3.201) is NPMAX $\times$ NTHMAX $\times$ NRMAX, and that of the coefficient matrix is (NPMAX $\times$ NTHMAX $\times$ NRMAX)^2 though it is a band matrix which has finite width of (NPMAX$\times$NTHMAX). Since the typical amount of the grid number is around 100, the coefficient matrix becomes very huge. Therefore, it is necessary to solve the matrix equation for large-scale asymmetric matrix as fast as possible. For this purpose, TASK/FP is parallelized with the parallel computing library, PETSc (The Portable Extensible Toolkit for Scientific Computation) [51]. PETSc is a program library developed by S. Balay, *et al.* and is used widely for numerical analysis in the field of aerodynamics and acoustics. The primary features of PETSc are listed below.

- Open-sourced code
- Portable to UNIX and Windows
- Intensive error checking
- Three program languages, C, C++, and FORTRAN, are supported.
- Both real and complex calculation is enable.
- Several preconditionerare implemented.
- Several iteration method are implemented. Here we use the defoult one, GMRES (Generalized minimal residual).

In TASK/FP, the calculation is split into processes, the number of which is a divisor of the number of radial grid points. The reduction of computation time through parallel processing is shown in the following. With a cluster computer with 128 cores on 16 nodes, the test calculation is done for combinations of different number of nodes and cores. The test calculation describes temperature relaxation among electron and ions and 64 radial mesh are used without radial diffusion.

The results of test calculation is listed in Table 3.2. And Fig. 3.6 shows that calculation time (user time and system time) [2] vs. the number of radial grid points per node for different the number of cores for 64, 32, and 16 cores, respectively. These values are the average of five trials. From Fig. 3.6, the more cores are used, the less calculation time becomes. Moreover, it is found that cpu time is little affected by the number of grid points per node. On the contrary, system time is strongly affected by the number of grid points per node. Thus, cpu time depends strongly on the number of cores used. On the other hand, system time depends on the calculation size per node.

[2] The total time (real CPU time or elapsed time) is the combination of the amount of time the CPU spends performing some action for a program and the amount of time the CPU spends performing system calls for the kernel on the program's behalf. When a program loops through an array, it is accumulating user CPU time. Conversely, when a program executes a system call, it is accumulating system CPU time.

number of core	64		32			16		
grid/core	1		2			3		
number of node	16	8	16	8	4	16	8	4
grid/node	4	8	4	8	16	4	8	16
core/node	4	8	2	4	8	1	2	4
User time [s]	119	113	319	316	380	1037	935	1150
Sys. time [s]	141	198	459	583	842	1130	1677	2600
S/(U+S)	0.54	0.64	0.59	0.65	0.69	0.52	0.64	0.69

Table 3.2: The calculation times for the test calculation are listed.

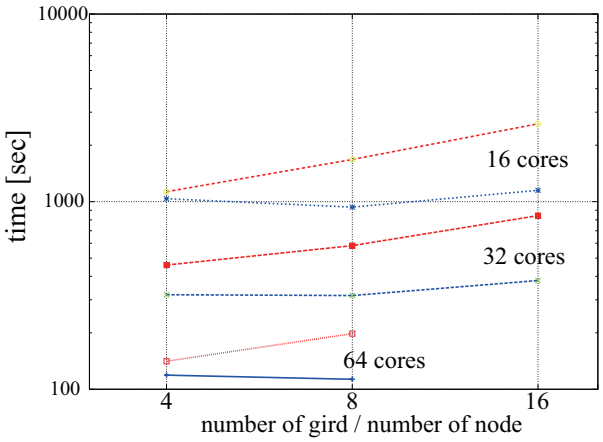

Figure 3.6: The user time (blue lines) and the system times (red lines) for different the number of cores are shown. Horizontal axis denotes the number of grid points divided by the number of nodes and vertical axis denotes the calculation time.

Chapter 4

Verification of the code

In this chapter, the verification for each term of TASK/FP is shown. The properties of Coulomb collision term, dc electric field term, quasi-linear term, and source term are verified. The effect of bounce average is also confirmed.

4.1 Reaction rate

4.1.1 Reaction rate for Maxwellian distribution function

Here, our calculation results of reaction rate is compared with the literature values [1]. Fig. 4.1 shows the $\langle \sigma v \rangle$ vs. temperature for D-D, D-T, and T-T reactions. In Fig. 4.1, lines indicate our calculation, and black points indicate the literature value. In this calculation, deuteron and triton are set to have same temperature ($T_D = T_T$) and their momentum distribution functions are set to be Maxwellian. The value of D-D reaction is sum of two reactions, Eq. (1.1) and (1.2). From Fig. 4.1, it is found that our calculations have good agreements with literature values for each reaction.

4.1.2 Reaction rate for non-Maxwellian distribution function

Since NBI and RF waves deform the momentum distribution function of incident nuclei, the fusion reaction rate should include the effect of non-Maxwellian distribution function. Here, the influence of non-Maxwellian distribution function on fusion reaction rate is discussed. In order to deform the momentum distribution function, ICRF wave and 1 MeV D-NBI are applied for heat source in these test calculations.

Figs. 4.2 show the examples of the contour of the deformed momentum distribution function for deuteron (a) and triton (b) at 50 msec after onset of heatings in 2D momentum space. The x and y axes denote normalized parallel and perpendicular momentum. In a set of test calculations, both heating powers are set to be close, and they are around $16\mathrm{MW/m^3}$. The deuteron neutral beam is injected with 1 MeV energy and pitch angle $\theta = \pi/9$. In Fig. 4.2-(a), its distribution spreads from the NBI source. Fig. 4.2-(b) shows the momentum distribution function of triton. Since tritons are accelerated by ion cyclotron resonance, their perpendicular momentum increase compared to parallel moemntum. Moreover the fast triton generated by D-D reaction is also displayed in

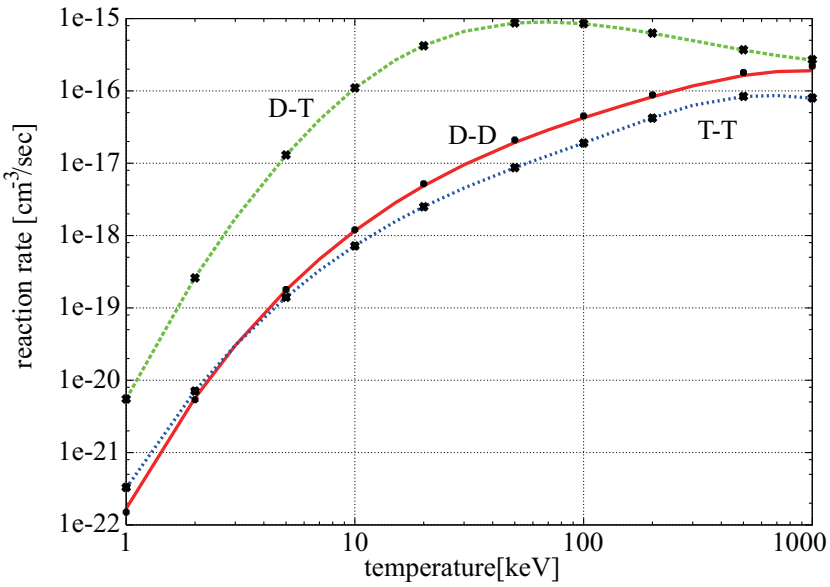

Figure 4.1: The comparison of $\langle \sigma v \rangle$ between our calculation (lines) and the literature value (black points) is shown.

Fig. 4.2-(b) at 1.05MeV ($\bar{p} \sim 14$). The fast tritons generated by D-D reactions are distributed isotropically.

The influence of non-Maxwellian distribution on the fusion reaction rate is shown in Fig. 4.3. The lines indicate $\langle \sigma v \rangle$ calculated for Maxwellian, and the points indicate that for non-Maxwellian distribution function. Since the temperatures of deuteron and triton become different due to heating, the average of two bulk temperature, deuteron and triton, is applied for the temperatures of heated deuteron and triton. The bulk temperature is previously defined at Sec. 3.9.2. From Fig. 4.3, it is found that the influence of non-Maxwellian on the fusion reaction rate is strong at low temperature region rather than that of figh temperature region for each reactions. This is beause the particles which fuse thermally are very few at low temperature. On the other hand, the number of fusing fast particles are little affected by temperature. Especially, the amount of fast deuteron injected by NBI is constant for each plot point.

The result shows that the fusion reaction rate should be considered with the effect of non-Maxwellian distribution function, especially the effect of fast ions, in the temperature range of less than 10 keV for D–T reaction and less than the 50 keV for D–D and T–T reactions. Since the typical plasma temperature in start up phase of ITER plasma is less than 10 keV, kinetic treatment of fusion reaction rate is required at least in the analysis of plasma heating in the start up phase.

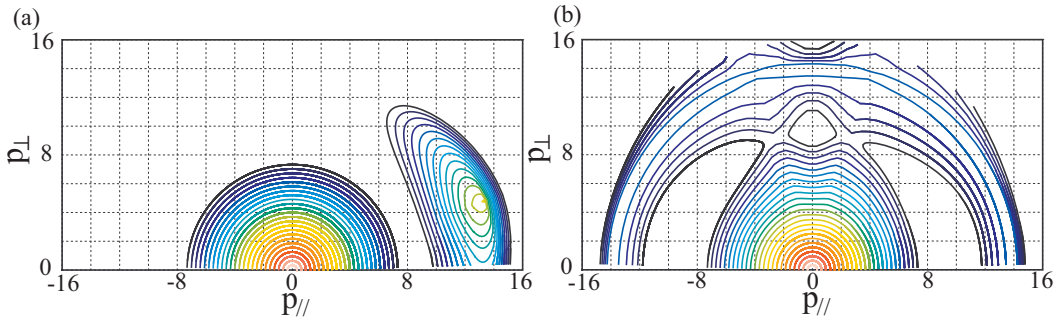

Figure 4.2: The examples of non-Maxwellian distribution function in moemntum space are shown. (a) deuteron with NBI source, (b) triton accelerated by ICRF with fusion generated source. Both of initial temperatures are set as 10 keV. In this case, $\bar{p} = 1$ corresponds to 5keV.

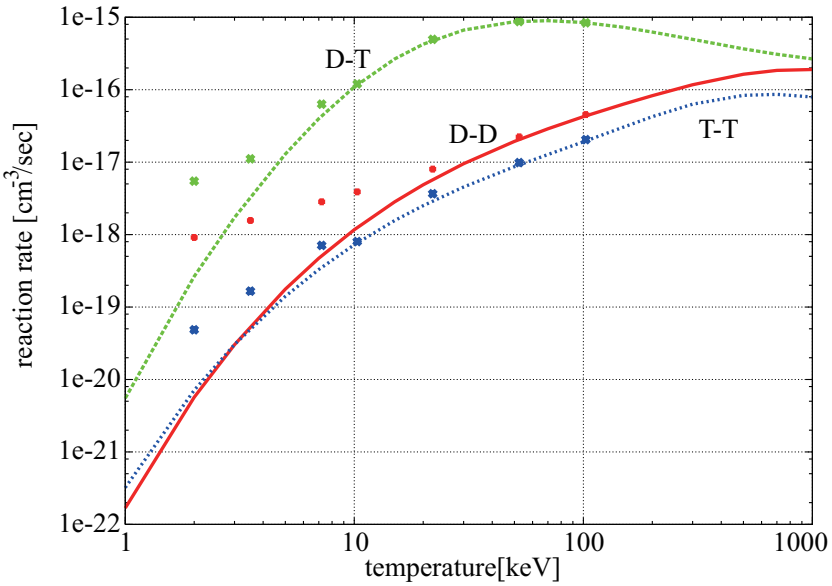

Figure 4.3: The comparison of $\langle \sigma v \rangle$ between calculation for Maxwellian (lines) and non-Maxwellian (points) is shown.

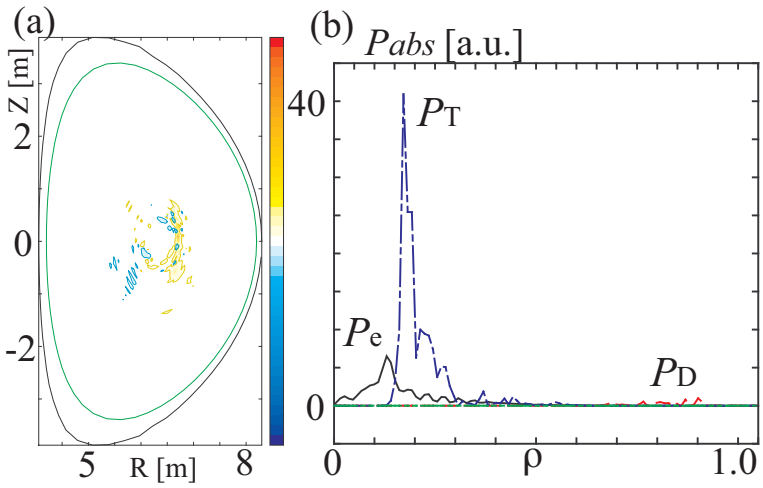

Figure 4.4: ICRF wave power absorption profiles (a) on poloidal cross section and (b) in radial direction. In this example, plasma consist of four speices, electron, deuteron, triton, and helium ion. Fig. 4.4-(b) shows the absorption profile for triton. ITER magnetic configuration is applied, so toroidal magnetic field strength at magnetic axis is 5.3T, and major radius is 6.2m. RF wave frequency is 55MHz.

4.2 Wave-plasma interaction

4.2.1 In the case of uniform magnetic field

The propagation of RF electric field which accelerate plasma particles is calculated by TASK/WM. Figs. 4.4 shows the example of RF power absorption profile calculated by TASK/WM. Although the RF electric field is obtained by TASK/WM on 2D poloidal cross section, TASK/FP is spationally one dimensional. Therefore the quasi-linear diffusion should be bounce averaged. In the case of uniform magnetic field, $\lambda = 1$ and $\psi(s) = 1$ for all particles and orbits.

Figs. 4.5 show an example of time evolution of the momentum distribution function of triton. It is found that the perpendicular momentum increases gradually due to the second harmonic cyclotron resonance.

4.2.2 In the case of non-uniform magnetic field

Due to the non-uniform magnetic field effect, some particles are trapped in a weak magnetic field region. These trapped particles are accelerated by the RF waves in the different way from that of passing particles.

In non-uniform magnetic field, when the particle moves from weak magnetic field point to strong magnetic field point, the parallel velocity decreases due to the conservation of magnetic moment. It means the particle stays longer in the strong magnetic field region than the weak magnetic field region. Especially, since the parallel velocity of the trapped particle becomes nearly zero at the bounce point, the trapped particle

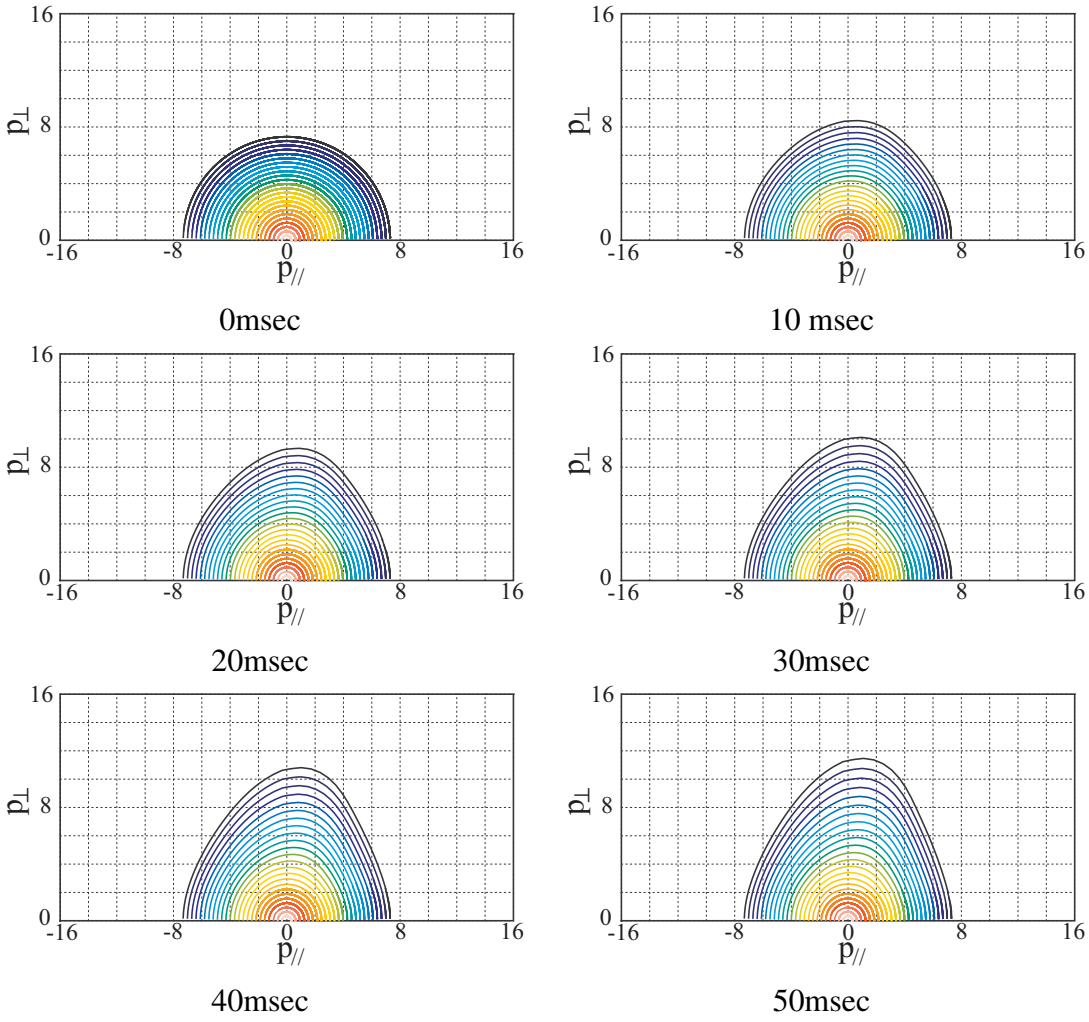

Figure 4.5: Time evolution of the momentum distribution function of triton at $\rho = 0.17$ is displayed. This radial point is consistent to the peak of wave absorption. In this example, the absorption power density is $0.90\mathrm{MW/m^3}$.

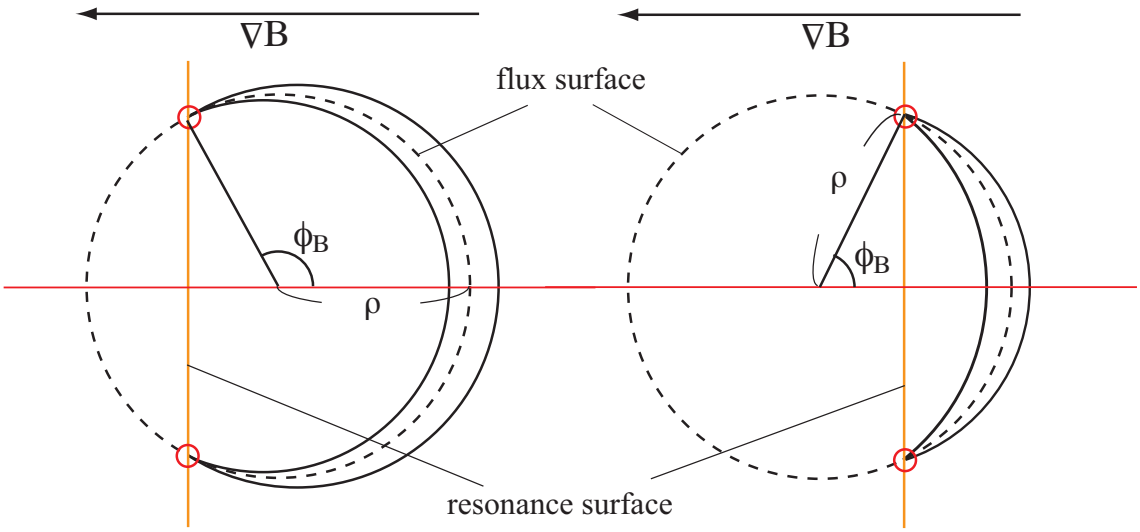

Figure 4.6: The trapped particle orbit and resonance surface are shown in two cases. One has a resonance surface in high magnetic field region (left), and another has it in low magnetic field region (right). These trapped particle orbits have a pitch angle $\theta_B \leq \theta_0 < \pi/2$. If the trapped particle bounce on the resonance surface, the trapped particle accelerate strongly.

stays relatively long time at the bounce points than the other region on the flux surface. Therefore, the trapped particles which bounce at the resonance surface, as is shown in Fig. 4.6, are accelerated strongly. Now we call such a pitch angle as θ_{tip}, and it satisfies $\theta_B < \theta_{tip} < \pi/2$. Conversely, when the trapped particle orbits do not reach the resonance surface, the particle has very little acceleration. Such a pitch angle is larger than θ_{tip}, namely $\theta_{tip} < \theta_0 < \pi/2$. Because of the difference of acceleration, the momentum distribution function of heated species has two tips, as is shown in Figs. 4.7.

Figs. 4.7 show the time evolution of the momentum distribution function of triton at the peak of wave absorption, $\rho = 0.17$. Since our bounce average assumes zero banana width, the momentum distribution function is symmertic around $p_\parallel = 0$ axis in the trapped region.

4.3 Conductivity

When working with electron-electron collision operators, it is useful to have some benchmark test against analytically in order to check their numerical implemention. A useful benchmark test is provided by the electrical conductivity, which is the ratio of electrical current to electric field in the limit of $E \to 0$.

To numerically verify our model, we compare the electrical conductivity calculated by our model with that in the previous work [20]. The electron-electron collision operator of the previous work is linearized one (for non-relativistic case),

$$C_{\rm lin}(f_e(\boldsymbol{v})) = C(f_e(\boldsymbol{v}), f_{em}(v)) + C(f_{em}, f_e(\boldsymbol{v})), \tag{4.1}$$

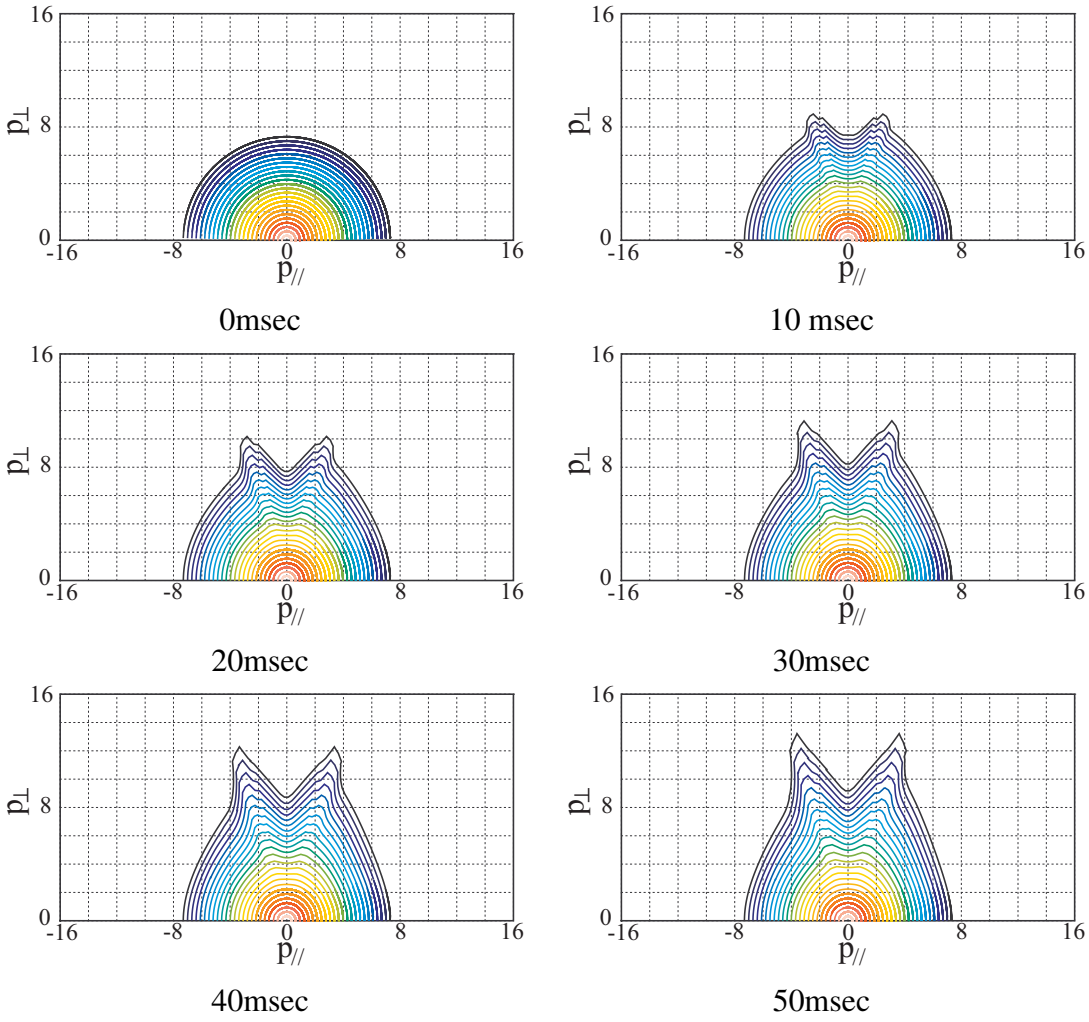

Figure 4.7: Time evolution of the momentum distribution function of triton with non-uniform magnetic field effect is displayed. This radial point is consistent to the peak of wave absorption. In this example, the absorption power density is $0.94\mathrm{MW/m^3}$.

Model	$Z_i = 1$	$Z_i = 2$	$Z_i = 5$	$Z_i = 10$
Reference value [20]	7.429	4.377	2.078	1.133
Our calculation	7.370	4.335	2.054	1.118

Table 4.1: The electrical conductivity for various ion charge is shown with the DC electric field 0.001V/m. The conductivities are normalized to $n_e q_e^2/m_e \nu_{te}$, where $\nu_{te} = \tau_{te}^{-1} = \Gamma^{e/e}/v_{te}^3$.

Model	$Z_i = 1$	$Z_i = 2$	$Z_i = 5$	$Z_i = 10$
Reference value [20]	7.160	4.180	1.963	1.064
Our calculation	7.041	4.110	1.930	1.046

Table 4.2: The relativistic electrical conductivity for various ion charge is shown with the DC electric field 0.001V/m and $\Theta = T_e/m_e c^2 = 0.02$. The conductivities are normalized to $n_e q_e^2/m_e \nu_{te}$.

or truncated operator (for relativistic case)

$$C_{\rm trun}(f_e(\boldsymbol{v})) = C(f_e(\boldsymbol{v}), f_{em}(v)) + C(f_{em}, f_e^{(1)}(v)P_1(\mu)). \tag{4.2}$$

On the other hand, our electron-electron collision operator is the non-linear operator

$$C(f_e(\boldsymbol{v})) = \sum_{l=0}^{\infty} C(f_e(\boldsymbol{v}), f_e^{(l)}(v)P_l(\mu)). \tag{4.3}$$

which is explaned in Sec. 3.3 and 3.4. An approximate collision term which assumes $m_i \to \infty$ is used for electron-ion collision term in all cases, because the ions are so massive relative to the electrons. The exressions of the diffusion coefficients in this limit are given by [20]:

$$D_{cvv}^{e/i} = F_{cv}^{e/i} = 0 \tag{4.4}$$

$$D_{c\theta\theta}^{e/i} = \Gamma^{e/e}\frac{Z_i}{2v}, \tag{4.5}$$

where

$$Z_i = -\frac{q_i \ln \Lambda^{e/i}}{q_e \ln \Lambda^{e/e}}. \tag{4.6}$$

In these calculations, non-uniform magnetic field effect is not included.

The conductivities for electrons are listed in Table 4.1 (non-relativistic) and 4.2 (relativistic) for each model. In these calculation, Legendre polynomials are calculated up to $l = 1$. Since the agreement in the both tables is fairly good, the validity of conductivity of our model is confirmed.

Chapter 5

Multi-species heating without radial transport

In general, fusion plasma consists of several species, and each species are heated by different heating schemes. Since the distortion level of the momentum distribution function is different for the each heating scheme, the time evolution of the momentum distribution function for each species should be calculated simultaneously. Fokker-Planck component TASK/FP can calculate the evolution for multi-species simultaneously. In this chapter, some simulation results for multi-species heating without radial transport are presented.

5.1 Plasma parameters and initial conditions

We carried out numerical analysis of multi-species heating with the plasma parameters simulating ITER as listed in Table 5.1. The plasma consists of four particle species, electron, deuteron, triton, and helium ion, respectively. Each species is heated by different scheme, such as NBI, ICRF, ECH, and fusion reaction. NBI is particle and energy source of deuteron. And its energy is transferred to the other species through collisions. ICRF wave accelerates electron and triton through Landau resonance and second harmonic cyclotron resonance. ECH wave also accelerates electron through electron cyclotron resonance. Moreover, triton and helium ion have fast particle source generated by fusion reaction. D-D reaction generates 1 MeV triton, and D-T and T-T reaction generate 3.5 MeV and 1.25 MeV helium ions. These fast ion generations are assumed to be isotropic. Furthermore, each species transfers its power to the other species through collisions. The image of such a heating mechanism is illustrated in Fig. 5.1.

In the following sections, the non-linear Coulomb collision model is applied for the collision term, and radial transport term is neglected. Because of the lack of radial transport, the stored energy continue to increase and don't saturate. The other models adopted in this section are listed in Table 5.2.

major radius	R_0	6.2m
minor radius	a	2.0m
elongation	κ	1.7
triangularity	δ	0.33
magnetic field on axis	B_0	5.3T
initial temperature on axis	T_0	20.0keV
initial temperature on surface	T_s	2.0keV
initial density on axis	n_0	$1\times10^{20}/\mathrm{m}^3$
initial density on surface	n_s	$1\times10^{19}/\mathrm{m}^3$
initial deuterium ratio	n_D/n_e	0.5
initial tritium ratio	n_T/n_e	0.5
NBI energy	E_{NBI}	1MeV
NBI pitch angle	θ_{NBI}	$\pi/9$
α particle energy	E_α	3.5MeV
ICRF wave frequency	f_{IC}	55.0MHz
ECH wave frequency	f_{EC}	185GHz

Table 5.1: ITER like plasma parameters

	MODEL
Motion	Relativistic
Collision	Non-linear
Orbit average	Bounce average
Radial transport	None
Absorption power	Constant in time

Table 5.2: Adopted models

5.1.1 Initial state

At the beginning of our calculation, each momentum distribution function is Maxwellian, and the radial profiles of temperature and density are distributed parabolic as is shown in Figs. 5.2.

$$n(\rho) = (n_0 - n_s)(1 - \rho^2) + n_s$$
$$T(\rho) = (T_0 - T_s)(1 - \rho^2) + T_s$$

5.1.2 Heat source

The propagation of ICRF wave electric field is calculated by TASK/WM. Figs. 5.3 show the ICRF wave power absorption profiles. Using the wave electric field calculated by TASK/WM, TASK/FP obtains quasi-linear diffusion coefficients, and then, calculates power absorption profile for electron and triton. The absorption profiles are

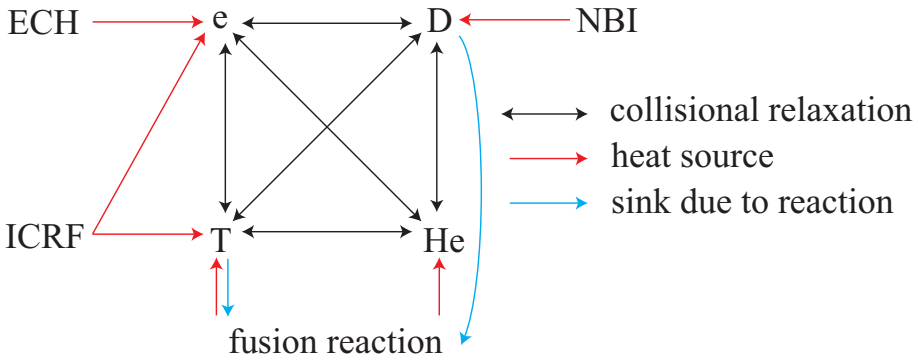

Figure 5.1: The image of plasma heating. Each species is heated not only external heating or fast ion source, but also collisional power transfer among species through collision.

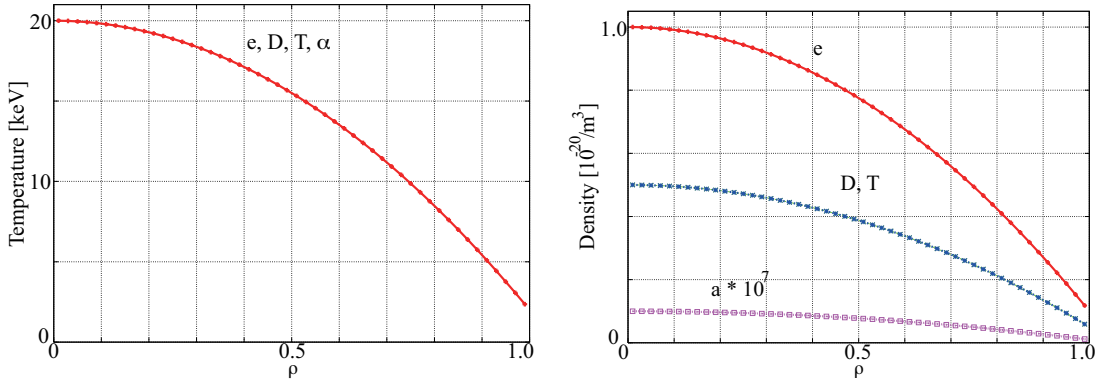

Figure 5.2: Initial density and temperature profiles

shown in Fig. 5.4. Generally, since the dielectric tensor depends on the momentum distribution function of plasma species, the propagation will be affected by plasma heating. In this chapter, however, the profile of wave electric field is assumed to be constant in time. ECH and NBI power absorption profiles are also shown in Fig. 5.4. Here, on the contrary of ICRF, ECH wave electric field is calculated by a simple model. In addition, these absorption profiles are also fixed in time. Therefore, the absorption power by NBI, ICRF, and ECH during the simulation are 31.6MW, 20.5MW, and 20.4MW, respectively.

On the other hand, since the fast ion generation rate by fusion reaction depends on the momentum distribution function, the absorption power due to fusion-generated fast ion source varies in time. The power of the source at initial state is 78.3MW for helium ion, and the loss due to fusion reactions for deuteron and triton are -0.843 MW and -0.581MW, respectively. The radial profile of the source power for helium ion is also shown in Fig. 5.4. Because of the small values of the loss power due to the fusion reactions, the power loss of deuteron and triton is not shown in Fig. 5.4.

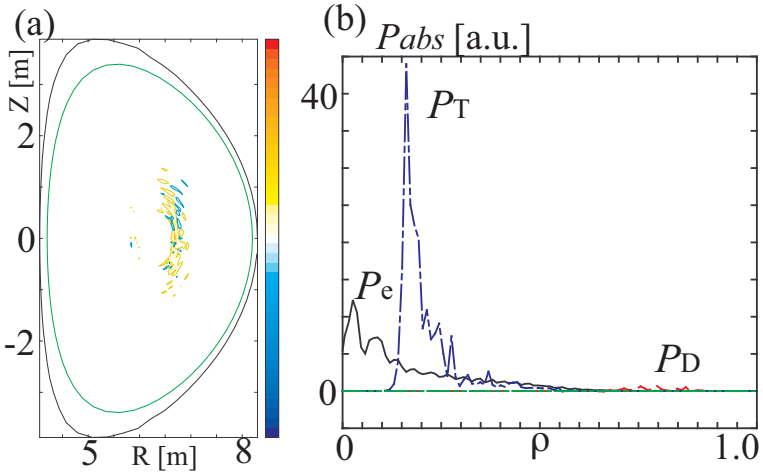

Figure 5.3: Wave absorption profiles calculated by TASK/WM. (a) power absorption for triton, (b) radial profile of power absorption for each species.

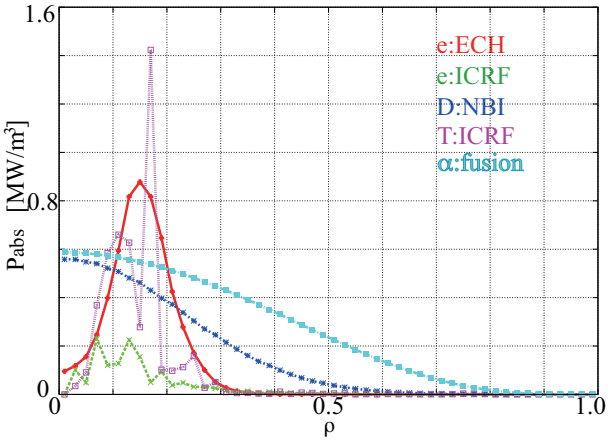

Figure 5.4: The power absorption profiles of ECH, ICRF, and NBI for each species. ICRF absorption profiles for electron (green) and triton (purple) are calculated using the wave electric field calculated by TASK/WM. These heat profiles are fixed in time during the simulation of this chapter. The absorption powers for NBI, ICRF, and ECH are 31.6MW, 20.5MW, and 20.4MW, respectively. ICRF absorption power consists of 4.72MW for electron and 15.8MW for triton. In this figure, the only α particle source power varies in time.

5.2 At 1 sec after the onset of heating

First, the simulation is done for 1 second with the several heatings introduced at previous section. Figs. 5.5 and 5.6 show the contour of the heated momentum distribution function for each species at several radial points. Since the relaxation time of electrons is very short compared to the other species, there is little distortion of the momentum distribution function of electron. Conversely, since deuteron, triton, and helium ion have slow relaxation processes rather than electron, the distortion of the momentum distribution function is clearly observed. NBI absorption profile have gentle slope as is shown in Fig. 5.4. Therefore the contour of the momentum distribution function of deuteron becomes smaller gradually as point moves radially outward. In contrast, there is a drastic difference between the contour of triton at $\rho = 0.17$ and $\rho = 0.37$ in Fig. 5.6. This is because the ICRF wave absorption profile has a strong peak at $\rho = 0.17$. At the absorption peak, since tritons are accelerated by second harmonic cyclotron resonance, the perpendicular momentum of triton increase strongly. At other point, tritons are hardly accelerated by wave, and then, only the fast triton source generated by D-D reaction stands out. The contours of helium ions show the fast α particle source at 3.5MeV $\sim \bar{p} = 17$, and these fast ions are becoming thermal ions through collisional slowing down.

Figs. 5.7 show the radial profile of two kind of temperatures. Here, the bulk temperature is estimated in the $p < 4p_{th}(\rho)$ region[1]. The main heat source of deuteron is NBI, and the energy of NBI is 1MeV= $\bar{p} = 10$. Thus, only the injected deuterons slowed down to around the thermal momentum are estimated in bulk temperature. This is the reason of the large differences between the deuteron averaged energy temperature and bulk temperature. With the similar reason, there are some differences for the temperature profile of triton at the vicinity of the wave absorption peak. On the other hand, since the momentum distribution of electron is thermalized sufficiently, there are little difference between averaged energy temperature and bulk temperature.

Figs. 5.8 show the time evolution profiles of two kind of temperature which is volume averaged. As same as the radial profiles of temperatures, it is found that injected deuteron is not sufficiently thermalized yet. Moreover, for triton, because the strong distortion of the momentum distribution function occurs only at the vicinity of the peak of absorption, there are little differences between volume averaged temperatures.

It have been clear by shown in the previous chapter that the fusion reaction rate is strongly affected by the existence of fast ions. Since the averaged energy temperature which is estimated with fast ions increases for each species, the source power of fusion reaction also increases. Due to the plasma heating, the source power of fusion reaction for helium ion increases from 78.3MW to 109.5MW. Figs. 5.9 show the power absorption profiles at 1 sec after the onset of heatings. From Fig. 5.9-(b), the increase of the source power is remarkable at the vicinity of the peak of wave absorption, $0.05 < \rho < 0.2$. It is consistent with the radial profile of averaged energy temperature of deuteron and triton.

Fig. 5.10-(a) shows the radial profiles of collisional power transfer density for each

[1] $p = \bar{p}p_{th}(0)$

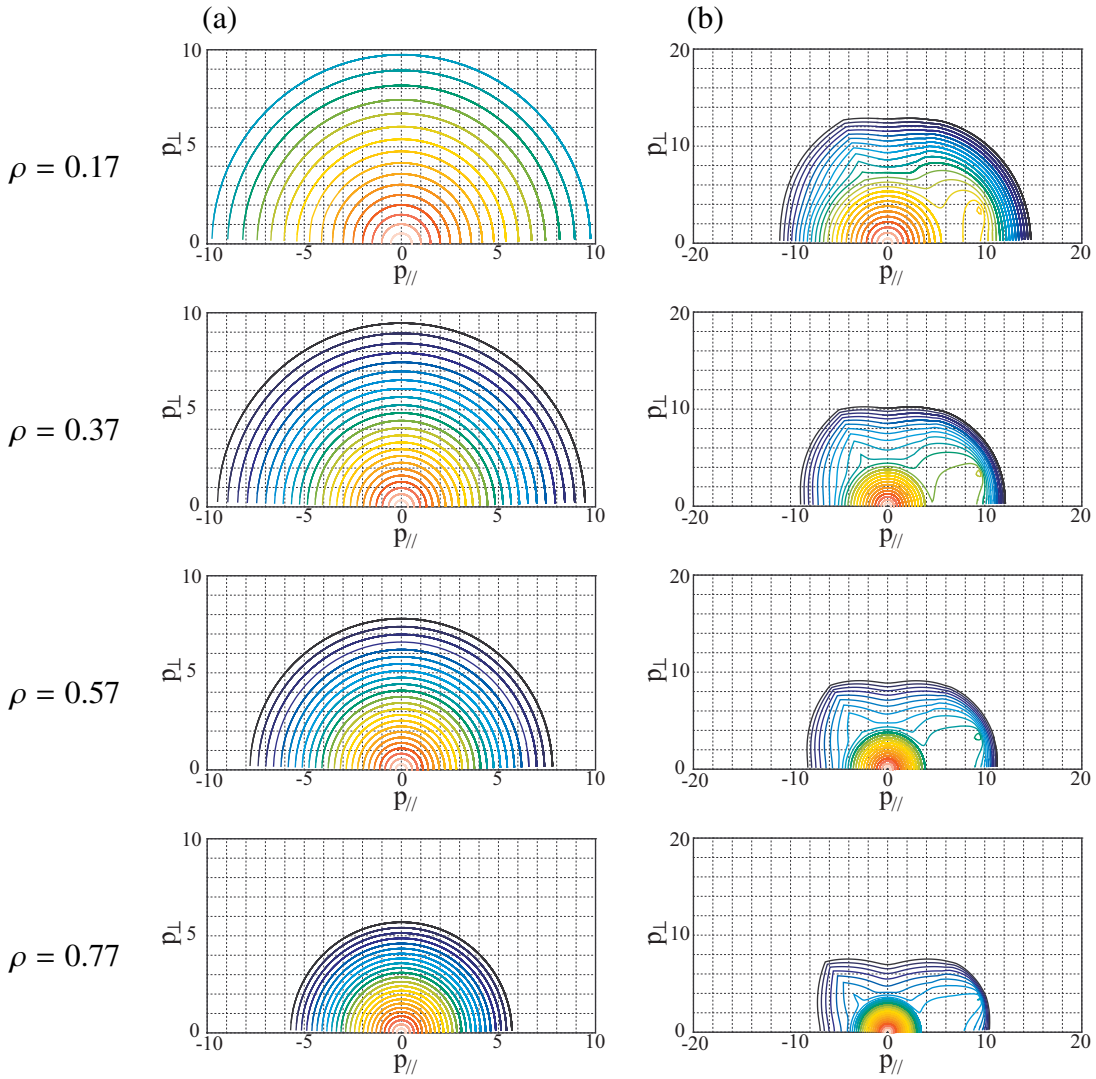

Figure 5.5: The contour of the momentum distribution functions of electron and deuteron in 2D momentum space at several radial points are shown. The radial point $\rho = 0.17$ is consistent to the point of the ICRF wave absorption peak for triton.

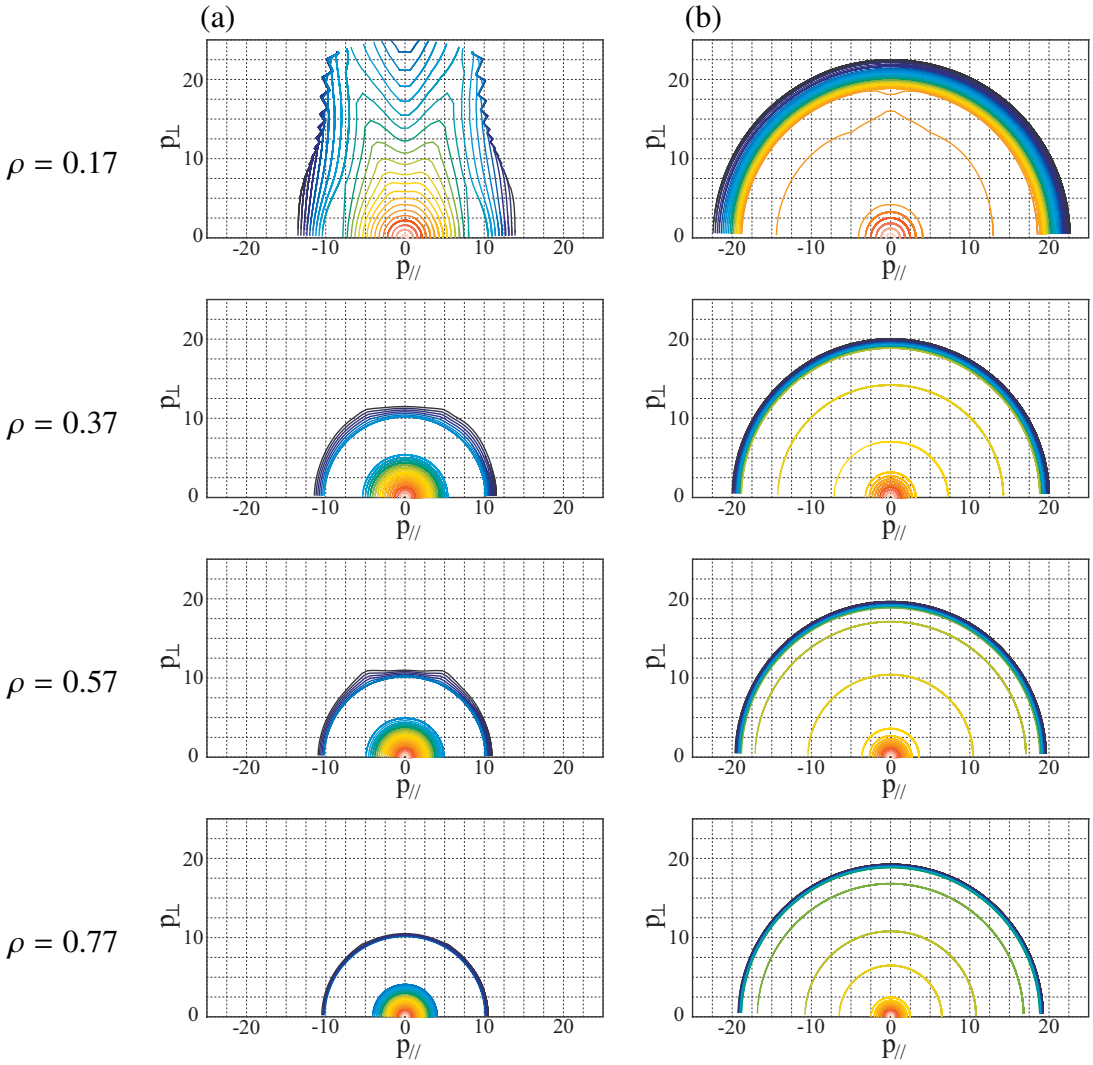

Figure 5.6: The contour of the momentum distribution functions of triton and helium ion in 2D momentum space at several radial points are shown.

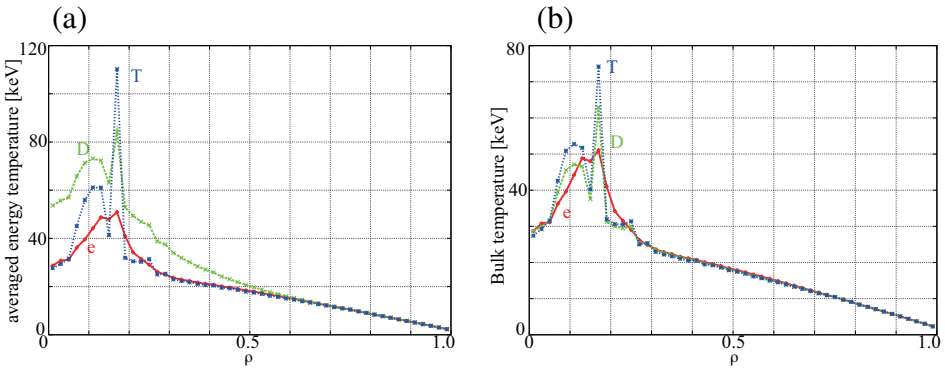

Figure 5.7: Two kind of temperature profiles at 1 sec are shown. (a) averaged energy temperature. (b) bulk temperature.

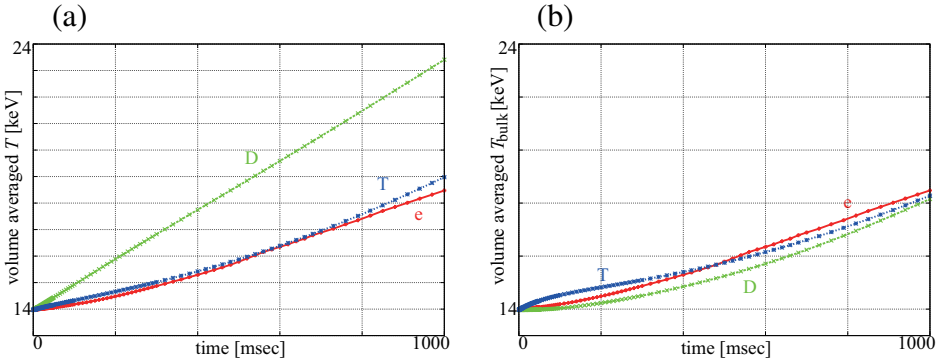

Figure 5.8: The time evolution of volume averaged T and T_{bulk}. T and T_{bulk} denote averaged energy temperature and bulk temperature, respectively.

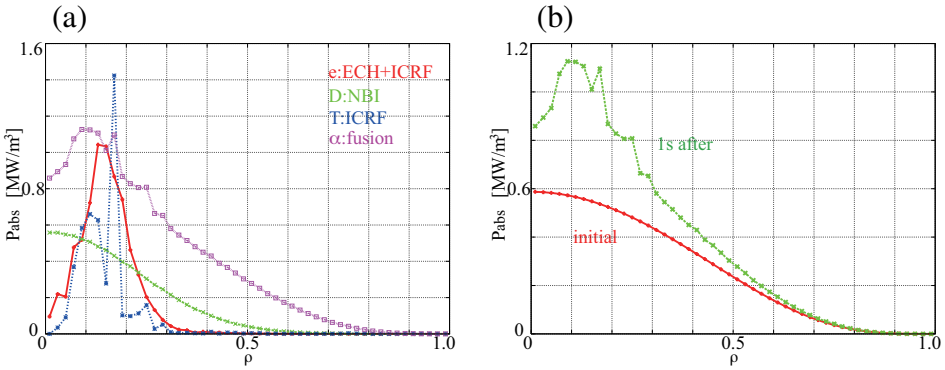

Figure 5.9: The power absorption profiles at 1 sec after the onset of heating are shown. Right figure shows the input power profiles of fast α particles at initial state and 1 sec later.

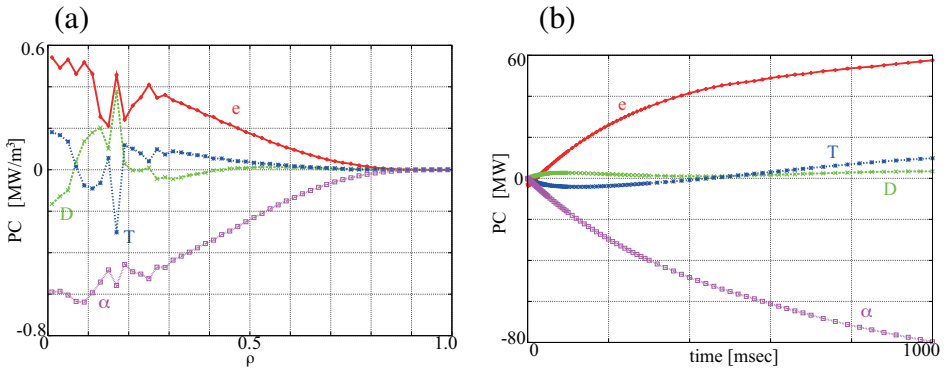

Figure 5.10: The collisional power transfer profiles are shown. (a) The radial profile at 1 sec after. (b) The time evolution profile.

species. When the value of the density for the species s is positive, the species s gain power through collisions with the other species. From 5.10-(a), fusion generated α particles lose its energy through collision, and the power transfers to electron. The profiles of electron, deuteron, and triton have a spike at $\rho = 0.17$. The spike of electron and deuteron is positive one, conversely, triton profile has a negative spike. The spike is a result of the generation of fast triton due to ICRF acceleration. This is because, in the extremely fast region, triton-electron collision is dominant, and in the slightly fast region, triton-deuteron collision is dominant.

Fig. 5.10-(b) denotes the time evolution of the collisional power transfer for each species. In this simulation, since the energy sink is not included, the simulation can not reach a steady state. From Fig. 5.10-(b), it is found that the collisional power gain of electron is increasing. This is because, the temperatures of ions are continue to increase, and the source power of fusion reaction also continue to increase.

5.3 Artificial loss in order to obtain a steady state

Now we introduce artificial energy loss mechanism in order to obtain steady state without radial transport. The artificial loss consists of loss term $-f/\tau_L$ and compensating source term $f_{maxwell}/\tau_L$, where τ_L is a typical relaxation time. Including the loss term, the stored energy saturates with density conservation and without radial transport.

We simulate the plasma heating for 1 sec with the artificial loss term and the same parameters to the previous section. Figs. 5.11 show the time evolution of volume averaged T and T_{bulk}. From both figures, it is found that the both temperature of deuteron and triton saturate in time. Conversely, the temperatures of electron still increases. This is because the power transfer from fast α particle to electron is large, and then the power is still greater than the loss power due to the sink term. Figs. 5.12 are the power transfer profiles. From Fig. 5.12-(b), is is found that the collisional power transfers also saturates. It means the all heating power for electron saturates. Therefore, the electron temperatures saturate when the tail of the momentum distribution function of electron

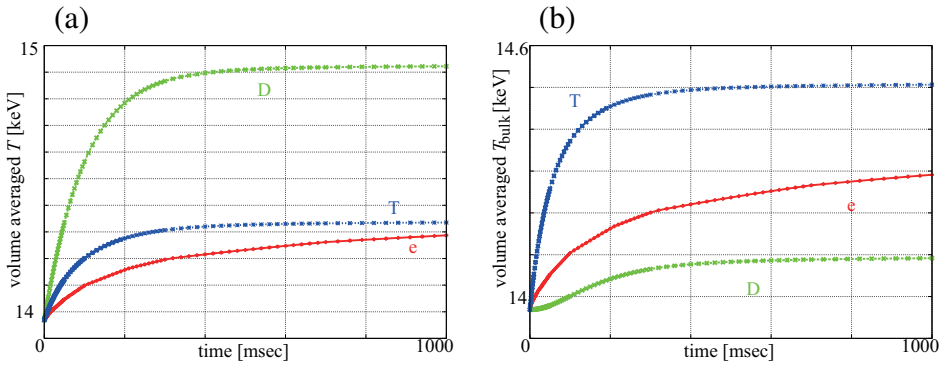

Figure 5.11: The time evolution of volume averaged (a) T and (b) T_{bulk} for each species except helium ion.

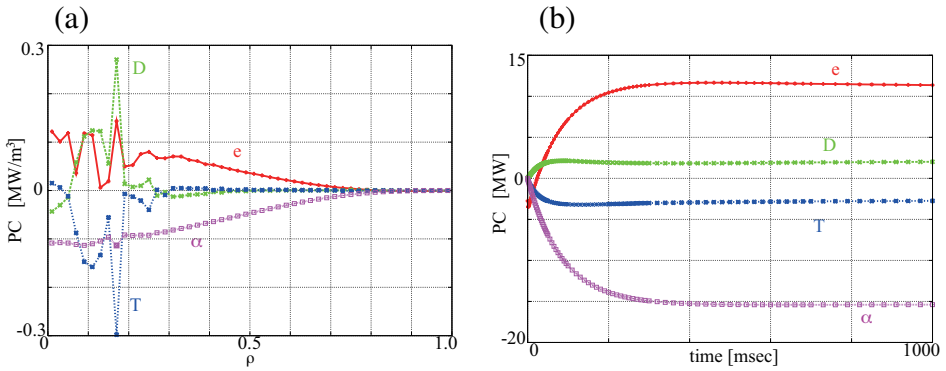

Figure 5.12: The collisional power transfer profiles are shown. (a) The time evolution profile. (b) The radial profile at 1 sec after.

develop and loss power due to $-f/\tau_L$ increases to the level of the all heating power.

Figs. 5.13 show the radial profiles of the two temperatures. Due to the power loss, the peak of temperatures become smaller than the case without loss term. The decrease of the peak of temperature denotes the decrease of fast ions. The lack of the fast ions cause the fusion reaction power decreasing. Figs. 5.14 show the radial profile and time evolution profile of the source power generated by fusion reaction. From Figs. 5.14, it is certain that the increase of the fusion reaction power is weak compared the the case without loss.

Figs. 5.15 and 5.16 show the contour of the momentum distribution function for each species at the peak of the resonance, $\rho = 0.17$, in several time steps. Compared with Figs. 5.5 and 5.6, it is clear that the development of a tail in the momentum distribution function is weak. Moreover, it is found that the development of the tail of the momentum distribution function becomes slow as the time step advances. From Figs. 5.11 and 5.12-(b), it is presumed that each species reaches steady state around 400ms, and the guess is confirmed by Figs. 5.15 and 5.16.

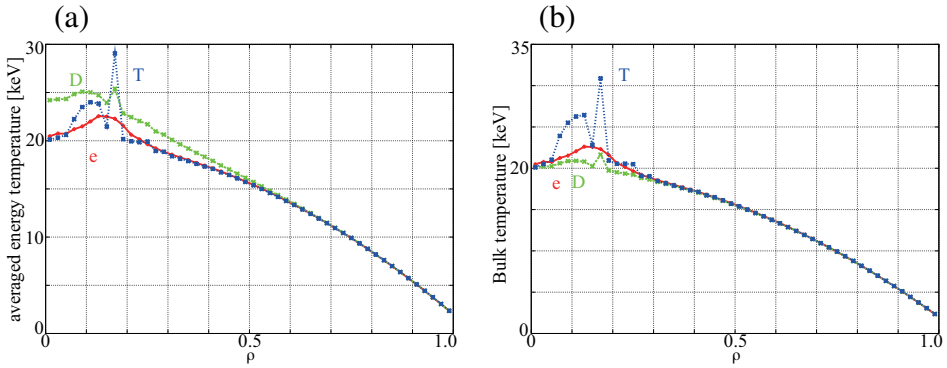

Figure 5.13: Two kind of temperature profiles at 1 sec are shown. (a) averaged energy temperature. (b) bulk temperature.

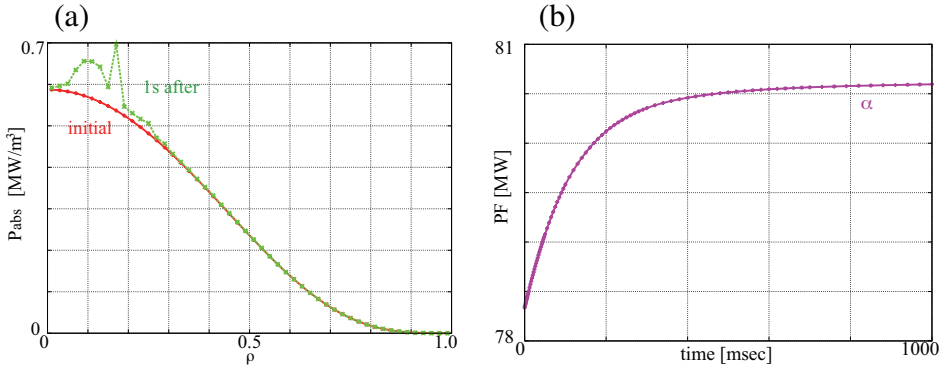

Figure 5.14: (a) The radial profile and (b) time evolution profile of the source power generated by fusion reaction are shown.

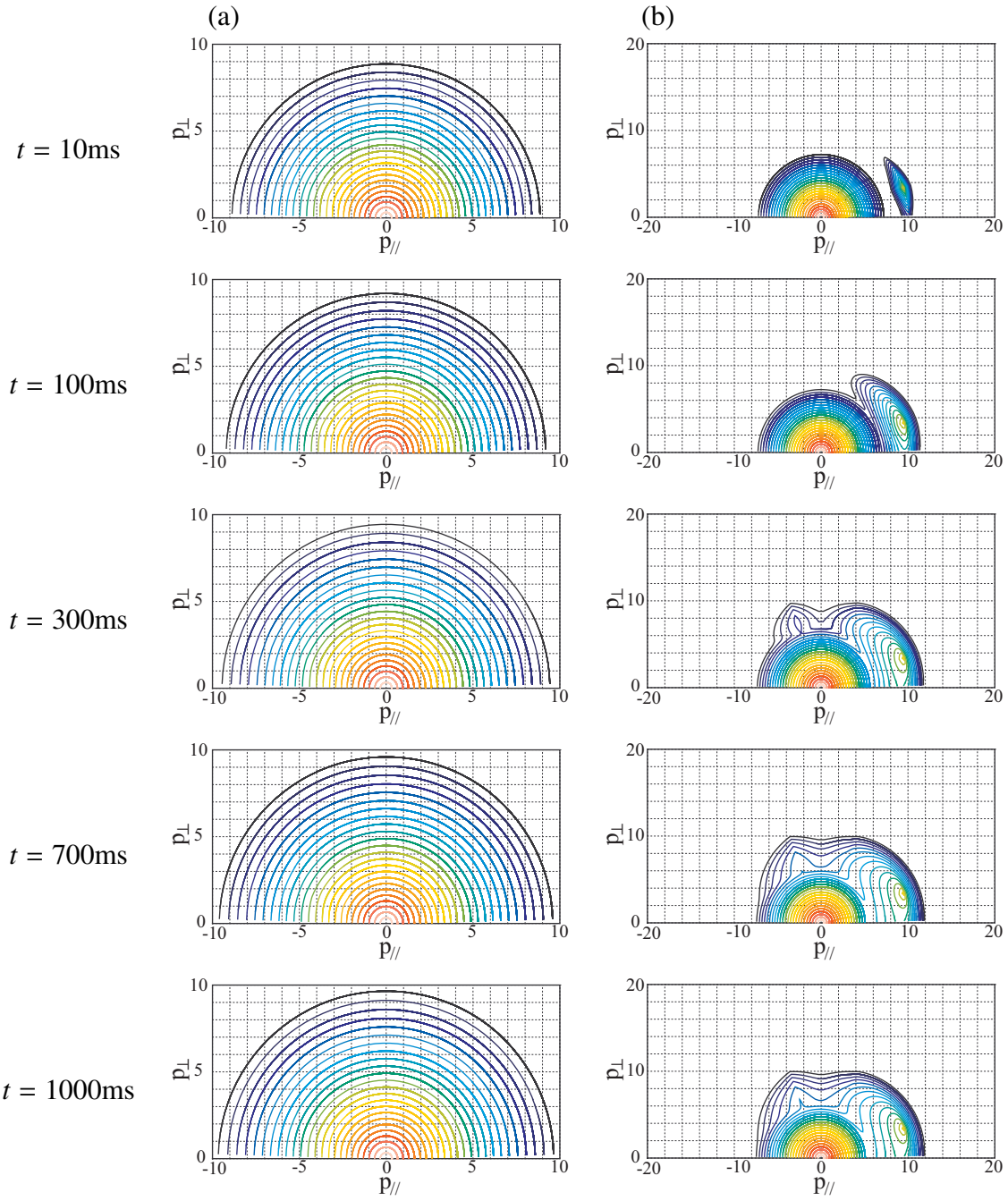

Figure 5.15: The contour of the momentum distribution function for (a) electron and (b) deuteron at $\rho = 0.17$ in several time step are shown.

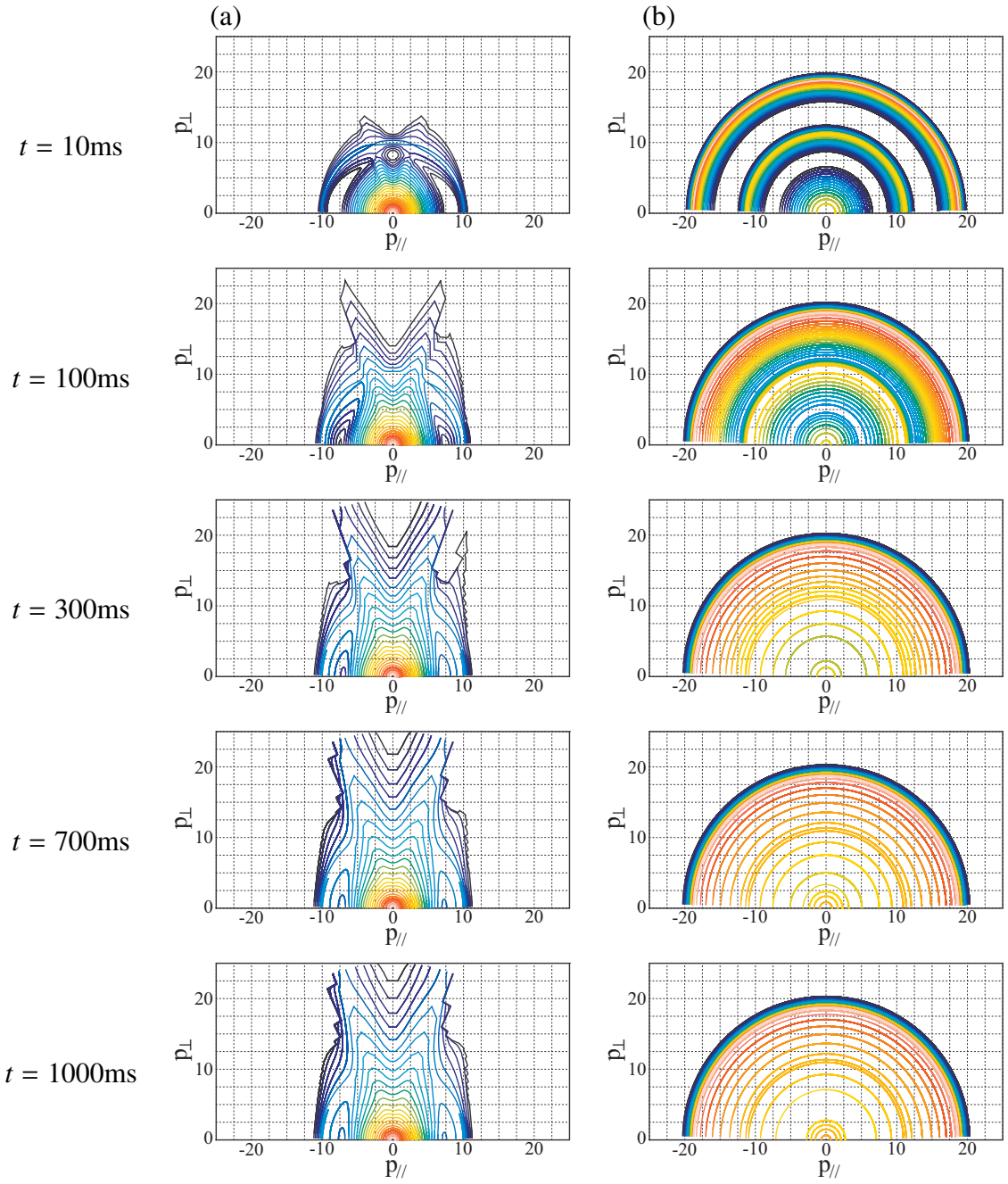

Figure 5.16: The contour of the momentum distribution function for (a) triton and (b) helium ion at $\rho = 0.17$ in several time step are shown. The fast α particle source at $\bar{p} \sim 11$ and $\bar{p} \sim 19$ denote T-T and D-T reaction sources.

Chapter 6

Multi-species heating with radial transport

In the previous section, the plasma heatings without radial transport are analyzed. The results show that the radial profiles have a strong peak at the peak of absorption, and when the artificial loss is not included, the plasma temperatures continue to increase. In practice, however, the radial transport causes the broadening of the profiles, and the power loss due to the energy transport to out of the plasma will balance to the heating power. Moreover, in general, the transport depends on the momentum of the particle. Therefore, some radial transport models, introduced in Sec. 3.6, are implemented.

In this chapter, simulation results for multi-species heating with radial transport are shown.

6.1 Case without momentum dependence of D_ρ

6.1.1 Initial conditions

Parameters

We carried out numerical analysis of multi-species heating again with the plasma parameters simulating ITER plasmas listed in Table 6.1. Only the ion density rates are different from that of previous chapter. The initial α particle density rate is set to $n_\alpha/n_e = 0.01$. This is because when the fusion generated α particle becomes greater than the initial density, it gives bad effect to the iteration convergency and the calculation accuracy.

Models

In the following sections in this chapter, the same models which is applied in the previous chapter are used except radial diffusion model. Table 6.2 shows the models adopted in the calculation of this section. In this chapter, the value of the radial diffusion coefficients are set as $D(0) = 0.1\mathrm{m/s}^2$ and $D(1) = 1.0\mathrm{m/s}^2$, where $D(0)$ and $D(1)$ are defined in eq. (3.139).

major radius	R_0	6.2m
minor radius	a	2.0m
elongation	κ	1.7
triangularity	δ	0.33
magnetic field on axis	B_0	5.3T
initial temperature on axis	T_0	20.0keV
initial temperature on surface	T_s	2.0keV
initial density on axis	n_0	$1\times10^{20}/\mathrm{m}^3$
initial density on surface	n_s	$1\times10^{19}/\mathrm{m}^3$
initial deuterium ratio	n_D/n_e	0.49
initial tritium ratio	n_T/n_e	0.49
initial α particle ratio	n_α/n_e	0.01
NBI energy	E_{NBI}	1MeV
NBI pitch angle	θ_{NBI}	$\pi/9$
α particle energy	E_α	3.5MeV
ICRF wave frequency	f_{IC}	55.0MHz
ECH wave frequency	f_{EC}	185GHz

Table 6.1: ITER like plasma parameters.

	MODEL
Motion	Relativistic
Collision	Non-linear
Orbit average	Bounce average
Radial transport	Without momentum dependence (Sec. 6.1) With momentum dependence (Sec. 6.2)
Absorption power	Constant in time

Table 6.2: Adopted models

Initial distribution

The initial temperature and density profiles are parabolic and the initial momentum distribution function is Maxwellian for each species as same as the previous chapter. Only the values of n_D, n_T, and n_α at $\rho = 0$ and $\rho = 1$ are changed.

Heat source

As same as in the previous chapter, the propagation of ICRF wave electric field calculated by TASK/WM is used to the calculation of quasi-linear diffusion term in TASK/FP. The ICRF wave propagation is shown in Fig. 5.3. And then the initial power absorption profile of ECH, ICRF, NBI, and fast α particle generated by fusion reaction are shown in Fig. 5.4. The absorption power of NBI, ICRF, and ECH are constant in time and the values are 31.6MW, 20.2MW, and 20.4MW, respectively.

6.1.2 At 3 second after the onset of heatings

The simulation is carried out for 3 second with the several heating scheme. Figs. 6.1 and 6.2 show the contour of the heated momentum distribution function for each species at four radial points. As same as Figs. 5.5, since the relaxation time of electrons is very short compared with the other species, there are little distortion of the momentum distribution function of electron. Conversely, the momentum distribution function of the other species deformed strongly by the heatings. While there are large differences among Figs. 5.5, 5.6 and Figs. 6.1, 6.2 for the momentum distribution function of deuteron and triton, especially for triton. In the case without radial transport, there are few fast ion where the absorption power is weak as is shown in Fig. 5.6-(a). On the contrary, in the case with radial transport, there are not a few fast ions at the outer region as Fig. 6.2-(a). This is because the fast ion generated at the peak of power absorption diffuses to the less absorption region by the radial diffusion term. The reason of the clear differences between Fig. 5.6-(a) and 6.2-(a) is that the profile of power absorption for triton has strong spikes compared with the other species. Therefore the same transport phenomena happens for the other species.

Figs. 6.3 show the radial profile of two kind of temperatures, averaged energy temperature and bulk temperature, at 3 second. The bulk temperature is estimated at the $p < 4p_{th}(\rho)$ region. Unlike the Figs. 5.7 and 5.13, the spike of temperature is not appeared in Figs. 6.3 due to the radial transport. The time evolution profile of two kind of temperatures are shown in Figs. 6.5. The temperatures are volume averaged. Unlike the case with artificial loss, sec. 5.3, it is found from Figs. 6.5 that the plasma does not reach a steady state. Moreover, since the temperature profile of deuteron and triton become broad, the source power profile of fusion generated α particle also becomes broad (Fig. 6.5-(b)) compared to that of the previous section (Fig. 5.9-(b)). Similarly, collisional power transfer profile (Fig. 6.6-(a)) also become broad, especially around the peak of wave absorption, $\rho = 0.17$. Additionally, since the plasma has not reached s steady state, the collisional power transfer also does not saturate.

Figs. 6.7 show the radial profile of the radial power transfer by radial diffusion term for each species (a) at initial state and (b) at 3 sec after. It is found that the heated profile (Fig. 6.7-(b)) is similar to the profile of power absorption rather than that of the temperature. This is because that the radial power transfer strongly depends on $\partial f/\partial\rho$, and the peaked absorption makes $\partial f/\partial\rho$ large.

Fig. 6.8 show the radial profile of the total input power, ΔP, for each species. The total input power is sum of the absorbed power P_{abs} (Fig. 6.5-(a)), the collisional power transfer P_c (Fig. 6.6-(a)), and the radial transported power P_{Dr} (Fig. 6.7). In an initial state, the power absorption profile holds a dominant position of the total input power profile. On the other hand, at 3 sec after the onset of heating, the collisional power transfer profile holds a dominant position of the total input power profile, especially for electron and triton. This is because that the most of the power absorption profile for electron and triton are cancelled by the radial power transfer profiles as is shown in Fig. 6.7-(b), and the collisional power transfer develops as the plasma is heated.

Moreover, from Fig. 6.8-(b), it is found that the value of ΔP for electron is greater than that of the other species. One of the reason is that the density of electron is much

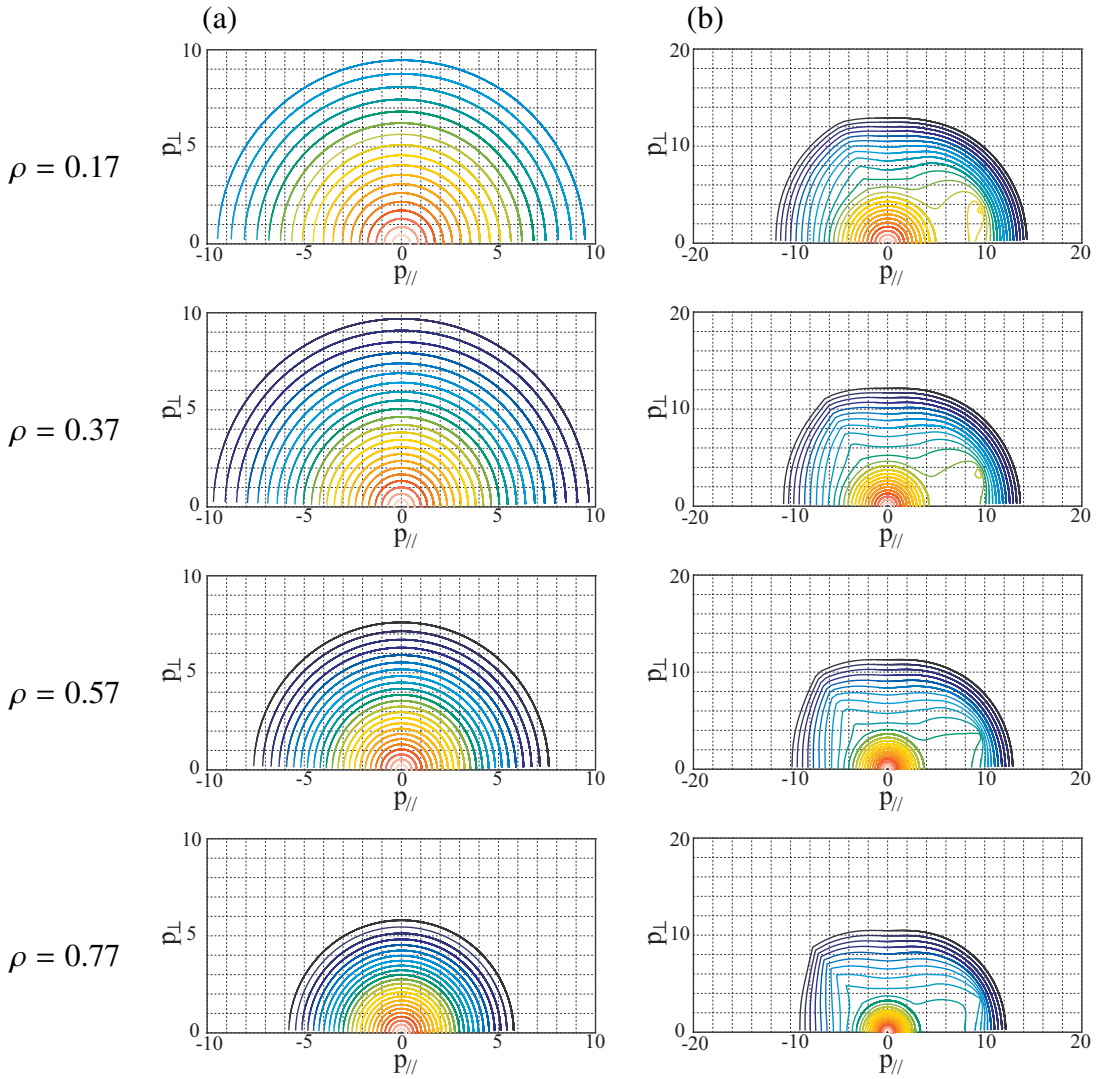

Figure 6.1: The contour of the momentum distribution functions of electron and deuteron in 2D momentum space at several radial points are shown. The radial point $\rho = 0.17$ is consistent to the point of the ICRF wave absorption peak for triton.

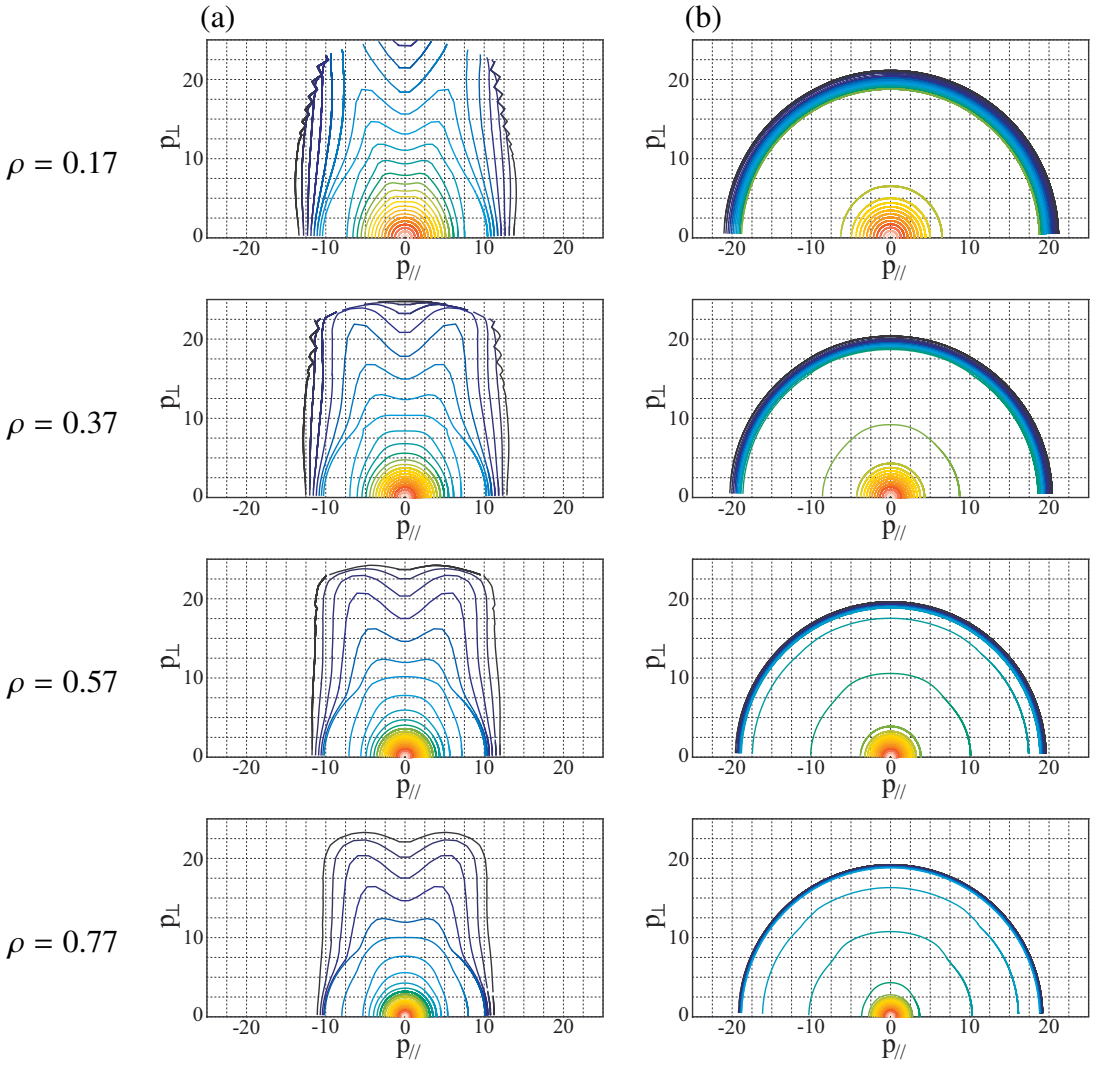

Figure 6.2: The contour of the momentum distribution functions of triton and helium ion in 2D momentum space at several radial points are shown.

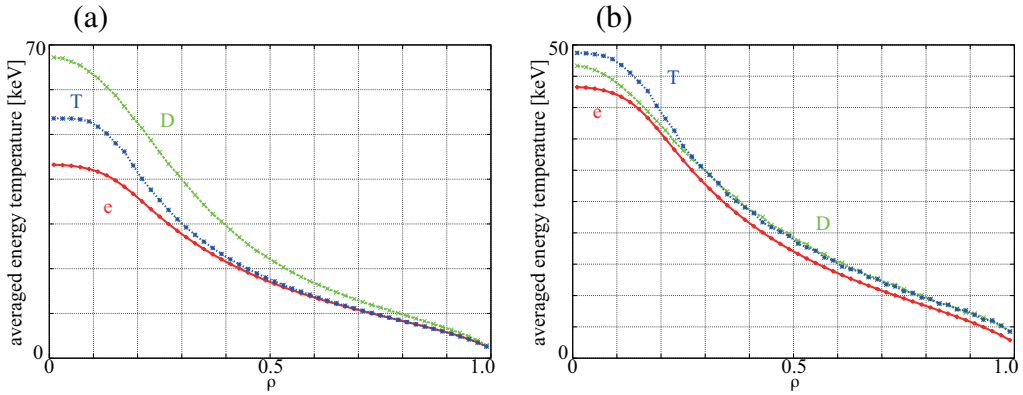

Figure 6.3: (a) The averaged energy temperature and (b) the bulk temperature for each species at 3 sec are shown.

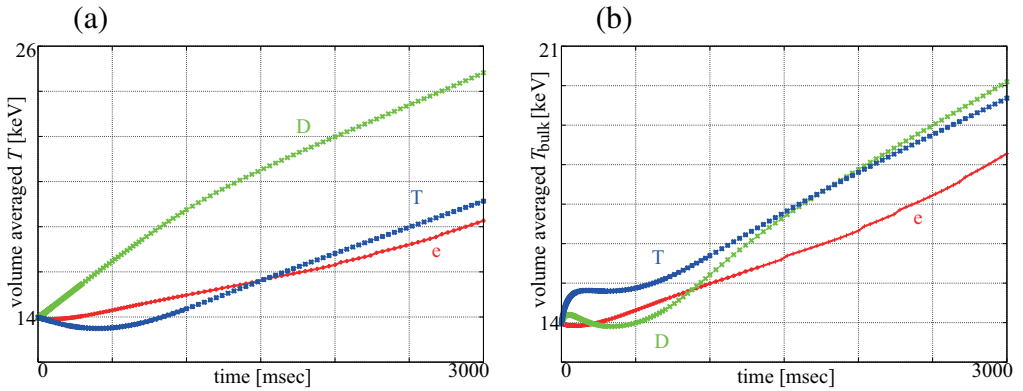

Figure 6.4: The time evolution of volume averaged (a) T and (b) T_{bulk}.

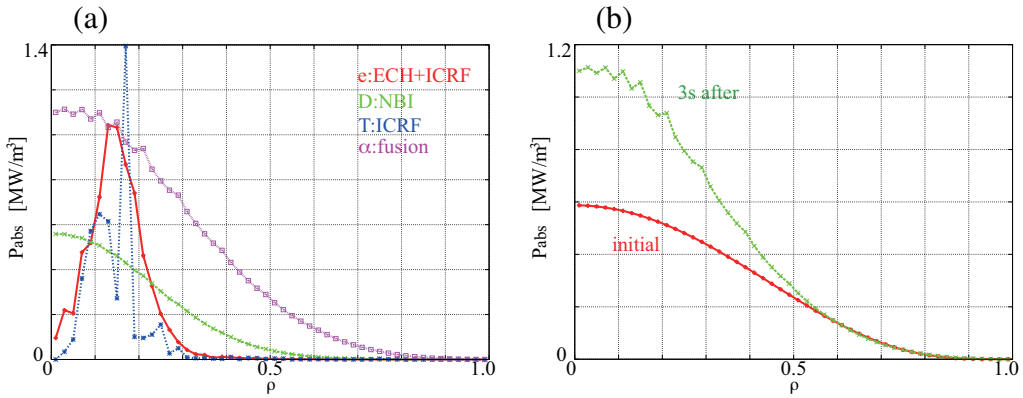

Figure 6.5: (a) The power absorption, P_{abs}, profiles at 3 sec after the onset of heating and (b) the source power of fast α particles generated by fusion reaction for initial state and 3 sec after are shown.

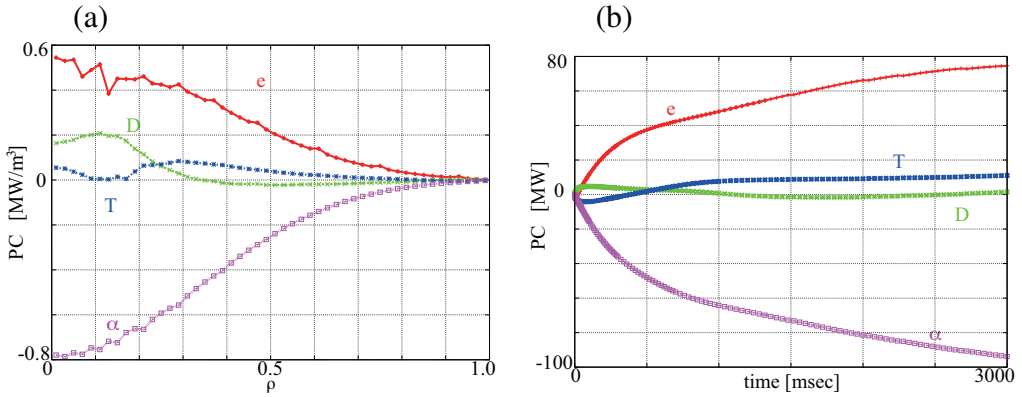

Figure 6.6: The collisional power transfer, P_c, profiles are shown. (a) The radial profile at 3 sec after. (b) The time evolution profile.

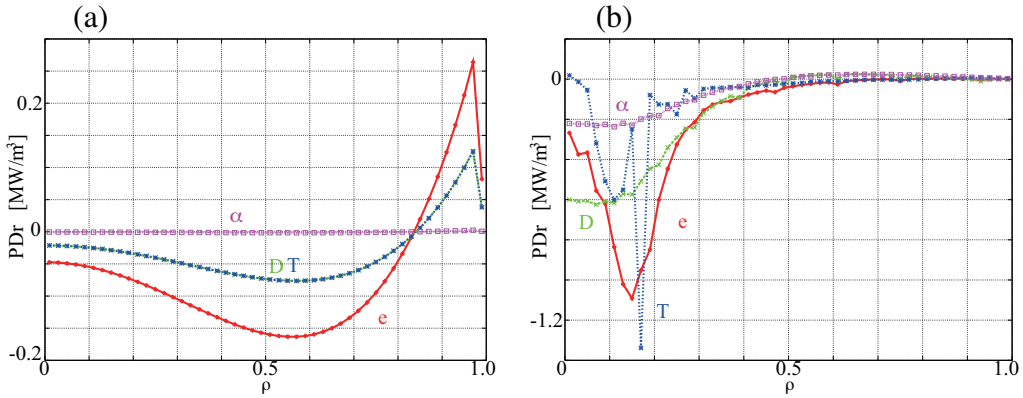

Figure 6.7: The radial profiles of the power transferred by radial diffusion term , P_{Dr}, are shown. (a) Initial profile. (b) the profile of 3 sec after.

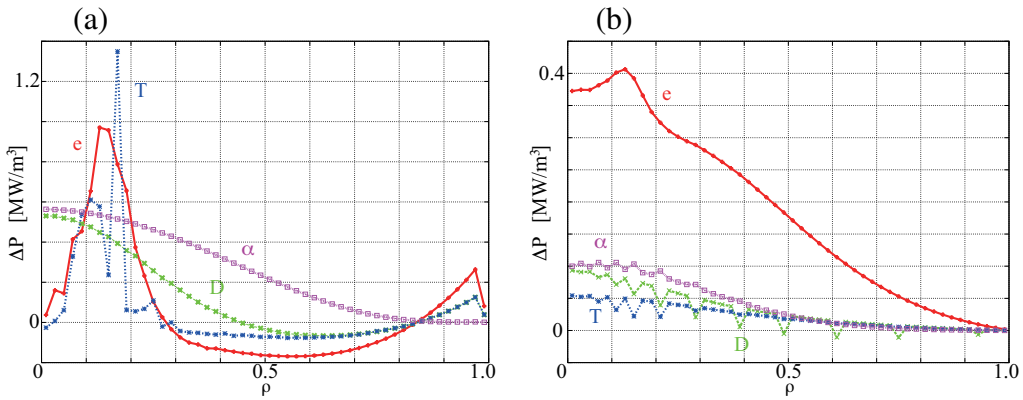

Figure 6.8: The radial profiles of the total input power, $\Delta P = P_{abs} + P_c + P_{Dr}$, are shown. (a) Initial profile. (b) the profile of 3 sec after.

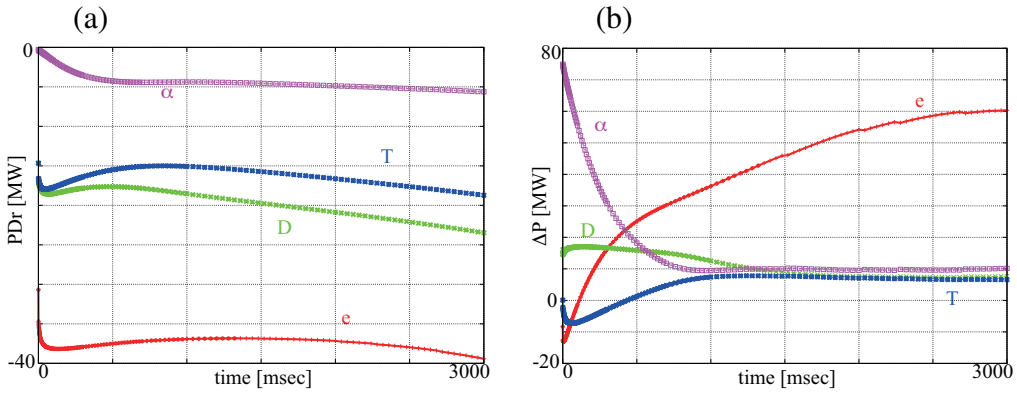

Figure 6.9: The time evolution profile of (a) PDr and (b) ΔP are shown.

higher than that of the other species. The other reason is that the temperature of electron is still less than that of the other species at 3 sec.

Figs. 6.9 show the time evolution of (a) radial power transfer and (b) total input power. As is shown in Fig. 6.9-(a), since the radial power transfer is developing, the plasma will reach the steady state at some future time. From Fig. 6.9-(b), it is found that the ΔP for deuteron and triton are decreasing at 3 sec. On the other hand, that of electron is still increasing. From this, it is speculated that it will take a lot of time for electron to reach the steady state than the other species.

6.2 Case with momentum dependence of D_ρ

As same as the case without momentum dependence of D_ρ, the propargation of ICRF wave electric field calculated by TASK/WM is used to the calculation of quasi-linear diffusion term in TASK/FP. The ICRF wave propargation is shown in Fig. 5.3. And then the initial power sbsroption profile of ECH, ICRF, NBI, and fast α particle generated by fusion reaction are shown in Fig. 5.4. The absorption power of NBI, ICRF, and ECH are constant in time and the values have same value that of previous section.

6.2.1 At 3 second after the onset of heatings

The simulation is done for 3 second with the several heatings. Figs. 6.10 and 6.11 show the contour of the heated momentum distribution function for each species at four radial points. There are large differences among Figs. 6.2-(c), 6.11-(c) for the momentum distribution function of triton. Compared with the case without momentum dependence of D_ρ, it is found that the fast tritons are less around plasma edge. This is because the fast triton generated by the fusion reaction and cyclotron acceleration aroud plasma core is less transfered due to the momentum dependence of D_ρ.

Figs. 6.12 show the radial pprofile of two kind of temperatures, averaged energy temperature and bulk temperature, at 3 second. Compared with the Figs. 6.3, the temperature of electron and ions become high temperature because the fast ions which

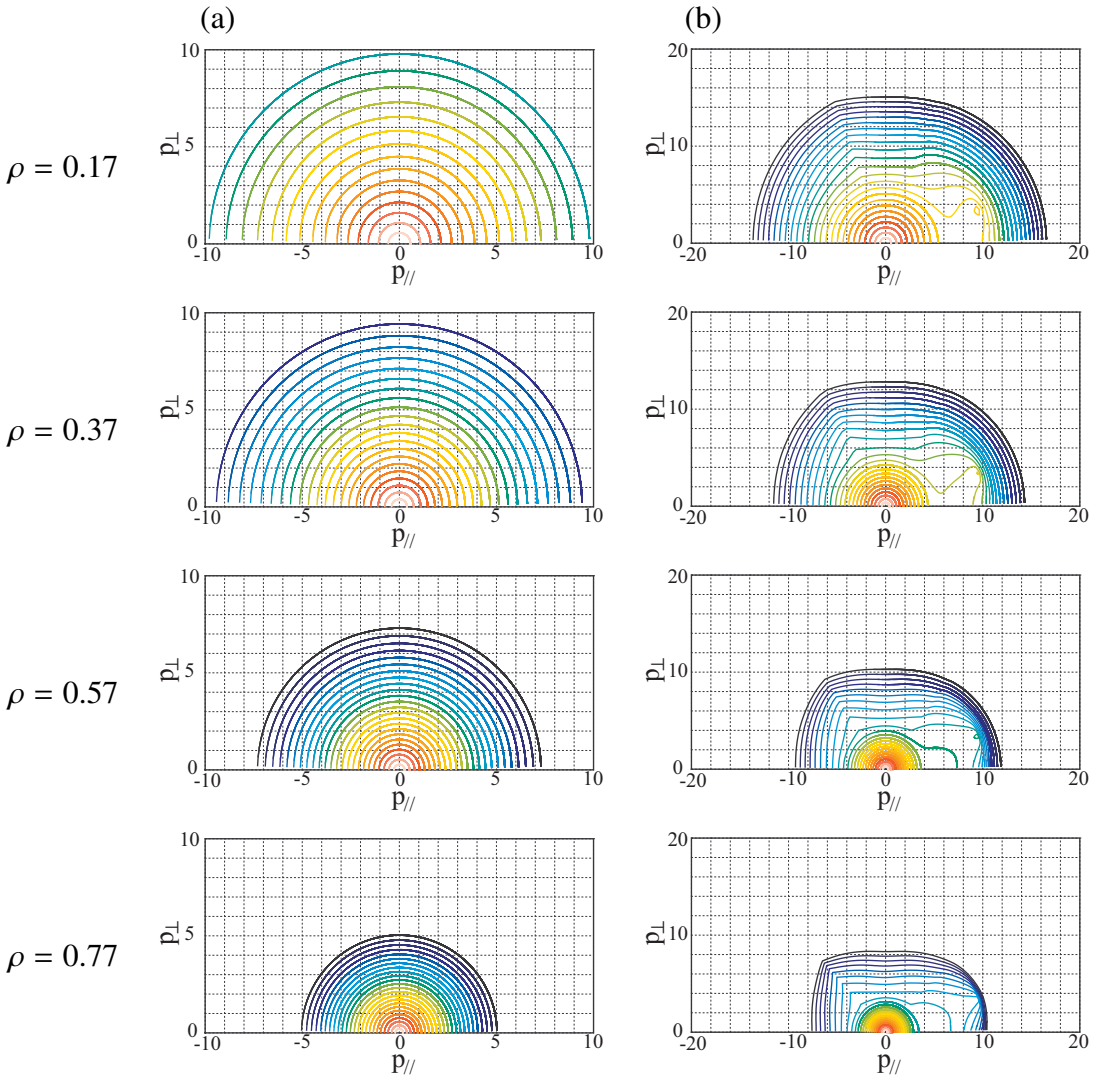

Figure 6.10: The contour of the momentum distribution functions of electron and deuteron in 2D momentum space at several radial points are shown. The radial point $\rho = 0.17$ is consistent to the point of the ICRF wave absorption peak for triton.

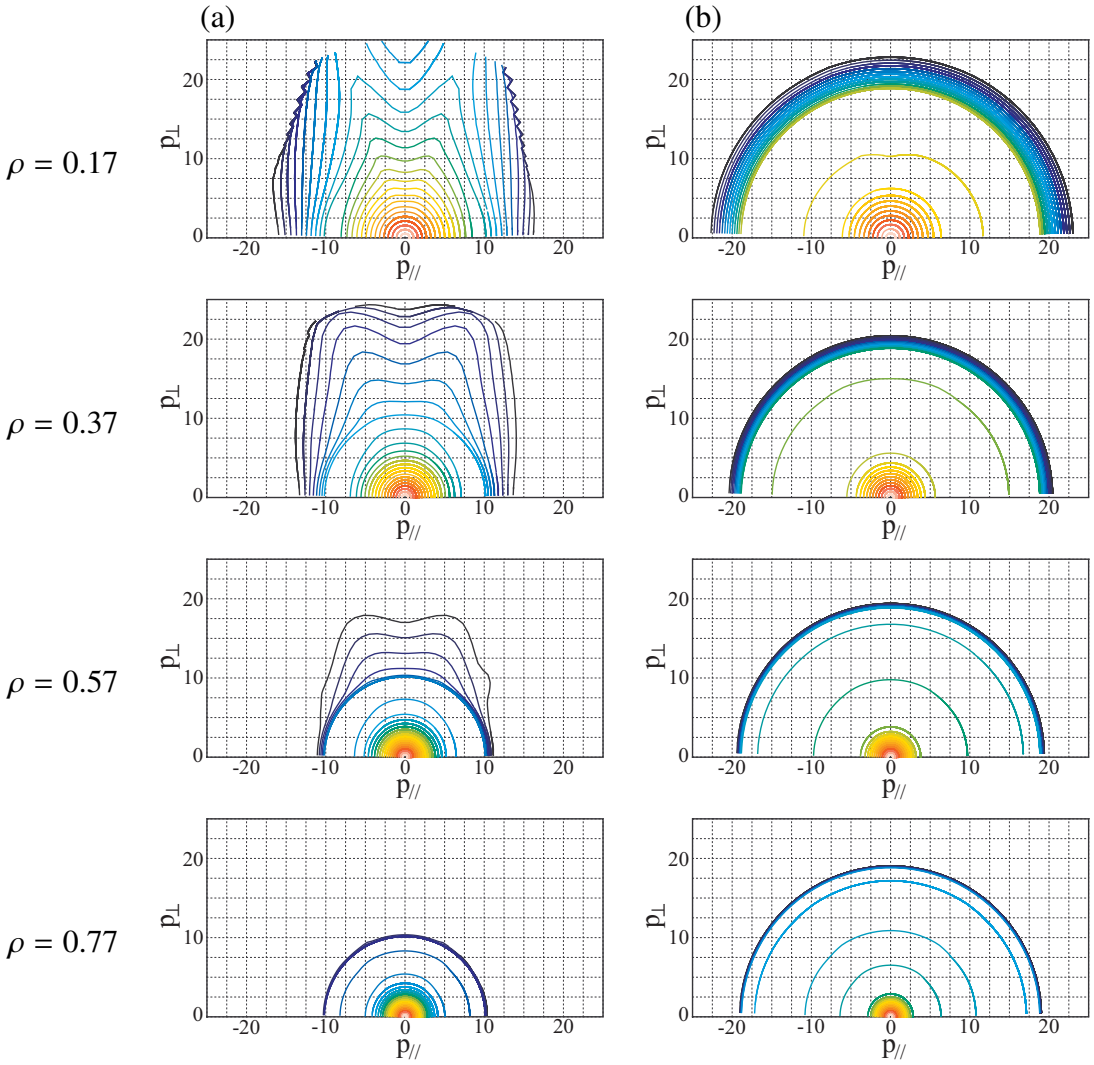

Figure 6.11: The contour of the momentum distribution functions of triton and helium ion in 2D momentum space at several radial points are shown.

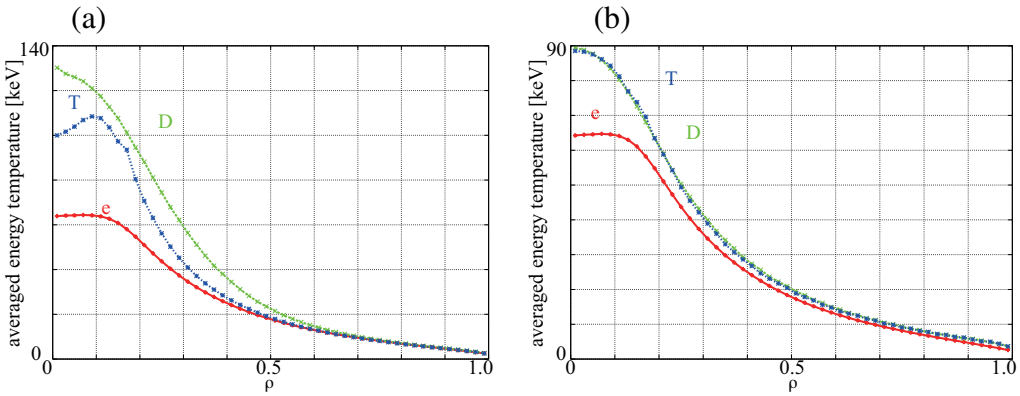

Figure 6.12: (a) The averaged energy temperature and (b) the bulk temperature for each species at 3 sec are shown.

are not thermalized stay around the plasma core. With the same reason, the peak of the temperature profiles become narrow compared with Fig. 6.3.

Chapter 7

Conclusion

Throughout our research presented in this thesis, we have devoted to two aspects; one is to develop the kinetic transport code TASK/FP, which is a component of integrated code TASK, and the other is to analyze the plasma heating with ITER like parameters by the use of TASK/FP.

Formulation

In Chapter 3, the fundamental equation which describes the time evolution of the momentum distribution function was formulated.

Reduction of the phase space variables In general, the momentum distribution function has seven variables, three momentum variables $\boldsymbol{p}$, three spatial variables $\boldsymbol{r}$, and time t. In our kinetic transport code TASK/FP, the number of variables of the momentum distribution function is reduced to four, the momentum parallel to the magnetic field line $p_{\parallel}$, the momentum perpendicular to the magnetic field line $p_{\perp}$, normalized minor radius ρ, and time t by using the assumption of azimuthal symmetry in momentum space, that of toroidal symmetry in real space and the bounce average.

Relativistic effect Since our kinetic transport code simulates the transport in high temperature fusion plasmas, the relativistic effect was included in the formulation. The relativistic effects appear not only as a momentum distribution function but also in several terms such as, the Coulomb collision term, the quasi-linear term, and the fusion reaction rate. Thus they were also included in the formulation.

Collision term In a fusion plasma with auxiliary heating, the momentum distribution function of background plasma often deviates from the Maxwellian distribution function. In order to include the non-Maxwellian effect into the Coulomb collision term, the collision term is described by the non-linear collision model [20, 40]. Owing to the use of the non-linear collision term, the density, the momentum, and the energy of the plasma are conserved through the collision. In the calculation of the non-linear collision term, the integration whose integrand include the non-Maxwellian background

momentum distribution function can not be calculated analytically, but should be calculated numerically. Since the numerical calculation requires a lot of computational resources, the requirement was reduced by using the Legendre expansion.

Radial transport In TASK/FP, the one-dimensional radial transport term was implemented. The transport model was formulated in order to describe the turbulence transport due to microscopic instabilities. In order to include the finite gyro radius effect on energetic ions, the momentum dependence of the radial transport coefficient is included in the model.

Fusion reaction rate The fusion reaction rate is given by the double integration of the background and incident momentum distribution functions. In the conventional calculation of the fusion reaction rate, however, both of the momentum distribution functions are assumed to be Maxwellian. In order to include the effect of fast ions, we numerically integrate the non-Maxwellian momentum distribution function. Since the momentum space retains only two variables, in our numerical code $p_{\parallel}$ and $p_{\perp}$, the gyro-phase average is used to calculate the relative velocity.

Bounce average Since the magnetic field is non-uniform in tokamak plasma, the poloidal angle dependence appears in the momentum distribution function. Therefore, the Fokker-Planck equation should be averaged over the poloidal motion of the particles. In the non-uniform magnetic field, there are two kind of guiding center orbits, passing and trapped. The orbit of the trapped particle guiding center does not circulate around the magnetic axis, but bounce on the magnetic surface. In TASK/FP, the Fokker-Planck equation is bounce averaged using the method derived by Killeen *et al.* [49].

Coding

In the latter half of Chapter 3, the numerical scheme of our code is described.

Numerical grid and differencing We use a finite computational domain in three dimensional phase space for the calculation of the Fokker-Planck equation. The equation formulated in the above is discretized in the three phase space variables. The full implicit method is adopted for the scheme of the time advancing.

Multi-species In general, the fusion plasma consist of several particle species. Therefore, it is required that time evolution of the momentum distribution function of each species should be calculated simultaneously.

Parallel computing Although the variables of the momentum distribution function are reduced to four, the required amount of computation for long time simulation is still huge. In order to solve the matrix equation for large-size asymmetric coefficient

matrix as fast as possible, we parallelized our code by using the parallel computing library, PETSc [51]. By this implementation, we achieved a considerable reduction of the computation time.

Verification

In Chapter 4, the properties of the Coulomb collision term, DC electric field term, quasi-linear diffusion term, and source term were numerically examined. The benchmark test of the Coulomb collision term and DC electric field term was done for the electrical conductivity. The confirmation of the properties of the quasi-linear term and the effect of the non-uniform magnetic field effect is given by the deformed distribution function. The influence of the existence of fast ions to the reaction rate was also confirmed.

Simulation of multi-species heating without radial transport

In Chapter 5, the analysis of multi-species plasma heating was done by using TASK/FP. The plasma which consists of four species, electron, deuteron, triton, and α particle is considered and the time evolution of their momentum distribution functions were calculated. The ECRF, ICRF, NBI, and fusion reactions (D–D, D–T, T–T) were included as heat sources.

From the results of the calculation without radial transport, it was found that the heating mechanism which is different for each species was described. The triton is accelerated by the second cyclotron harmonics of ICRF in addition to the strong acceleration of fast triton generated by D–D reaction. The momentum distribution function of deuteron injected 1 MeV NB was relaxed through the slowing down due to the collision with electron and pitch angle scattering due to the collision with ions. The fast α particles generated by D-T and T–T reactions is isotropic and slowed down owing to the collision mainly with electron. The electron was accelerated by ICRF and ECRF and heated by collision with fast ions. Because of the fast collisional relaxation of electron, however, the momentum distribution function of electron was only weakly deformed.

Simulation of multi-species heating with radial transport

In Chapter 6, the analysis of multi-species plasma heating with radial transport was carried out by the use of TASK/FP. In the presence of radial transport, the fast ions generated in the central part of the plasma diffuse to the plasma edge, and the heating profile becomes broad. In the case of radial transport with the momentum dependence $D_\rho \propto 1/\sqrt{1 + p^2/p_{th}^2}$, the fast ions less diffuse. Therefore, the heating profile becomes narrower compared with the case without momentum dependence.

Future perspective

There are several improvements required for comprehensive kinetic analysis of heating processes in fusion plasmas. TASK/FP should include the finite gyro radius effect, more

realistic turbulence transport model and the coupling with radial and toroidal electric field. Additionally, the coupling with full wave analysis code TASK/WM is required for the self-consistent wave heating analysis. Moreover, the validation of our code through the comparison with the experimental observation is necessary. With these improvements, the integrated simulation code will be available for the prediction of the plasma performance, the planning of operation scenario, and the development of plasma control.

Acknowledgement

My heartfelt appreciation goes to Prof. Fukuyama whose comments, suggestions, and encouragement were of inestimable value for my study. I am also indebt to Associate Prof. Murakami for his comments and enormous contribution to my work. I would also like to express my gratitude to all members of our laboratory, especially, Dr. Honda, Dr. Kawamura, Dr. Wakasa, and Dr. Raburn for their help and support.

This work was supported in part by the Grant-in-Aid for scientific research, No. 20226017, from Japan Society for the Promotion of Science.

Finally, I would also like to express my gratitude to my family for their moral support and warm encouragement.

Bibliography

[1] J. Huba: *"NRL PLASMA FORMULARY"* (The Office of Naval Research, Washington, DC, 2007).

[2] J. Wesson: *"Tokamaks 3rd Edition"* (Oxford University Press, 1987).

[3] Y. Shimomura, R. Aymar, V. Chuyanov, et al.: Nuclear Fusion **39** (1999) 1295.

[4] Fusion Reactor System Laboratory. "Concept Stugy of the Steady State Tokamak Reactor". JAERI-M 91-081, 1991.

[5] S. Iio: Journal of Plasma and Fusion Research **74** (1998) 685. in Japanese.

[6] J. Reader, I. Cook, et al. "Safety and Enviromental Assessment of Fusion Power (SEAFP)". EURFUBRU XII-217/95, European Commission Directorate General XII Fusion Program Brussels, 1995.

[7] D. Dombrowski: Fusion Eng. Des. **37** (1997) 229.

[8] T. Muroga: Journal of Plasma and Fusion Research **85** (2009) 260. in Japanese.

[9] S. Nishio, K. Tobita, K. Ushigusa, et al.: Journal of Plasma and Fusion Research **78** (2002) 1219.

[10] K. Tobita, S. Nishio, M. Sato, et al. "Concept of compact low aspect ratio DEMO reactor, SlimCS". Proc. of 21th IAEA Fusion Energy Conf., Chengdu, 2006. FT/P5-22.

[11] H. Hondo, Y. Uchiyama, Y. Morizumi. "Evaluation of Power Generation Technologies based on Life Cycle CO2 Emissions - Re-estimation using the Latest Data and Effects of the Difference of Conditions -". Socio-economic Research Center. Reo. No. Y99009, 2000. in Japanese.

[12] H. Hondo. "Evaluation of nuclear power generation technologies based on life cycle CO2 emissions". Socio-economic Research Center. Reo. No. Y01006, 2001. in Japanese.

[13] S. Uemura, K. Yamazaki, H. Arimoto, et al.: Transactions of the Atomic Energy Society of Japan **8** (2009) 34. in Japanese.

[14] S. Maruyama, T. Mizoguchi: Journal of Plasma Fusion Research **78** (2002).

[15] T. Imai: Journal of Plasma Fusion Research **81** (2005) 178. in Japanese.

[16] M. Kuriyama, N. Akino, M. Araki, et al.: Fusion Engineering and Design **26** (1995) 445.

[17] T. Stix: Nuclear Fusion **15** (1975) 737.

[18] D. Blackfield, J. Scharer: Nuclear Fusion **22** (1982) 255.

[19] M. McCoy, A. MIRIN, J. Killeen: Computer Physics Communication **24** (1981) 37.

[20] C. Karney: Computer Physics Reports **4** (1986) 183.

[21] G. Kerbel, M. McCoy: Phys. Fluid **28** (1985) 3629.

[22] A. Fukuyama, T. Ueeda. Proc. 17th Euro. Conf. Amsterdam, 1990. IAEA-CSP-25/CD/TH/P2-3.

[23] J. McKenzie, M. O'Brien, M. Cox: Computer Physics Communications **66** (1991) 194.

[24] G. Giruzzi, I. Findone, X. Garbet: Nuclear Fusion **32** (1992) 1011.

[25] R. Harvey, M. McCoy. Proceedings of the IAEA Technical Committee Meeting on Simulation and Modeling of Thermonuclear Plasmas, Montreal, Canada, 1992. (USDOC NTIS Document No. DE93002962).

[26] R. Harvey, M. McCoy. "The CQL3D Fokker-Planck Code". `http://www.compxco.com/cql3d.html`, 2005.

[27] A. Fukuyama, et al. Proc. of 20th IAEA FEC (Villamoura, 2004). IAEA-CSP-25/CD/TH/P2-3.

[28] T. Yamamoto, S. Murakami, A. Fukuyama: Plasma and Fusion Research **3** (2008) S1075.

[29] H. Nuga, A. Fukuyama: Plasma and Fusion Research **5** (2010) S2068.

[30] M. Honda, A. Fukuyama: Journal of Computational Physics **227** (2008) 2808.

[31] H. Nuga, A. Fukuyama: Journal of Plasma and Fusion Research **8** (2009) 1125.

[32] S. R. de Groot, W. A. van Leeuwen, C. G. van Weert: *"Relativistic kinetic theory: principles and applications"* (North-Holland, 1980).

[33] K. Nakashima, T. Cowan: Journal of Plasma and Fusion Research **78** (2002) 568. (in Japanese).

[34] L. Landau: Phys. Z. Sowjet. **10** (1936) 154.

[35] M. Rosenbluth, W. MacDonald, D. Judd: Phys. Rev. **107** (1957) 1.

[36] B. A. Trubnikov: Sov. Phys.-JETP **7** (1958) 926.

[37] B. A. Trubnikov: in*Reviews of Plasma Physics*, ed. M. A. Leontovich (Consultants Bureau, New York, 1965), Vol. 1, p. 174.

[38] S. Beliaev, G. Budker: Sov. Phys.-Dokl. **1** (1956) 218.

[39] B. Braams, C. Karney: Physical Review Letters **59** (1987) 1817.

[40] B. Braams, C. Karney: Phys. Fluid B **1** (1989) 1355.

[41] C. F. F. Karney, N. J. Fisch: Phys. Fluids **28** (1985) 116.

[42] A. A. Vedenov, E. P. Velikhov, R. Z. Sagdeev: Nuclear Fusion **1** (1961).

[43] W. E. Drummond, D. Pines: Nucl. Fusion Soc Suppl. **3** (1962) 1049.

[44] C. Kennel, F. Engelmann: Phys. Fluids **9** (1966) 2377.

[45] H. Nuga, A. Fukuyama: Progress in Nuclear Science and Technology accepted.

[46] S. Ichimaru: *"Basic principles of plasma physics: a statistical approach"* (Westview Press, 1973).

[47] B. H. Duane. "Fusion Cross Section Theory". Brookhaven National Laboratory, Rept. BNWL-1685, 1972.

[48] G. H. Miley, H. Towner, N. Ivich. "Fusion Cross Section and Reactivities". Rept. COO-2218-17, University of Illinois, Urbana, IL, 1974.

[49] J. Killeen, G. Kerbel, M. McCoy, et al.: *"Computational Methods for Kinetic Models of Magnetically Confined Plasmas"* (Springer-Verlag, 1986).

[50] J. S. Chang, G. Cooper: Journal of Computational Physics **6** (1970) 1.

[51] S. Balay, K. Buschelman, V. Eijkhout, et al. "PETSc Users Manual". http://www.mcs.anl.gov/petsc/petsc-as/snapshots/petsc-3.0.0/docs/manual.pdf, December 2008.

Appendix A

Derivations related with first kind Legendre function in collision term

A.1 Derivation of the derivatives of Rosenbluth potentials in non-relativistic collision operator

The derivative of the Legendre harmonics, $P_l(\mu)$ ($\mu = \cos\theta$), are derived in this section. The derivative of the Legendre harmonics is given by the following reccurence equation:

$$(\mu^2 - 1)\frac{\partial}{\partial\mu}P_l(\mu) = l\mu P_l(\mu) - lP_{l-1}(\mu). \tag{A.1}$$

Similarly, the derivative of the second order of $P_l(\mu)$ is given by the reccurence equation:

$$\frac{\partial^2 P_l(\mu)}{\partial\mu^2} = \frac{1}{\sin^2\theta}\left\{2\mu\frac{\partial P_l(\mu)}{\partial\mu} - l(l+1)P_l(\mu)\right\}. \tag{A.2}$$

From these equations, we obtain:

$$\frac{\partial P_l(\mu)}{\partial\theta} = \frac{1}{\sin\theta}\left\{\mu P_l(\mu) - P_{l-1}(\mu)\right\} \tag{A.3}$$

$$\frac{\partial^2 P_l(\mu)}{\partial\theta^2} = -\left(\frac{l}{\sin^2\theta} + l^2\right)P_l(\mu) + \frac{l\cos\theta}{\sin^2\theta}P_{l-1}(\mu). \tag{A.4}$$

A.2 The calculation of the functions $j_{l[k]*}$ and $y_{l[k]*}$ in Sec. 3.4.2

As shown in eq. (3.115), the functions $j_{l[1]a}$ and $y_{l[1]a}$ are expressed in terms of first kind Legendre function, $P^l_a(\gamma)$.

$$\begin{aligned} j_{l[1]a}(u/c) &= \sqrt{\pi c/2u}P^{-l-1/2}_{a-1/2}(\gamma) \\ y_{l[1]a}(u/c) &= (-1)^{-l-1}\sqrt{\pi c/2u}P^{l+1/2}_{a-1/2}(\gamma). \end{aligned} \tag{3.115}$$

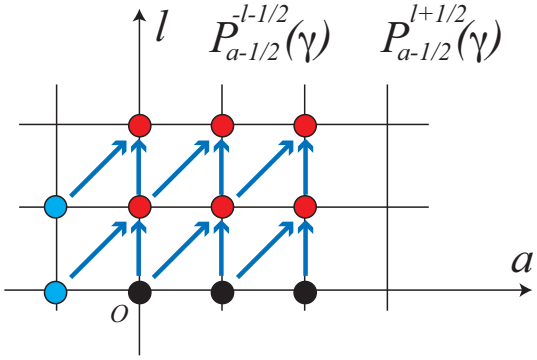

Figure A.1: The image figure which shows the method in order to obtain $P^{-l-1/2}_{a-1/2}(\gamma)$ and $P^{l+1/2}_{a-1/2}(\gamma)$ for $1 \leq l$ is shown. The black circles denote the expressions of eqs. (A.8) or (A.9). The red circles are obtained by the two below circles. The blue circles are given by the relation $P^{\mu}_{\nu}(\gamma) = P^{\mu}_{-\nu-1}(\gamma)$.

The first kind Legendre function which is needed for the calculation of the functions, $j_{l[1]a}$ and $y_{l[1]a}$, is given by the reccurence equation;

$$P^{\mu}_{\nu-1}(\gamma) - \gamma P^{\mu}_{\nu}(\gamma) + (\nu - \mu + 1)\sqrt{\gamma^2 - 1} P^{\mu-1}_{\nu}(\gamma) = 0. \tag{A.5}$$

We can rewrite the equation by the replacements of $\mu = -l - 1/2$ and $\nu = a - 1/2$;

$$P^{-(l+1)-1/2}_{a-1/2}(\gamma) = \frac{1}{(a + l + 1)\sqrt{\gamma^2 - 1}} \left(\gamma P^{-l-1/2}_{a-1/2}(\gamma) - P^{-l-1/2}_{a-3/2}(\gamma)\right). \tag{A.6}$$

Similarly, the equation can be rewritten into;

$$P^{(l+1)+1/2}_{a-1/2}(\gamma) = \frac{1}{\sqrt{\gamma^2 - 1}} \left\{(a - l - 1)\gamma P^{l+1/2}_{a-1/2}(\gamma) - (a + l) P^{l+1/2}_{a-3/2}(\gamma)\right\}. \tag{A.7}$$

As shown in Fig. A.1, we can obtain the every expression of $j_{l[1]a}$ and $y_{l[1]a}$ for $0 < a < 2$ by using eqs. (A.6) and (A.7) and the following equations:

$$\begin{aligned} P^{-1/2}_{-1/2}(\gamma) &= \sqrt{\frac{2}{\pi z}}\sigma \\ P^{-1/2}_{1/2}(\gamma) &= \sqrt{\frac{2z}{\pi}} = P^{-1/2}_{-3/2}(\gamma) \\ P^{-1/2}_{3/2}(\gamma) &= \sqrt{\frac{2z}{\pi}}\gamma \end{aligned} \tag{A.8}$$

$$\begin{aligned} P^{1/2}_{-1/2}(\gamma) &= \sqrt{\frac{2}{\pi z}} \\ P^{1/2}_{1/2}(\gamma) &= \sqrt{\frac{2}{\pi z}}\gamma = P^{1/2}_{-3/2}(\gamma) \\ P^{1/2}_{3/2}(\gamma) &= \left(\frac{1}{z} + 2z\right)\sqrt{\frac{2z}{\pi}}, \end{aligned} \tag{A.9}$$

where $z = u/c$ and

$$\sigma = \sinh^{-1} z = \ln\left(z + \sqrt{1+z^2}\right). \tag{A.10}$$

In order to obtain the relativistic non-linear collision coefficients to the order of $l = 2$, from eqs. (3.121), the functions $j_{l[1]a}$ and $y_{l[1]a}$ are required to the order of $l = 4$. Therefore we catalog all the required functions $j_{l[1]a}$ and $y_{l[1]a}$ for $0 \le l \le 4$:

$$\begin{aligned} j_{0[1]0} &= \frac{\sigma}{z}\,, & y_{0[1]0} &= -\frac{1}{z} \\ j_{0[1]1} &= 1\,, & y_{0[1]1} &= -\frac{\gamma}{z} \\ j_{0[1]2} &= \gamma\,, & y_{0[1]2} &= -\frac{1+2z^2}{z} \end{aligned} \tag{A.11}$$

$$\begin{aligned} j_{1[1]0} &= \frac{\gamma\sigma - z}{z^2}\,, & y_{1[1]0} &= -\frac{\gamma}{z^2} \\ j_{1[1]1} &= \frac{z\gamma - \sigma}{2z^2}\,, & y_{1[1]1} &= -\frac{1}{z^2} \\ j_{1[1]2} &= \frac{z}{3}\,, & y_{1[1]2} &= -\frac{(1-2z^2)\gamma}{z^2} \end{aligned} \tag{A.12}$$

$$\begin{aligned} j_{2[1]0} &= \frac{1}{4z^3}\left\{(2\gamma^2+1)\sigma - 3\gamma z\right\}, & y_{2[1]0} &= -\frac{1}{z^3}(1+2\gamma^2) \\ j_{2[1]1} &= \frac{1}{6z^3}\left\{(\gamma^2+2)z - 3\gamma\sigma\right\}, & y_{2[1]1} &= -\frac{3}{z^3}\gamma \\ j_{2[1]2} &= \frac{1}{24z^3}\left(2\gamma z^3 - 3\gamma z + 3\sigma\right), & y_{2[1]2} &= -\frac{3}{z^3} \end{aligned} \tag{A.13}$$

$$\begin{aligned} j_{3[1]0} &= \frac{1}{36z^4}\left\{(6\gamma^2+9)\gamma\sigma - (11\gamma^2+4)z\right\}, & y_{3[1]0} &= -\frac{3\gamma}{z^4}(3+2\gamma^2) \\ j_{3[1]1} &= \frac{1}{48z^4}\left\{(2\gamma^2+13)\gamma z - 3(4\gamma^2+1)\sigma\right\}, & y_{3[1]1} &= -\frac{3}{z^4}(1+4\gamma^2) \\ j_{3[1]2} &= \frac{1}{120z^4}\left\{2\gamma^2 z^3 - (7\gamma^2+8)z + 15\gamma\sigma\right\}, & y_{3[1]2} &= -\frac{15\gamma}{z^4} \end{aligned} \tag{A.14}$$

$$\begin{aligned} j_{4[1]0} &= \frac{1}{576z^5}\left\{(24\gamma^4+72\gamma^2+9)\sigma - (50\gamma^2+55)\gamma z\right\}, & y_{4[1]0} &= -\frac{3}{z^5}(8\gamma^4+24\gamma^2+3) \\ j_{4[1]1} &= \frac{1}{720z^5}\left\{(6\gamma^4+83\gamma^2+16)z - (60\gamma^2+45)\gamma\sigma\right\}, & y_{4[1]1} &= -\frac{15\gamma}{z^5}(4\gamma^2+3) \\ j_{4[1]2} &= \frac{1}{1440z^5}\left\{(4\gamma^2 z^2 - 24\gamma^2 - 81)\gamma z + (90\gamma^2+15)\sigma\right\}, & y_{4[1]2} &= -\frac{15}{z^5}(6\gamma^2+1). \end{aligned} \tag{A.15}$$

A.2.1 The case with small z

In the numerical code, the numerical instability occurs with the value of $j_{l[1]a}$ ($l \geq 2$) for small z. Therefore, in order to avoid the trouble, σ and γ should be expanded in terms of infinitesimal z:

$$\begin{aligned}\sigma &\sim z - \frac{1}{6}z^3 + \frac{3}{40}z^5 - \frac{5}{112}z^7 + \frac{35}{1152}z^9 \\ \gamma &\sim 1 + \frac{1}{2}z^2 - \frac{1}{8}z^4 + \frac{1}{16}z^6 - \frac{5}{128}z^8.\end{aligned} \tag{A.16}$$

In TASK/FP, the both approximation is applied for the range of the value $z < 10^{-2}$, and the approximation of σ is only applied for the range of the value $10^{-2} < z < 10^{-1}$. With the both of approximation, the expressions of $j_{l[1]a}$ are given by:

$$j_{2[1]0} \sim \frac{1}{4}\left\{\frac{4}{15}z^2 - \left(\frac{15}{112} + \frac{3}{80}\right)z^4\right\} \tag{A.17}$$

$$j_{2[1]1} \sim \frac{1}{6}\left(\frac{3}{12}z^2 - \frac{29}{80}z^4\right) \tag{A.18}$$

$$j_{2[1]2} \sim \frac{1}{24}\left(\frac{8}{5}z^2 - \frac{4}{7}z^4\right) \tag{A.19}$$

$$j_{3[1]0} \sim \frac{1}{36}\left(\frac{81}{80} - \frac{75}{112}\right)z^3 \tag{A.20}$$

$$j_{3[1]1} \sim \frac{1}{48}\left\{\left(\frac{11}{16} - \frac{9}{10} + \frac{75}{112}\right)z^3 + \left(\frac{1}{8} + \frac{15}{28}\right)z^5\right\} \tag{A.21}$$

$$j_{3[1]2} \sim \frac{15}{120}\left\{\left(\frac{29}{240} - \frac{5}{112}\right)z^3 - \left(\frac{11}{336} + \frac{3}{320}\right)z^5\right\} \tag{A.22}$$

$$j_{4[1]0} \sim \frac{1}{576}\left(\frac{125}{128} + \frac{3675}{1152} - \frac{249}{70}\right)z^4 \tag{A.23}$$

$$j_{4[1]1} \sim \frac{1}{720}\left(-105 \times \left(\frac{35}{1152} - \frac{5}{224} - \frac{3}{320} - \frac{1}{96} - \frac{5}{128}\right) - \frac{480}{105}\right)z^4 \tag{A.24}$$

$$j_{4[1]2} \sim \frac{1}{1440}\left(\frac{301}{128} + \frac{3675}{1152} - \frac{225}{56}\right)z^4 \tag{A.25}$$

Appendix B

Matrix formulation

As shown in Sec. 3.10.3, the Fokker-Planck equation is given by:

$$\frac{\partial \boldsymbol{f}_s}{\partial t} = \overleftrightarrow{\boldsymbol{A}}_s \cdot \boldsymbol{f}_s + \boldsymbol{H}_s, \tag{B.1}$$

for species s. Moreover, the bounce averaged Fokker-Planck equation is also given by:

$$\frac{\partial \lambda \boldsymbol{f}_s}{\partial t} = \overleftrightarrow{\boldsymbol{A}}_{0s} \cdot \boldsymbol{f}_s + \lambda \langle \boldsymbol{H}_s \rangle, \tag{B.2}$$

where λ and $\overleftrightarrow{\boldsymbol{A}}_0$ denote bounce averaged parameter defined at Sec. 3.8 and the bounce averaged coefficient matrix. In this section, the formulation of coefficient matrix $\overleftrightarrow{\boldsymbol{A}}$ is discussed.

B.1 Discretization

From here, we discuss the bounce averaged Fokker-Planck equation. As shown in Sec. 3.8, eq. (B.2) can be rewritten as:

$$\begin{aligned}\frac{\partial \lambda f}{\partial t} &= \overleftrightarrow{\boldsymbol{A}}_0 \boldsymbol{f} + \lambda \langle H \rangle \\ &= -\frac{1}{p_0^2}\frac{\partial}{\partial p_0} p_0^2 S_{p0} - \frac{1}{p_0 \sin\theta_0}\frac{\partial}{\partial \theta_0}\sin\theta_0 S_{\theta 0} - \frac{1}{\rho_0}\frac{\partial}{\partial \rho_0}\rho_0 S_{\rho 0} + \lambda \langle H \rangle ,\end{aligned} \tag{B.3}$$

where S_{p0}, $S_{\theta 0}$ and $S_{\rho 0}$ are the bounce averaged flux

$$S_{p0} = -D_{pp0}\frac{\partial f}{\partial p_0} - D_{p\theta 0}\frac{1}{p_0}\frac{\partial f}{\partial \theta_0} + F_{p0} f \tag{B.4}$$

$$S_{\theta 0} = -D_{\theta p0}\frac{\partial f}{\partial p_0} - D_{\theta\theta 0}\frac{1}{p_0}\frac{\partial f}{\partial \theta_0} + F_{\theta 0} f \tag{B.5}$$

$$S_{\rho 0} = -D_{\rho 0}\frac{\partial f}{\partial \rho} + F_{\rho 0} f. \tag{B.6}$$

In the following, the subscript 0 whcih is the label of the bounce average is omitted for simplicity.

$\overleftrightarrow{\boldsymbol{A}} \cdot \boldsymbol{f}$ is discretized around the neighbor of the grid point (NR, NTH, NR) = (i, j, k) as:

$$
\begin{aligned}
(Af)_{i+1/2,j+1/2,k+1/2} = & \frac{1}{p^2\Delta p}\left(S_{p(i+1,j+1/2,k+1/2)} - S_{p(i,j+1/2,k+1/2)}\right) \\
& + \frac{1}{p\sin\theta\Delta\theta}\left(S_{\theta(i+1/2+j+1,k+1/2)} - S_{\theta(i+1/2,j,k+1/2)}\right) \\
& + \frac{1}{\rho\Delta\rho}\left(S_{\rho(i+1/2,j+1/2,k+1)} - S_{\rho(i+1/2,j+1/2,k)}\right). \qquad \text{(B.7)}
\end{aligned}
$$

The fluxes are given by:

$$
\begin{aligned}
S_{p(1,1/2,1/2)} = & D_{pp}\frac{f_{3/2,1/2,1/2} - f_{1/2,1/2,1/2}}{\Delta p} \\
& + D_{p\theta}\frac{[\varepsilon_{(1,3/2,1/2)}f_{(3/2,3/2,1/2)} + \delta_{(1,3/2,1/2)}f_{(1/2,3/2,1/2)}] - [\varepsilon_{(1,-1/2,1/2)}f_{(3/2,-1/2,1/2)} + \delta_{(1,-1/2,1/2)}f_{(1/2,-1/2,1/2)}]}{2\Delta\theta} \\
& - F_p[\varepsilon_{(1,1/2,1/2)}f_{(3/2,1/2,1/2)} + \delta_{(1,1/2,1/2)}f_{(1/2,1/2,1/2)}] \qquad \text{(B.8)}
\end{aligned}
$$

where $1 - \delta = \varepsilon$ and the subscript $(i + a, j + b, k + c)$ is reduced to (a, b, c). Moreover, the grid point of diffusion and friction coefficients in RHS is same with that of flux in LHS. Thus the notation of the grid point of D and F in RHS are reduced. Similarly,

$$
\begin{aligned}
S_{p(0,1/2,1/2)} = & D_{pp}\frac{f_{1/2,1/2,1/2} - f_{-1/2,1/2,1/2}}{\Delta p} \\
& + D_{p\theta}\frac{[\varepsilon_{(0,3/2,1/2)}f_{(1/2,3/2,1/2)} + \delta_{(0,3/2,1/2)}f_{(-1/2,3/2,1/2)}] - [\varepsilon_{(0,-1/2,1/2)}f_{(1/2,-1/2,1/2)} + \delta_{(0,-1/2,1/2)}f_{(-1/2,-1/2,1/2)}]}{2\Delta\theta} \\
& - F_p[\varepsilon_{(0,1/2,1/2)}f_{(1/2,1/2,1/2)} + \delta_{(0,1/2,1/2)}f_{(-1/2,1/2,1/2)}] \qquad \text{(B.9)}
\end{aligned}
$$

$$
\begin{aligned}
S_{\theta(1/2,1,1/2)} = & \\
& D_{\theta p}\frac{[\varepsilon_{(3/2,1,1/2)}f_{3/2,3/2,1/2} + \delta_{(3/2,1,1/2)}f_{3/2,1/2,1/2}] - [\varepsilon_{(-1/2,1,1/2)}f_{-1/2,3/2,1/2} + \delta_{(-1/2,1,1/2)}f_{-1/2,1/2,1/2}]}{2\Delta p} \\
& + D_{\theta\theta}\frac{f_{1/2,3/2,1/2} - f_{1/2,1/2,1/2}}{\Delta\theta} - F_\theta[\varepsilon_{(1/2,1,1/2)}f_{1/2,3/2,1/2} + \delta_{(1/2,1,1/2)}f_{(1/2,1/2,1/2)}] \qquad \text{(B.10)}
\end{aligned}
$$

$$
\begin{aligned}
S_{\theta(1/2,0,1/2)} = & \\
& D_{\theta p}\frac{[\varepsilon_{(3/2,0,1/2)}f_{3/2,1/2,1/2} + \delta_{(3/2,0,1/2)}f_{3/2,-1/2,1/2}] - [\varepsilon_{(-1/2,0,1/2)}f_{-1/2,1/2,1/2} + \delta_{(-1/2,0,1/2)}f_{-1/2,-1/2,1/2}]}{2\Delta p} \\
& + D_{\theta\theta}\frac{f_{1/2,1/2,1/2} - f_{1/2,-1/2,1/2}}{\Delta\theta} - F_\theta[\varepsilon_{(1/2,0,1/2)}f_{1/2,1/2,1/2} + \delta_{(1/2,0,1/2)}f_{(1/2,-1/2,1/2)}] \qquad \text{(B.11)}
\end{aligned}
$$

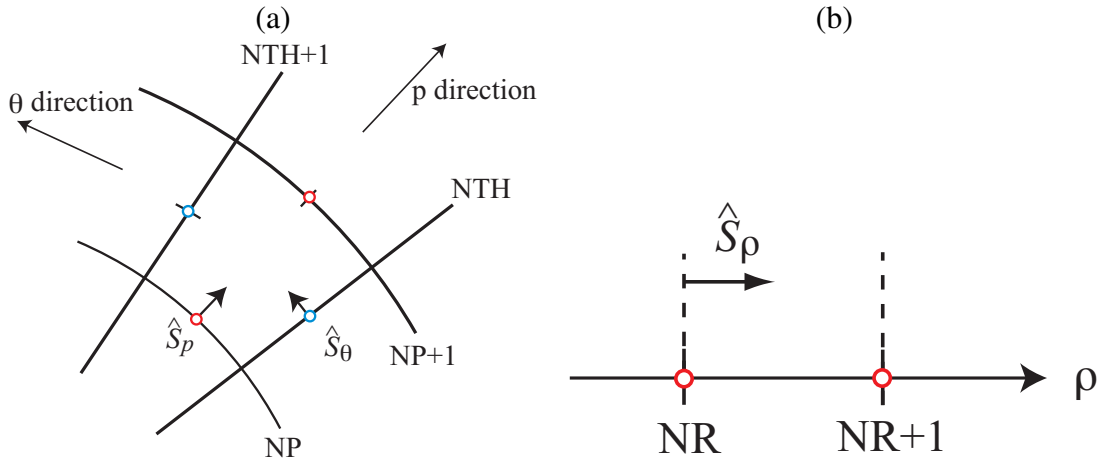

Figure B.1: Numerical grid and grid point of the fluxes, S_p, S_θ, S_ρ are shown.

$$S_{\rho(1/2,1/2,1)} = D_\rho \frac{f_{(1/2,1/2,3/2)} - f_{(1/2,1/2,1/2)}}{\Delta\rho} - F_\rho \left\{ \varepsilon_{(1/2,1/2,1)} f_{(1/2,1/2,3/2)} + \delta_{(1/2,1/2,1)} f_{(1/2,1/2,1/2)} \right\} \tag{B.12}$$

$$S_{\rho(1/2,1/2,0)} = D_\rho \frac{f_{(1/2,1/2,1/2)} - f_{(1/2,1/2,-1/2)}}{\Delta\rho} - F_\rho \left\{ \varepsilon_{(1/2,1/2,0)} f_{(1/2,1/2,1/2)} + \delta_{(1/2,1/2,0)} f_{(1/2,1/2,-1/2)} \right\} \tag{B.13}$$

B.2 New notation

Since the expressions become long, the new notation should be introduced in order to be short the expressions. As shown in fig. B.2 and from eq. (), only the fluxes S_p on the grid point $(NTH, NR) = (j + 1/2, k + 1/2)$ and S_θ on the grid point $(NP, NR) = (i + 1/2, k + 1/2)$ are required for the calculation of $(Af)_{1/2,1/2,,1/2}$. Therefore, the notation $S_{p(i,j+1/2,k+1/2)}$ and $S_{p(i+1,j+1/2,k+1/2)}$ are enabled to reduce S_{p0} and S_{p1}. Similarly, $S_{\theta(i+1/2,j,k+1/2)}$ and $S_{\theta(i+1/2,j+1,k+1/2)}$ can be reduced to $S_{\theta 0}$ and $S_{\theta 1}$, moreover, $S_{\rho(i+1/2,j+1/2,k)}$ and $S_{\rho(i+1/2,j+1/2,k+1)}$ are $S_{\rho 0}$ and $S_{\rho 1}$. The diffusion and friction coefficients also can be reduced by the same method.

Meanwhile, from eq. (B.2) and figs. B.2-(a), (c), 11 momentum distribution functions are required for the calculation of $(Af)_{1/2,1/2,,1/2}$. Each momentum distribution function exists on the half mesh point. The notations of these grid point can be reduced as shown in figs. B.2-(b), (d). By using these new notations, eq. (B.8)~(B.13) can be

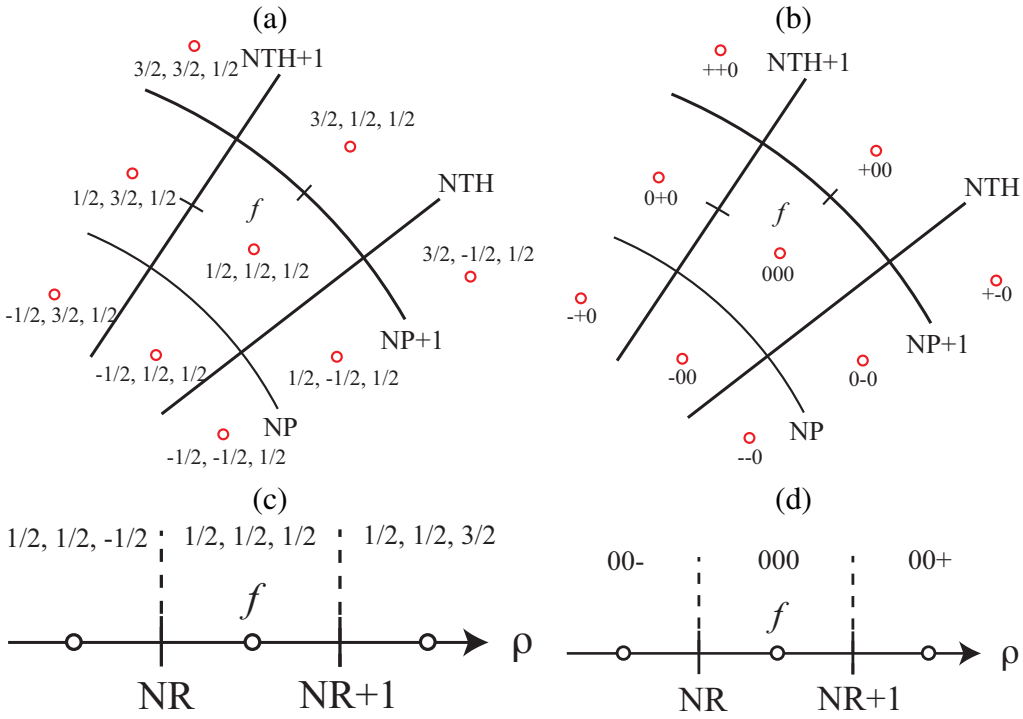

Figure B.2: Numerical grid and grid points of the momentum distribution function around (NP,NTH,NR)= $(i + 1/2, j + 1/2, k + 1/2)$ are shown.

rewritten as:

$$S_{p1} = D_{pp1}\frac{f_{+00} - f_{000}}{\Delta p} + D_{p\theta 1}\frac{[\varepsilon_{(1,\ 3/2,\ 1/2)}f_{++0} + \delta_{(1,\ 3/2,\ 1/2)}f_{0+0}] - [\varepsilon_{(1,\ -1/2,\ 1/2)}f_{+-0} + \delta_{(1,\ -1/2,\ 1/2)}f_{0-0}]}{2\Delta\theta} - F_{p1}[\varepsilon_{(1,\ 1/2,\ 1/2)}f_{+00} + \delta_{(1,\ 1/2,\ 1/2)}f_{000}] \tag{B.14}$$

$$S_{p0} = D_{pp0}\frac{f_{000} - f_{-00}}{\Delta p} + D_{p\theta 0}\frac{[\varepsilon_{(0,\ 3/2,\ 1/2)}f_{0+0} + \delta_{(0,\ 3/2,\ 1/2)}f_{-+0}] - [\varepsilon_{(0,\ -1/2,\ 1/2)}f_{0-0} + \delta_{(0,\ -1/2,\ 1/2)}f_{--0}]}{2\Delta\theta} - F_{p0}[\varepsilon_{(0,\ 1/2,\ 1/2)}f_{000} + \delta_{(0,\ 1/2,\ 1/2)}f_{-00}] \tag{B.15}$$

$$S_{\theta 1} = D_{\theta p1}\frac{[\varepsilon_{(3/2,\ 1,\ 1/2)}f_{++0} + \delta_{(3/2,\ 1,\ 1/2)}f_{+00}] - [\varepsilon_{(-1/2,\ 1,\ 1/2)}f_{-+0} + \delta_{(-1/2,\ 1,\ 1/2)}f_{-00}]}{2\Delta p} + D_{\theta\theta 1}\frac{f_{0+0} - f_{000}}{\Delta\theta} - F_{\theta 1}[\varepsilon_{(1/2,\ 1,\ 1/2)}f_{0+0} + \delta_{(1/2,\ 1,\ 1/2)}f_{(000)}] \tag{B.16}$$

$$S_{\theta 0} = D_{\theta p 0}\frac{[\varepsilon_{(3/2,\ 0,\ 1/2)}f_{+00} + \delta_{(3/2,\ 0,\ 1/2)}f_{+-0}] - [\varepsilon_{(-1/2,\ 0,\ 1/2)}f_{-00} + \delta_{(-1/2,\ 0,\ 1/2)}f_{--0}]}{2\Delta p}$$
$$+D_{\theta\theta 0}\frac{f_{000} - f_{0-0}}{\Delta\theta} - F_{\theta 0}[\varepsilon_{(1/2,\ 0,\ 1/2)}f_{000} + \delta_{(1/2,\ 0,\ 1/2)}f_{(0-0)}] \tag{B.17}$$

$$S_{\rho 1} = D_{\rho 1}\frac{f_{00+} - f_{000}}{\Delta\rho} - F_{\rho 1}\left\{\varepsilon_{(1/2,\ 1/2,\ 1)}f_{00+} + \delta_{(1/2,\ 1/2,\ 1)}f_{000}\right\} \tag{B.18}$$

$$S_{\rho 0} = D_{\rho 0}\frac{f_{000} - f_{00-}}{\Delta\rho} - F_{\rho 0}\left\{\varepsilon_{(1/2,\ 1/2,\ 0)}f_{000} + \delta_{(1/2,\ 1/2,\ 0)}f_{00-}\right\}. \tag{B.19}$$

B.3 Formulation

Using eqs. (B.2)~(B.13), the element of vector, $Af_{(1/2,1/2,1/2)}$, can be described in terms of the momentum distribution function, f_{***}, at the neighbor of the element as:

$$\begin{aligned}
Af_{(1/2,1/2,1/2)} = &\left[\frac{D_{p\theta 1}\varepsilon_{(1,\ 3/2,\ 1/2)}}{2p^2\Delta p\Delta\theta} + \frac{D_{\theta p 1}\varepsilon_{(3/2,\ 1,\ 1/2)}}{2p\sin\theta\Delta p\Delta\theta}\right]f_{++0}\\
&+\left[\frac{D_{pp1}}{p^2\Delta p^2} - \frac{F_{p1}\varepsilon_{(1,\ 1/2,\ 1/2)}}{p^2\Delta p} + \frac{D_{\theta p 1}\delta_{(3/2,\ 1,\ 1/2)}}{2p\sin\theta\Delta\theta\Delta p} - \frac{D_{\theta p 0}\varepsilon_{(3/2,\ 0,\ 1/2)}}{2p\sin\theta\Delta p\Delta\theta}\right]f_{+00}\\
&+\left[-\frac{D_{p\theta 1}\varepsilon_{(1,\ -1/2,\ 1/2)}}{2p^2\Delta p\Delta\theta} - \frac{D_{\theta p 0}\delta_{(3/2,\ 0,\ 1/2)}}{2p\sin\theta\Delta p\Delta\theta}\right]f_{+-0}\\
&+\left[\frac{D_{p\theta 1}\delta_{(1,\ 3/2,\ 1/2)}}{2p^2\Delta p\Delta\theta} - \frac{D_{p\theta 0}\varepsilon_{(0,\ 1/2,\ 1/2)}}{2p^2\Delta p\Delta\theta} + \frac{D_{\theta\theta 1}}{p\sin\theta\Delta\theta^2} - \frac{F_{\theta 1}\varepsilon_{(1/2,\ 1,\ 1/2)}}{p\sin\theta\Delta\theta}\right]f_{0+0}\\
&+\left[-\frac{D_{pp1}}{p^2\Delta p^2} - \frac{F_{p1}\delta_{(1,\ 1/2,\ 1/2)}}{p^2\Delta p} - \frac{D_{pp0}}{p^2\Delta p^2} + \frac{F_{p0}\varepsilon_{(0,\ 1/2,\ 1/2)}}{p\Delta p}\right.\\
&\quad -\frac{D_{\theta\theta 0}}{p\sin\theta\Delta\theta^2} - \frac{F_{\theta 1}\delta_{(1/2,\ 1,\ 1/2)}}{p\sin\theta\Delta\theta} - \frac{D_{\theta\theta 0}}{p\sin\theta\Delta\theta^2} + \frac{F_{\theta 0}\varepsilon_{(1/2,\ 0,\ 1/2)}}{p\sin\theta\Delta\theta}\\
&\quad \left.-\frac{D_{\rho 1}}{\rho\Delta\rho^2} - \frac{\delta_{(1/2,\ 1/2,\ 1)}F_{\rho 1}}{\rho\Delta\rho} - \frac{D_{\rho 0}}{\rho\Delta\rho^2} + \frac{\varepsilon_{(1/2,\ 1/2,\ 0)}F_{\rho 0}}{\rho\Delta\rho}\right]f_{000}\\
&+\left[-\frac{D_{p\theta 1}\delta_{(1,\ -1/2,\ 1/2)}}{2p^2\Delta p\Delta\theta} + \frac{D_{p\theta 0}\varepsilon_{(0,\ -1/2,\ 1/2)}}{sp^2\Delta p\Delta\theta} + \frac{D_{\theta\theta 0}}{p\sin\theta\Delta\theta^2} + \frac{F_{\theta 0}\delta_{(1/2,\ 0,\ 1/2)}}{pp\sin\theta\Delta\theta}\right]f_{0-0}\\
&+\left[-\frac{D_{p\theta 0}\delta_{(0,\ 3/2,\ 1/2)}}{2p^2\Delta p\Delta\theta} - \frac{D_{p\theta 1}\varepsilon_{(-1/2,\ 1,\ 1/2)}}{2p\sin\theta\Delta p\delta\theta}\right]f_{-+0}\\
&+\left[\frac{D_{pp0}}{p^2\Delta p^2} + \frac{F_{p0}\delta_{(0,\ 1/2,\ 1/2)}}{p^2\Delta p} + \frac{D_{\theta p 1}\delta_{(-1/2,\ 1,\ 1/2)}}{2p\sin\theta\Delta p\Delta\theta} + \frac{D_{\theta p 0}\varepsilon_{(-1/2,\ 0,\ 1/2)}}{2p\sin\theta\Delta p\Delta\theta}\right]f_{-00}\\
&+\left[\frac{D_{p\theta 0}\delta_{(0,\ -1/2,\ 1/2)}}{2p^2\Delta p\Delta\theta} + \frac{D_{\theta p 0}\delta_{(-1/2,\ 0,\ 1/2)}}{2p\sin\theta\Delta p\Delta\theta}\right]f_{--0}\\
&+\left[\frac{D_{\rho 1}}{\rho\Delta\rho^2} - \frac{\varepsilon_{(1/2,\ 1/2,\ 1)}F_{\rho 1}}{\rho\Delta\rho}\right]f_{00+} + \left[\frac{D_{\rho 0}}{\rho\Delta\rho^2} - \frac{\delta_{(1/2,\ 1/2,\ 0)}F_{\rho 0}}{\rho\delta\rho}\right]f_{00-}.
\end{aligned} \tag{B.20}$$

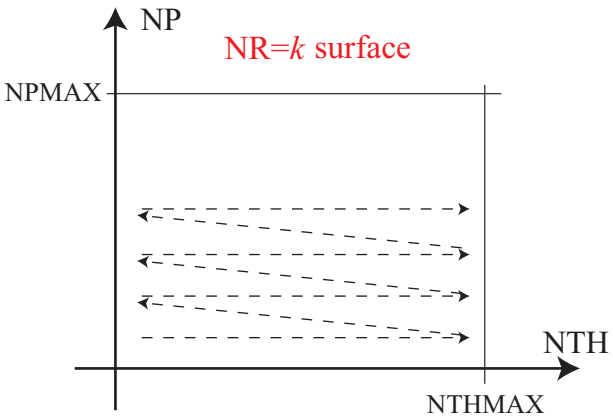

Figure B.3: The configuration of array of $\boldsymbol{f}$ is decided by the rule descibed in this figure.

The momentum distribution function vector, $\boldsymbol{f}$, has NPMAX $\times$ NTHMAX $\times$ NRMAX elements. The array of the elements is decided by the order descibed in fig. B.3. Namely, the momentum distribution function at the grid point (NP,NTH,NR)= (i, j, k) is contained in the [NPMAX $\times$ NTHMAX $\times (k-1)$ + NTHMAX $\times (i-1) + j$]th element of the vector.

The structure of the matrix $\overleftrightarrow{\boldsymbol{A}}$ is determined by the array of $\boldsymbol{f}$ and eq. (B.20).

Appendix C

Bounce average of divergence

C.1 derivation of the bounce averaged expression

The bounce average of the divergence of the flux is expressed as Eq. (3.163):

$$\langle \nabla \cdot \boldsymbol{S} \rangle_{\phi_B} \equiv \frac{1}{\tau_B} \int_0^{s_B} \frac{ds}{v_0 |\cos\theta|} \left[-\frac{1}{p_0^2} \frac{\partial}{\partial p_0} p_0^2 S_p - \frac{1}{p_0} \frac{\cos\theta}{\psi \sin\theta_0 \cos\theta_0} \frac{\partial}{\partial \theta_0} \sin\theta S_\theta - \frac{1}{\rho_0} \frac{\partial}{\partial \rho_0} \rho_0 S_\rho \right] \tag{3.163}$$

At first, for simplicity, we consider the transformation of the expression for S_p and S_θ. This expression can be rewritten by using the bounce average parameter, $\lambda = v_0 |\cos\theta_0| \tau_B$, as:

$$\begin{aligned}
\langle \nabla \cdot \boldsymbol{S} \rangle |_{p,\theta} &= -\frac{1}{\lambda} \left[\frac{1}{p_0^2} \frac{\partial}{\partial p_0} p_0^2 \int_0^{s_B} \frac{|\cos\theta_0|}{|\cos\theta|} S_p \, ds + \frac{1}{p_0 \sin\theta_0} \frac{\partial}{\partial \theta_0} \int_0^{s_B} \frac{\sin\theta}{\psi} S_\theta \, ds \right] \\
&= -\frac{1}{\lambda} \left[\frac{1}{p_0^2} \frac{\partial}{\partial p_0} p_0^2 \frac{\lambda}{\tau_B} \int_0^{s_B} \frac{ds}{v_0 |\cos\theta|} S_p + \frac{1}{p_0 \sin\theta_0} \frac{\partial}{\partial \theta_0} \frac{\lambda}{\tau_B} \int_0^{s_B} \frac{ds}{v_0 |\cos\theta|} \frac{\cos\theta \sin\theta}{\psi \cos\theta_0} S_\theta \right] \\
&= -\frac{1}{\lambda} \left[\frac{1}{p_0^2} \frac{\partial}{\partial p_0} p_0^2 \lambda \left\langle S_p \right\rangle_{\phi_B} + \frac{1}{p_0 \sin\theta_0} \frac{\partial}{\partial \theta_0} \sin\theta_0 \lambda \left\langle \frac{\cos\theta \sin\theta}{\psi \cos\theta_0 \sin\theta_0} S_\theta \right\rangle_{\phi_B} \right].
\end{aligned} \tag{C.1}$$

C.1.1 Transformation of bounce variable

Since the arclength, s, and infinitestimal element, ds, appeared in the definition of the bounce average depend on the normalized minor radius, ρ, the variable s should be transformed into the other variable which is independent from ρ. Therefore the arclength is transformed into the poloidal angle ϕ. The relations between s and ϕ are given by:

$$s = s_B \frac{\phi}{\phi_B}, \quad \frac{s_B}{\phi_B} = q(\rho) R_0. \tag{C.2}$$

Using these relations, the definition of the bounce average can be rewritten as:

$$\begin{aligned}\langle Q\rangle &\equiv \frac{1}{\tau_B}\int_0^{s_B}\frac{Q}{v_0|\cos\theta|}ds \\ &= \frac{s_B}{\tau_B\phi_B}\int_0^{\phi_B}\frac{Q}{v_0|\cos\theta|}d\phi \end{aligned} \tag{C.3}$$

Therefore the bounce average of the divergence of flux S_ρ can be expressed as:

$$\begin{aligned}\langle\nabla\cdot\boldsymbol{S}\rangle|_\rho &= \frac{1}{\tau_B}\int_0^{s_B}\frac{ds}{v_0|\cos\theta|}\left(-\frac{1}{\rho_0}\frac{\partial}{\partial\rho_0}\rho_0 S_\rho\right) \\ &= \frac{s_B}{\tau_B\phi_B}\int_0^{\phi_B}\frac{d\phi}{v_0|\cos\theta|}\left(-\frac{1}{\rho_0}\frac{\partial}{\partial\rho_0}\rho_0 S_\rho\right) \\ &= -\frac{q(\rho)R_0}{\lambda}\frac{1}{\rho_0}\frac{\partial}{\partial\rho_0}\rho_0 v_0|\cos\theta_0|\int_0^{\phi_B}\frac{S_\rho}{v_0|\cos\theta|}d\phi \\ &= -\frac{q(\rho)R_0}{\lambda}\frac{1}{\rho_0}\frac{\partial}{\partial\rho_0}\rho_0\frac{\lambda s_B}{\tau_B\phi_B}\int_0^{\phi_B}\frac{\phi_B}{s_B}\frac{S_\rho}{v_0|\cos\theta|}d\phi \\ &= -\frac{q(\rho)R_0}{\lambda}\frac{1}{\rho_0}\frac{\partial}{\partial\rho_0}\rho_0\frac{\lambda}{q(\rho)R_0}\left\langle S_\rho\right\rangle. \end{aligned} \tag{C.4}$$

Thus, from Eq. (C.1) and (C.4), Eq. (3.164) is given.